POLITECNICO DI MILANO

Master of Science in Civil Engineering

CERM – Civil Engineering for Risk Mitigation

Two Numerical Approaches of Shock Tube Test:

Discrete Model of PFC3D and Continuous Model of Abaqus

Supervisors: Ph.D. Andrea Galli

Ph.D. Paolo Martinelli

Master Thesis of:

LIU YUE   Matr. 780272

Academic Year 2012/2013

Abstract

A shock tube experimental test is established to perform the simulation of soil ashlar belonging to shallow tunnel subjected to shock blast wave.

In this work of thesis, a simple continuous numerical model of this shock tube is created using Abaqus, which consists of axial-symmetric soil specimen (1.42m long, 29.15m wide) and analytical rigid chamber (without thickness). Four kinds of material are considered: Elastic model, Porous elastic model, Drucker-Prager linear model, Drucker-Prager cap model. The sand-steel chamber's friction influence is studied in detail both in static and dynamic conditions. The behaviors of the 4 materials are investigated in several cyclic static load conditions. The effects of friction and plasticity are analyzed within the results of Abaqus models.

In another approach, a discrete numerical model of shock tube is created using PFC3D, which consists of rigid cylinder wall without thickness and large amounts of balls full filled inside walls. The model has 1.42m length and 29.15mm inter-radius. Four impulse waves of experimental tests are applied on the model.

Furthermore, the results of these two models under the experimental impulse loads are analyzed and compared, to discuss the difference between these two approached.

Key words: shock tube, blast load, dynamic test, discrete model, continuous FEM, soil/structure interaction, material plasticity.

Content

Chapter 1 Introduction

It is still an open issue nowadays to guarantee the tunnel safety and security. Italy owns the highest length (292 kilometers) of roadway tunnels in European countries, which number is equal to 66% of the total number of European roadway tunnels. Furthermore, in the last few years the international media has reported the occurrence of some of the most serious accidents in the alpine region such as the Mont Blanc Tunnel (March 1999) and the Gotthard Tunnel (October 2001). The vehicle collisions are generally the reasons that cause fire in tunnels, and it can be very destructive especially when oil/gasoline tanker trucks are involved. Some urban area of tunnel embedded in soft soil, which occurs similar accidents, can partial collapse and has significant settlement. This is a great threat to building stability at ground level. Fire and blast are considered as exceptional loads, but they are never taken into account in the lining design; to increase the safety of the lining, and reduce the occurrence of catastrophic structural collapse, an effort in introducing these aspects in the design process appears necessary (Caverzan, 2010).

Traditionally, experimental investigations of structures subjected to blast loading conditions have been performed through the use of explosive (TNT); the energy associated with the pressure waves, partly is dissipated in the fracture of tunnel segments and at the soil-structure-interface and partly causes transmission and reaction of the waves at the intrados and extrados interfaces of the structure, thus resulting in structure damped vibration. An alternative technique for creating impulse loading on a structure portion consist of the use of the shock tubes, thus allowing shock and expansion waves. The use of a shock tube (figure 1.1) instead of an explosive has distinct advantages:

- generation of planar waves front;
- shock tube is less hazardous than explosives and offers an easier and more repeatable load control. (Corti L., Corti L. G., 2012)

Figure 1.1 shock tube view (Corti L., Corti L. G., 2012)

The aim of this thesis is to study the behavior of the soil specimen under blast impact with interaction of the steel chamber of shock tube. Figure 1.2 shows the Sketch of an underground tunnel explosion and schematization of the problem under study. In the thesis numerical simulation approach is utilized instead of experimental ways. So far, there are two kinds of models to simulate the soil numerically. One is discrete model, another one is continuous model. The former consists of a large number of rigid entities, between which there are interactions. The

latter is traditional finite element model. Because of the diversity of soil, it is hard to conclude entirely which model is better. These two kinds of models show their advantages and limitations compared to experiment investigations.
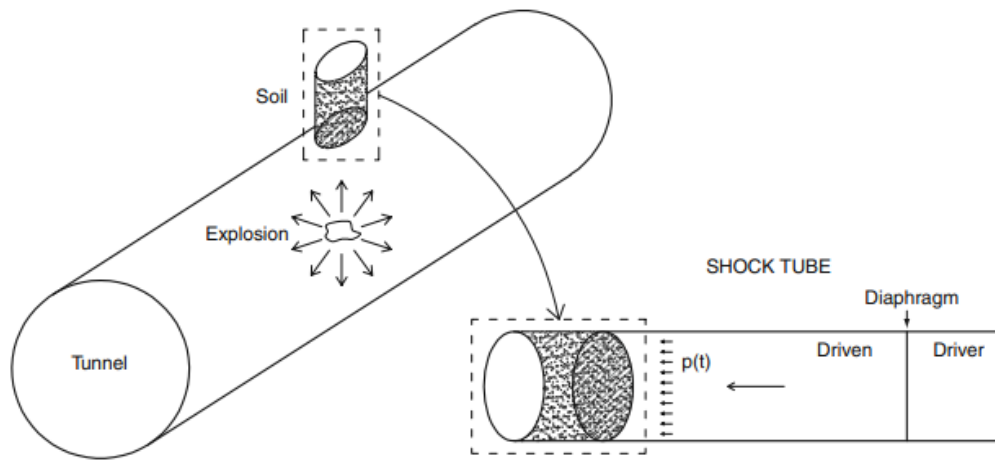
Figure 1.2 Sketch of an underground tunnel explosion
and schematization of the problem under study (Colombo et al. 2011)

This thesis consists of three parts:

(I) Chapter 2 is the description of the shock tube experiments, which is proceeded by previous researchers. The results of experimental tests are briefly excerpted at the end of this chapter.

(II) Chapter 3 is the introduction of software PFC3D and the discrete model of shock tube. PFC3D is one software of discrete numerical approach. Other researchers have created the discrete model for these experimental tests. And also their results are briefly excerpted at the end of this chapter.

(III) Chapter 4 and 5 are the third part, are also the main part of this thesis. In this part, a simple continuous model of shock tube is created utilizing software Abaqus. The detailed description of model and the results under experimental impulse loads are included in this part. At the same time the comparisons among the results of experimental tests and these two numerical models are analyzed.

Chapter 2 Description of Shock Tube and Experiments

2.1 Description of the equipment

The shock tube consists of the equipment designed to generate a shock wave, in a relatively simple and economic way. So, the entire equipment will enable to study the explosion reproduced and its effects. This tool has been so far mainly used in the aerodynamic field.

The shock tube used for such research has a of length is 14.9m and an internal diameter of 981mm. It is composed of four main sections (Figure 2.1.1):

- Driver section (high pressure chamber, at the right in the figure);
- Buffer section (intermediate pressure chamber, reduced length and placed between the space of driver and driven);
- Driven section (low-pressure chamber, of considerable length, at the center in the figure);
- Specimen and soil section (at left in the figure).

Figure 2.1.1 The shock tube (Corti L., Corti L.G., 2012)

Each section is composed of stainless steel, characterized by the yield strength fy= 210MPa and the ultimate tensile stress fu= 520MPa. All sections have been designed in order to withstand a constant pressure of 6MPa remaining in the elastic domain. The sections both driver and buffer will subsequently be placed in pressure. The buffer is located between the chamber of driver and driven, and is separated from them by means of two diaphragms. To cause a rupture of these diaphragms and the consequent generation of the shock wave, it then makes depression in the chamber buffer intermediately, so as to create a large difference of pressure between the driver chamber and the driven chamber which is at ambient pressure. The breaking pressure depends on the material of the diaphragm and its thickness. The thin diaphragms can avoid possible disturbances wave output caused by their breakup. Further details can be found in the reference paper (Colombo, et al. 2011).

2.1.1 Basic principles of operation of the shock tube

In its simple configuration, the shock tube is mainly divided into two parts: the high pressure chamber and low pressure chamber (figure 2.1.2). Both are cylindrical and steady section. These sections are separated by a diaphragm of thin material with high resistance. The high-pressure chamber (driver section) is shorter, while the low-pressure chamber (section driven) is longer. Both sections can be able to control their different gases, in different pressure and temperature. The initial conditions at rest are p_4, T_4, m_4 and γ_4 for the "driver" and p_1, T_1, m_1 and γ_1 for the driven section, where p is the pressure, T is the temperature, m is the molecular weight and $\gamma = c_p/ c_v$ is the ratio between the specific heat at constant pressure (c_p) and the specific heat at constant volume (c_v).
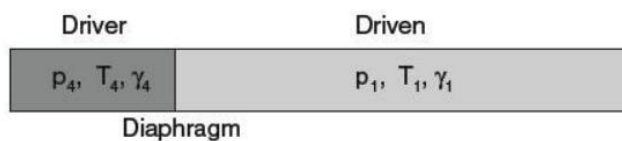

Figure 2.1.2 Schematic representation of the shock tube (Colombo, et al. 2011)

When the difference of pressure between the two chambers is such as to determine the breaking of the diaphragm, the expansion of the gas initially contained in the driver section, forms instantly a compression wave which travels through the driven section. The front of the wave, produced by the impulsive push, is rapidly evolving in a shock wave, while an induced flow develops immediately after it. At the same time, a rarefaction wave (also called the wave of expansion) develops and moves within the driver section. The instant when the shock waves and expansion reach the closed end, they are reflected and begin to move towards the center of the shock tube, interacting simultaneously with the flow induced.

In order to describe the flow of gas within a theoretical formulation of basis, you need the following assumptions:

- ideal gas with constant specific heat;
- one-dimension flow;
- no viscosity in the exchange of heat;
- the explosion of the diaphragm is instantaneous and produces no disturbance in the gas flow;
- the tube is infinitely rigid.
-

After the rupture of the diaphragm, four gaseous states are obtained, all of pressures, temperatures and different densities. It can then identify the regions of space-time in which they move (Figure 2.1.3).
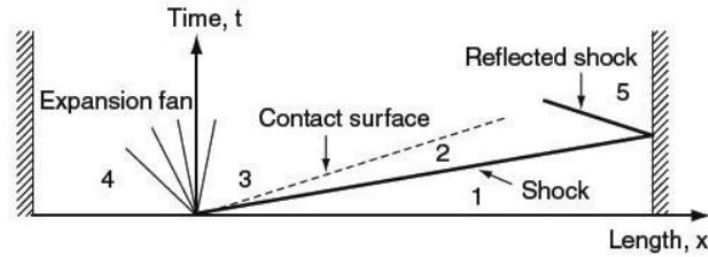
Figure 2.1.3 Diagram relate to the pressure wave that are created in the shock tube
(Colombo, et al. 2011)

The initial gas is contained in region 1 (driven) and 4 (driver) of Figure 2.1.3. The regions of flow induced by the compression and expansion waves are separated by an interface called the contact surface. It indicates the position that original gas contact to the diaphragm. Along this discontinuity of pressure and speed it appears to be the same for both sides, in a certain instant, while temperature and density are slightly different. This is due to opposite actions made by the compression and expansion waves.

The region 2 contains the gas that is compressed and heated by the shock wave, while in the Region 3 it is the expanded gas and cooled by the wave of rarefaction. The region 5 contains instead the gas after the reflection of the shock wave incident on the right end of the shock tube.

2.1.2 Driver, buffer and driven sections

The chambers of driver and driven have the lengths of 2.35m and 10.5m respectively, with a circular internal diameter of 481mm, while the thickness is 13.5mm external. Between these two sections there is the buffer section, 0.26 m long, with an internal diameter which is also 481mm long and an outer diameter of 857mm (Figure 2.1.4).
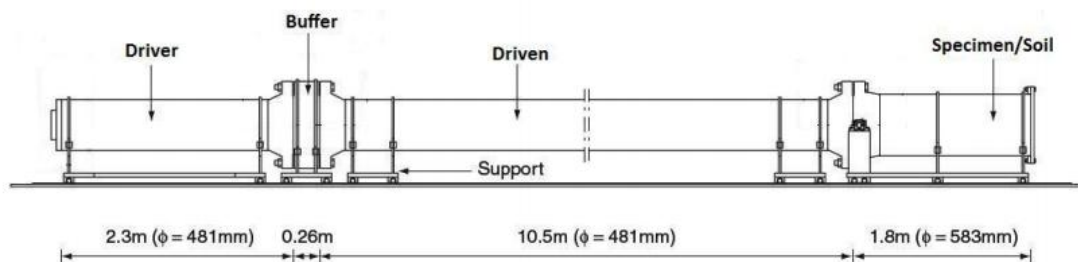

Figure 2.1.4 Geometry of shock tube (Colombo, et al. 2011)

The three chambers are bolted together with a self-closing system (pressure actuator), as shown in Figure 2.1.5.

Figure 2.1.5 Assembly of driver, buffer and driven (Corti L., Corti L.G., 2012)

The left end of the driver chamber is tightened by a special steel flange (Figure 2.1.6).

Figure 2.1.6 Particular circle flange of driver chamber (Corti L., Corti L.G., 2012)

The length of this section ensures that the front of reflected expansion wave cannot reach the shock wave along its travel to the end of the driven chamber. The ratio between the length and the inner diameter of the chamber is approximately 20, the value such as to ensure that this section is long enough for the full development of the shock wave.

In order to obtain the useful measures on the setting of the apparatus, many inlets for the introduction of transducers and pressure relief valves are included on the outer surface of each section. There are also safety valves set at a maximum tolerable pressure equal to 6MPa.

2.1.3 Specimen and soil section

This section is 1.8m long, has an internal diameter of 583mm and a thickness of 13.5mm (Figure 2.1.7 and Figure 2.1.8). It is bolted to the driven chamber through the use of twenty screws of diameter 54mm, while the other end is tightened closed by a flange.

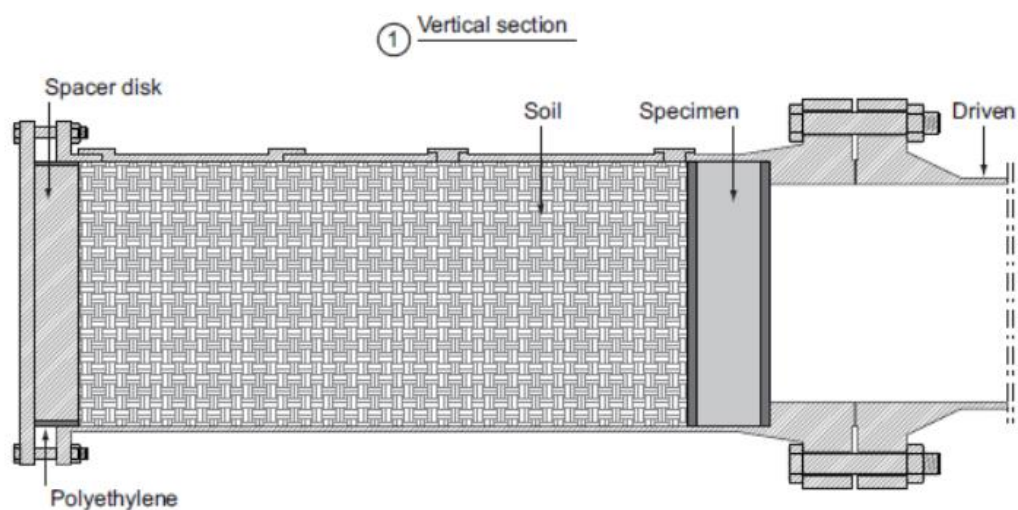Figure 2.1.7 Vertical section of specimen/soil section (Colombo, et al. 2011)

Figure 2.1.8 The specimen/soil section (Corti L., Corti L.G., 2012)

The final configuration of this section is obviously horizontal. In order to install the hard fiber-reinforced concrete and the soil inside of the chamber, the latter is made to rotate by means of a first rotary bearing system, allowing reach the vertical position.

2.2 Test set-up

The first step consists in positioning the two diaphragms on the ends of the buffer steel section, on both sides of the diaphragms, gaskets necessary to ensure sealing. Then it is necessary to assemble all the components: driver, buffer and driven. To accomplish this, on each interface there are twenty hydraulic nuts, each is connected to a hydraulic jack on the corresponding screws: applying pressure to the clamping nuts, with a strong compression between the flanges, thus obtaining the union of all the chambers (Figure 2.2.1). This only takes a few minutes.

Figure 2.2.1 Steel diaphragm and assembly stage of driver, buffer and driven
(Corti L., Corti L.G., 2012)

Subsequently, with the help of a crane, the specimen/soil section can be placed upright, open superiorly. The rotation is around the axis horizontal load-bearing system (Figure 2.2.2).

Figure 2.2.1 The specimen/soil section disposed in vertical (Corti L., Corti L.G., 2012)

The concrete specimen, including all of the necessary sensors, must be positioned within the specimen/soil chamber until reaching the bottom of the section. In order to be able to move it more easily with the crane, two small connectors were incorporated to it (Figure 2.2.2).

Figure 2.2.2 Positioning of the hard concrete instrumented inside the specimen/soil chamber
(Corti L., Corti L.G., 2012)

An apparatus containing the granular material is placed vertically on the axis of the specimen/soil section. This apparatus, which uses the principle of rain fall, is supported by external steel and consists of two containers: the diffuser of sand and the collector of sand (Figure 2.2.3 and Figure 2.2.4).

Figure 2.2.3 Chassis and pump with the detail of the final part (Corti L., Corti L.G., 2012)

Figure 2.2.4 Diffuser and collector (Corti L., Corti L.G., 2012)

The degree of compaction of the material is controlled by the size of a grid metal positioned inside the manifold. The apparatus used here is similar to what is already widely used in the Soil Mechanics Laboratory of the Politecnico of Milano. Once the specimen/soil chamber turns out to be filled with sand, the section can be tightened with the flange so closed and subsequently repositioned in its horizontal configuration.

In order to achieve the predetermined level of confinement within the sand, a steel disc spacer can be placed between it and the blind flange. The selected compression stress is then gradually achieved through the use of a hydraulic jack, then, it secures the blind flange with bolts (Figure 2.2.5 and Figure 2.2.6).

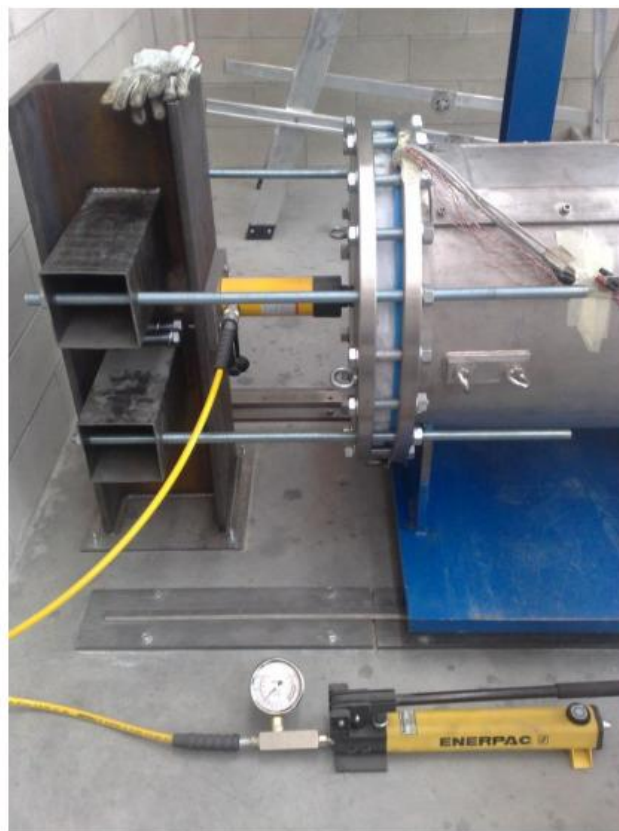Figure 2.2.5 The disc spacer and the blind flange (Corti L., Corti L.G., 2012)

Figure 2.2.6 The hydraulic jack used to achieve the desired degree of confinement
(Corti L., Corti L.G., 2012)

Finishing this stage, the specimen/soil chamber can be assembled to the driven section. To this end, additional twenty nuts are mounted on the respective screws that join the two sections (Figure 2.2.7).
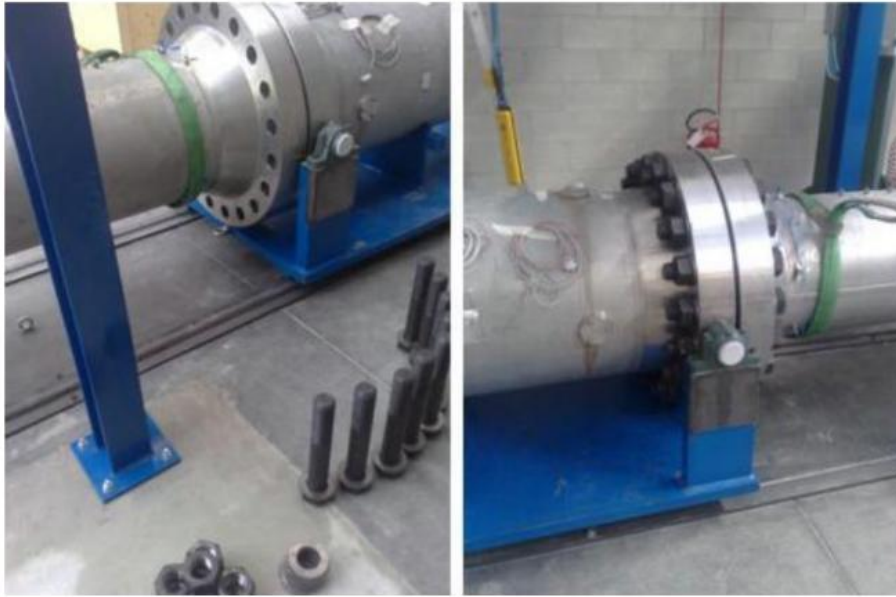

Figure 2.2.7 Assembly of the specimen/soil section to the driven (Corti L., Corti L.G., 2012)

For this type of tests, the buffer and driver sections are placed by pressure caused by the injection of helium gas, while the gas used inside the driven chamber is the air under ambient conditions. For example, to obtain a reflected pressure of p5= 5MPa, a pressure about 4.2MPa of helium is needed in the driver section, but 56.7MPa is necessary of the air. This justifies the choice of using the helium gas, besides the fact that it appears to be easily available, inexpensive and inert.

Prior to the injection of helium gas in the driver and buffer sections, the last thing is the air present within them must be drained away. To achieve this process, a vacuum pump is used (Figure 2.2.8).

Figure 2.2.8 The vacuum pump (Corti L., Corti L.G., 2012)

After reaching the desired vacuum (-800 mbar), it is possible to introduce helium within both the driver chamber and the buffer chamber, until they are achieved the pressure level assigned (Figure 2.2.9). The pressure in the buffer chamber should be approximately equal to the average of the pressure in driver and driven chambers.

Figure 2.2.9 Helium entering into the chamber buffer and driven (Corti L., Corti L.G., 2012)

Then it achieves the pressure value designed for all the sections. The gas present in the buffer section is intermediately ejected by the use of appropriate electro-valves, thus allowing return to atmospheric pressure. In this instant, the pressure difference between the buffer and driver sections is such as to cause the rupture of the first corresponding diaphragm seal. The consequent rupture of the second diaphragm occurs immediately. The rapid propagation of the gas in the pressure inside the driven section leads to the formation of a shock wave, which travels inside until bumps on the impulsive hard concrete localized at the opposite end.

2.3 Material

In the experimental campaign the fiber-reinforced concrete specimens with different layers and different thicknesses have been tested, under varied levels of pressure. The diameter of each remains the same, 560mm.

2.3.1 Description of the concrete specimen

The first type of specimen is composed of three layers (disc type 1, figure 2.3.1):
- two outer layers consist of high-performance fiber-reinforced concrete (HPFRC), with a thickness of 20mm;
- a central layer consists of steel fibers reinforced concrete (SFRC), with a thickness of 140mm.

Figure 2.3.1 The specimen composed of three layers (Corti L., Corti L.G., 2012)

These layers are made in different time periods. The outer layers are first made and get harden. In the layer that will be in contact with the soil two connectors should be included, which are necessary for the movement of the concrete specimen. The length of these connectors must be greater than the thickness of the layer. Similarly two anchors have inserted in the outer layer that will be exposed to the shock wave. The central layer SFRC is made on the latter layer, and after another layer HPFRC immediately. In this way, the cohesion between the layers is ensured by two contributions: the connectors and the cohesion of the adhesive cement paste.

The second type of specimen is composed of two layers (disc type 2, Figure 2.3.2):
- a layer composed of high-performance fiber reinforced concrete (HPFRC), with a thickness of 20mm;
- a layer composed of steel fibers reinforced concrete (SFRC) with a thickness of 140mm.

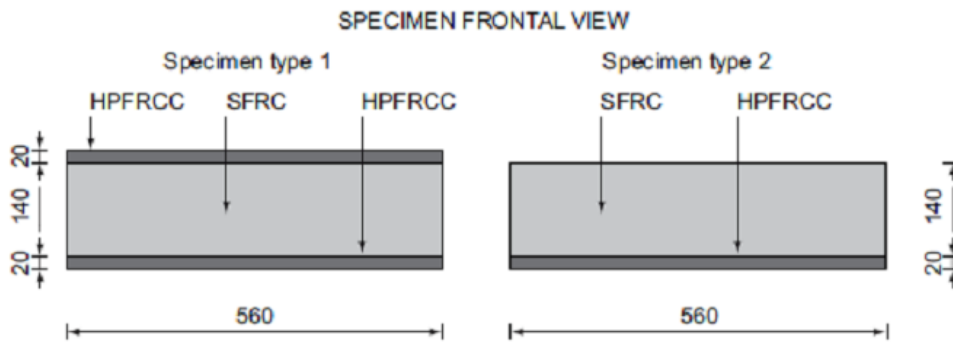Figure 2.3.2 The specimen composed of two layers (Corti L., Corti L.G., 2012)

Figure 2.3.3 Schematization of the two types of concrete specimen (Colombo et al. 2011)

2.3.2 The Hostun sand

The sand used for the experimental tests is the Hostun sand HN31 (HS) (figure 2.3.4).
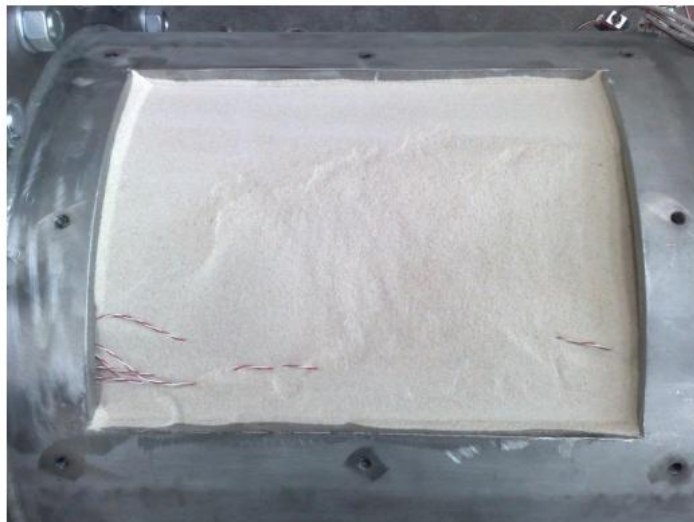

Figure 2.3.4 The Hostun sand (Corti L., Corti L.G., 2012)

This material has been chosen because of its characteristics rather uniform in terms of grain size and in continuity with previous studies. The main characteristics of the material used are summarized below (Table 2.1):

Table 2.1 The parameters of sand used (Bonacina F.,Dell'era G., 2013)

e_{min}	e_{max}	D_{10} [mm]	D_{50} [mm]	D_{60} [mm]	ρ_s [g/cm^3]	C_u
0.65	1.0	0.25	0.334	0.352	2.65	1.41

For the experimental tests it is important to have a relative density which is known and reproducible for each new test. For this purpose the method of fluid deposition (figure 2.3.5) is used, in which the sand appropriately diffuse and drop in the specimen/soil section by gravity. This method allows satisfying the following requirements:

- samples must have the required average density;
- samples must be homogeneous, so the local density must not have significant changes compared to the average value;
- the relative density range can be chosen between 20% and 100%;
- the method should allow easy and rapid preparation of sample.
-

Figure 2.3.5 The deposition fall (Corti L., Corti L.G., 2012)

The relative density of the sand depends on four parameters:
- grain size of the sand;
- height of the fall;
- diameter of the holes of the grid (1cm);
- distance between the holes (2cm).

This method ensures that you can get a homogeneous density of the soil of about 1400 kg/m^3 for each test (Figure 2.3.6)
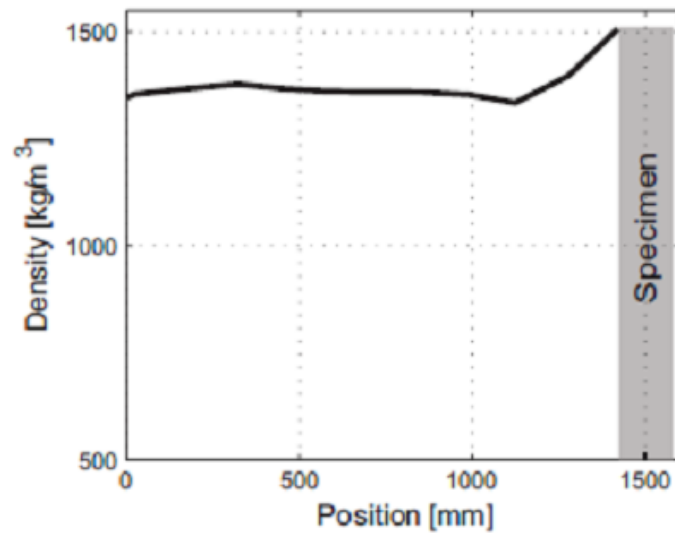
Figure 2.3.6 Density of the sand sample (Bonacina F.,Dell'era G., 2013)

2.4 The levels of pressure impact

2.4.1 The wave used

The tests carried out with the use of the shock tube is fixed predict the maximum reflected pressure of the concrete specimen. In this regard, it is appropriate to point out that this study is not intended to reproduce the maximum pressure right near the source of the explosion, but a pressure "widespread" in the environment around the source.

The experimental campaign is composed of two series of tests, which are different from the history of impulsive load applied (the shape of the pressure wave imposed on the specimen) and the type of concrete specimen tested. The first series of tests, referred to low pressure test, is characterized by a peak pressure of 0.34MPa. The second series of tests, referred to high pressure tests, is characterized by a peak pressure of 1.03MPa.

These two different pressure waves are determined by two different initial conditions of helium pressure in the driver and buffer chambers:

    Low pressure: buffer = 0.22MPa; driver = 0.44MPa

    High pressure: buffer = 0.70MPa; driver = 1.40MPa

Then a total of six tests were performed: three under low pressure and three under high pressure. For both pressure levels two tests were performed on the disc type 1 (two outer layers) and one test on the disc type 2 (an outer layer). The tests are listed and summarized in Table 2.2. For each test a specific identification code has been assigned in order to easily understand what evidence was taken in analysis: L stands for low pressure test, H for high pressure test, the confinement 40 is implemented at 40kPa, 122 confinement to 122kPa, T1 is going to disc type 1, T2 for disc type 2 and the final number is used to appoint two tests identical.

Table 2.2 Different type of experimental test (Bonacina F.,Dell'era G., 2013)

name	Data of test	Number of layer	Peak of pressure [MPa]	Duration of loading [ms]	Specific impulse [MPa/ms]
L-40-T1	30/03/2012	3	0.35	40.7	3.85
L-122-T1	17/04/2012	3	0.34	37.7	3.57
H-122-T1-1	03/05/2012	3	0.32	34.7	3.10
H-122-T1-2	09/05/2012	3	0.99	27.8	7.46
L-122-T2	11/05/2012	2	1.05	14.9	5.88
H-122-T2	16/05/2012	2	1.07	22.9	9.61

The average pressure of both series of tests, recorded by the transducer right near the hard concrete, is represented in figure 1.25 by the marked lines.
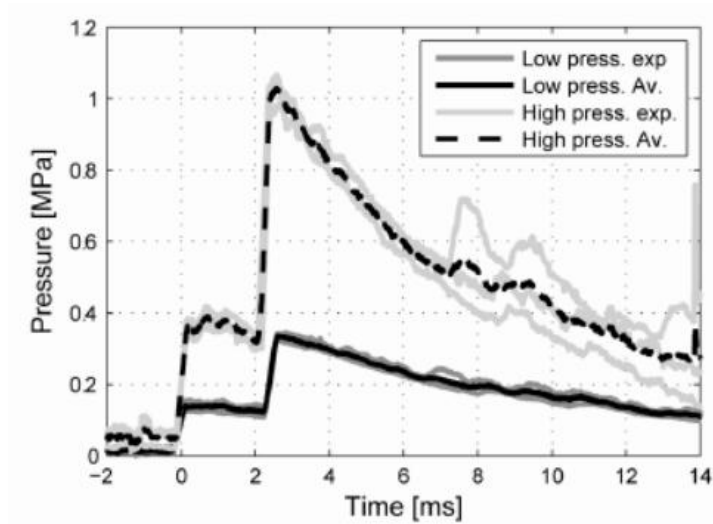
Figure 2.4.1 Pressures recorded at 30cm from the hard concrete (Bonacina F.,Dell'era G., 2013)

For the following analysis carried out, the first four cases listed in Table 2.2 have been focused on, the specimen samples consist of three layers (Figure 2.4.1).

2.4.2 Confinement

For all the tests performed, with the exception of the first test L-40-T1, a preload of 30kN (equivalent to a pressure of 122kPa) from the side of the blind flange was applied by means of a hydraulic jack. The test L-40-T1 provides, instead, a preload of 10kN (equivalent to a pressure of 40kPa) on the sand.

2.5 Measuring instruments

The shock tube is equipped in all its sections of many sensors, which are essential controls of the correct operations of the apparatus and measurements of the experimental data represented the behavior of the concrete specimen and soil.

The parameters to be measured are:

- the pressure of the shock wave;
- the deformation of the driven section and specimen/soil section;
- the accelerations of the concrete specimen and the soil;

2.5.1 Technical specifications

2.5.1.1 Dynamic pressure transducers ICP

To measure the pressure, a series of dynamic pressure sensors (Figure 2.5.1) were positioned inside the driven section through suitable openings.

Figure 2.5.1 Position of the dynamic pressure transducers on the driven chamber
(Corti L., Corti L.G., 2012)

The pressure transducer ICP (Integrated Circuit Piezoelectric) adopted in this campaign is shown in Figure 2.5.2.

Figure 2.5.2 Pressure transducer ICP (Corti L., Corti L.G., 2012)

It is able to measure the pressure up to 6.9MPa, with a sensitivity of 0.7mV/kPa and a rise time equal to 1s. The resonance frequency of the transducer is greater than 500kHz, a value such as to ensure an appropriate response of high frequency phenomena such as an explosion (table 2.3).

Table 2.3 Technical characteristics of dynamic pressure transducer ICP (Corti L., Corti L.G., 2012)

ICP blast pressure transducers		Pressure sensor: M102B04	
Measurement range (for ±5V output)	[KPa]	6900	
Useful over range (for ±10V output)	[KPa]	13790	
sensitivity	[mV/KPa]		$0.7 \pm 10\%$
resolution	[KPa]	0.14	
Rise time (incident)	[μs]		≤ 1.0
Non-linearity	FS		$\leq 1.0\%$
Resonant frequency	[KHz]		≥ 500

2.5.1.2 Accelerometers ICP

These accelerometers have been adopted in order to measure the accelerations of the concrete specimen and the soil during the impact of shock wave (Figure 2.5.3). ICP accelerometers are born in the mid 60's and their peculiarities reside in incorporating them into a voltage amplifier, and are capable of converting the electrostatic charges coming from the high impedance piezoelectric sensor into a voltage signal of low impedance. This is important particularly when it has been related with high frequency explosions, since the signal in low impedance output can be transmitted through long cable without the risk of signal quality losses. The ability to have a sensitivity of invariable measurement, regardless of cable length, is another feature that makes it convenient to use this type of accelerometers.

Figure 2.5.3 ICP accelerometer

Table 2.4 collects the advantages related to the choice of these sensors, and also compared to the piezoelectric transducers (PE). The accelerometer ICP chosen for this study is characterized by a quartz sensor element and the resonant frequency is greater than 70 kHz. It has a measuring range of ± 500g as a peak, a larger bandwidth of 10 kHz and a resolution bandwidth of 0.005 g rms. The signal conditioning of accelerometers is carried by a signal conditioner ICP with increment equal to 1, the bandwidth of 10 kHz and an electrical noise broadband equal to 3.5 μV rms (table 2.5).

Table 2.4 Advantages and disadvantages of ICP accelerometers, piezoelectric transducers compared to the PE sensors (Corti L., Corti L.G., 2012)

ICP accelerometer	
PE sensors	ICP sensors
advantages	
Extended low frequency response Flexibility in properly adjusting the electrical output High temperature range Interchangeability in existing system	Uses standard coaxial cables Drives long cable without noise increase or loss of resolution Operates from constant current-power source Have great resistance to contamination and electrical interference Better system reliability Bias monitor detects cable faults
Disadvantages	
Size and sensitivity are directly related Capacitive effects and cable length increase noise and reduces resolution Require low-noise cables Are more susceptible to electrical interference Higher cost per channel	Limited temperature range May not be interchangeable in system with different power requirement Electrical characteristic are fixed Sensitivity, range, discharge time constant are fixed within the sensor

Table 2.5 Technical characteristics of ICP accelerometers (Corti L., Corti L.G., 2012)

ICP accelerometer M353B17			
Measurement range		± 500	$[m/s^2]pk$
Sensitivity		$1.02 \pm 15\%$	$[mV/(m/s^2)]$
Frequency range (for $\pm 5\%$)		$1 \div 10000$	[Hz]
Frequency range (for $\pm 10\%$)		$0.7 \div 17000$	[Hz]
Rise time (incident)		≤ 4.0	[μs]
Non-linearity		$\leq 1.0\%$	
Resonant frequency		≥ 70	[kHz]
Broadband resolution	0.05		$[m/s^2]rms$
Transverse sensitivity		$\leq 5.0\% \pm 15\%$	

2.5.2 Positions of instruments

All measuring instruments were placed in the same positions for each test performed and is indicated in the following.

2.5.2.1 Dynamic pressure transducers ICP

Four pressure transducers ICP (indicated with the letter "P"), provided with quartz sensor element, were positioned along the axis of the driven chamber in order to measure the pressure inside the chamber (Figure 2.5.4). The first is at 2250 mm from the driven section (P1), while the second is 1250 mm (P2). In the part next to the concrete specimen two pressure transducers were placed, namely at 300 mm from the driven section, one is on the top (P3) and one is 120 degrees from it (P4) (Figure 2.5.5). In this thesis the results of the transducer P3 were used.

Figure 2.5.4 Pressure transducers on driven section (Corti L., Corti L.G., 2012)
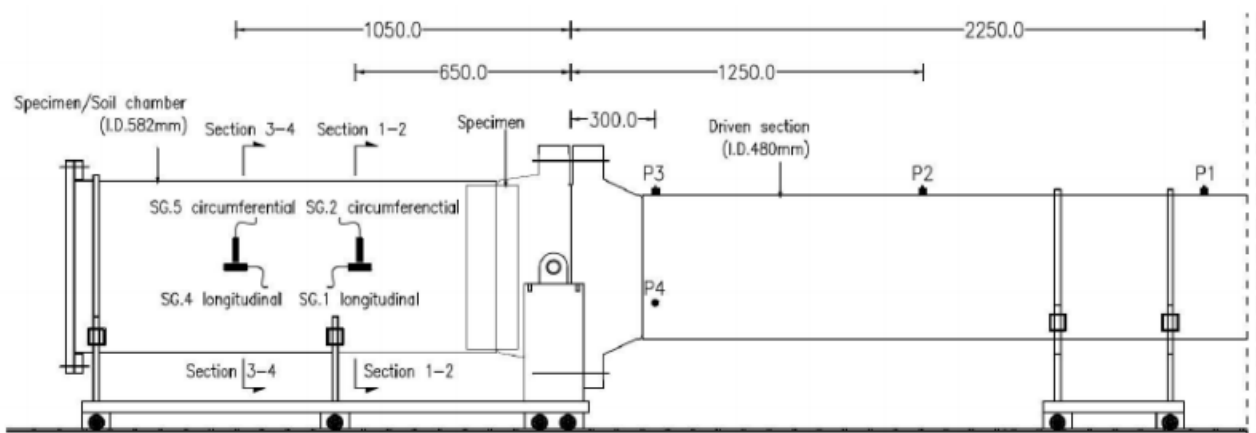
Figure 2.5.5 Positions of the dynamic pressure transducers and strain gauges
(dimensions in mm) (Colombo et al. 2013)

2.5.2.2 Accelerometers ICP on the specimen

During the tests the accelerations of the concrete specimen were recorded. For each of these, data are recorded by ICP accelerometers which are attached to the surface of the specimen in contact with the soil and are positioned in the following configuration (figure 2.5.6):

- A2, A3 and A4 are positioned at 120 ° from each other on a circumference that is 4 cm from the outer perimeter of the specimen;
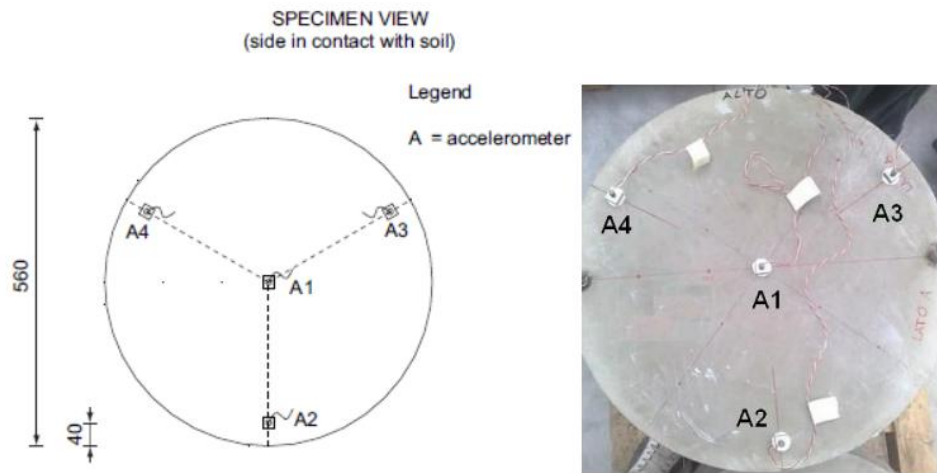- A1 in the center of the specimen.

Figure 2.5.6 Layouts of accelerometers on the hard fiber reinforced concrete
(Colombo et al. 2013)

Within the sand two sections were instead placed at different distances from the concrete specimen, on which four accelerometers were placed on each (Figure 2.5.7):

- Section A-A at a distance of 1 m from the blind flange, and then at 42 cm from the surface of the specimen;
- Section B-B at a distance of 50 cm from the blind flange, and then at 92 cm from the surface of the specimen.
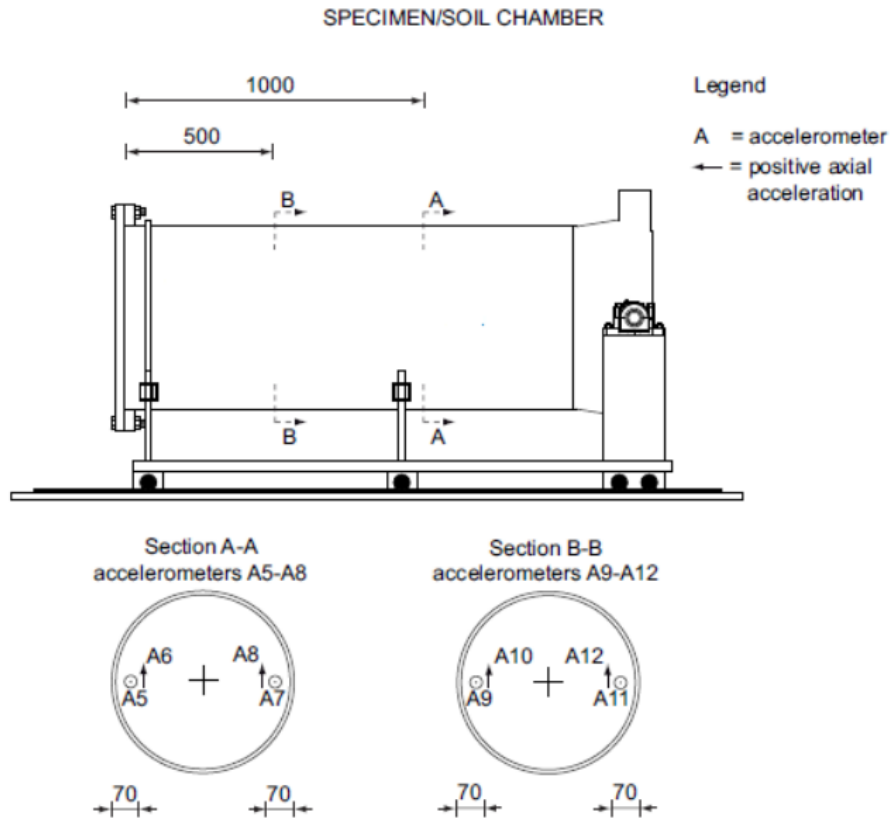
Figure 2.5.7 Disposition of accelerometers in sections A-A and B-B of the specimen/soil chamber (Colombo et al. 2013)

For each section, two small boxes were placed (Figure 2.5.8), each of them are containing two accelerometers ICP and four were arranged in the longitudinal direction (A5 and A7 on section A-A, A9 and A11 on the B-B) and four were seated in the vertical direction (A6 and A8 on section A-A, A10 and A12 on section B-B) (Figure 2.5.9). These boxes have been placed along the horizontal diameter of the section at a distance approximately equal to 70 mm from the inner radius of the chamber.
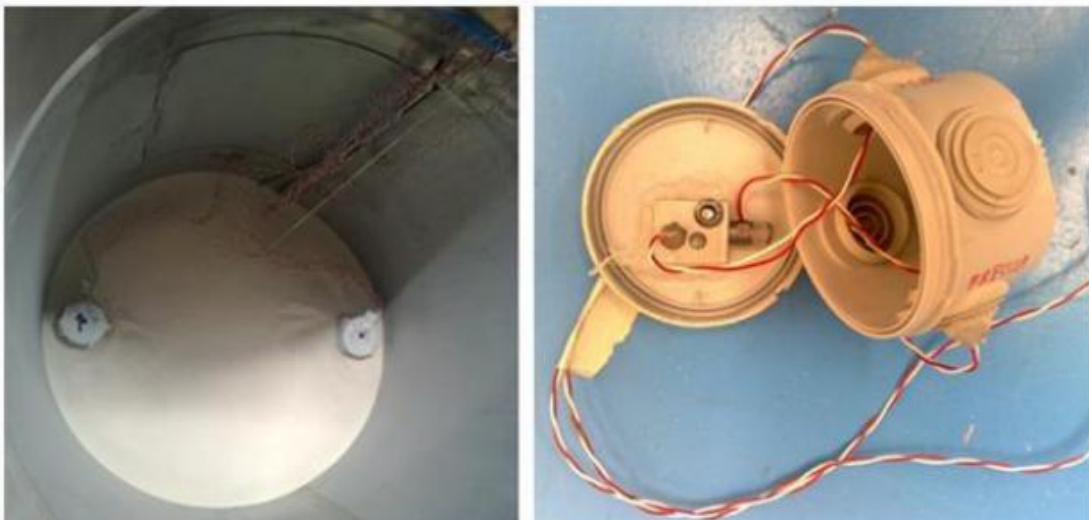
Figure 2.5.8 ICP accelerometers placed on the soil (Corti L., Corti L.G., 2012)

Figure 2.5.9 ICP accelerometers on different sections (Corti L., Corti L.G., 2012)

2.5.3 Acquisition system

All the sensors described above are connected to the same system of data acquisition, in which all channels converge (Figure 2.5.10). The acquisition is triggered by the signal of the first pressure transducer along the driven section: when the shock wave exceeds its position, the system begins to acquire data of all the sensors.
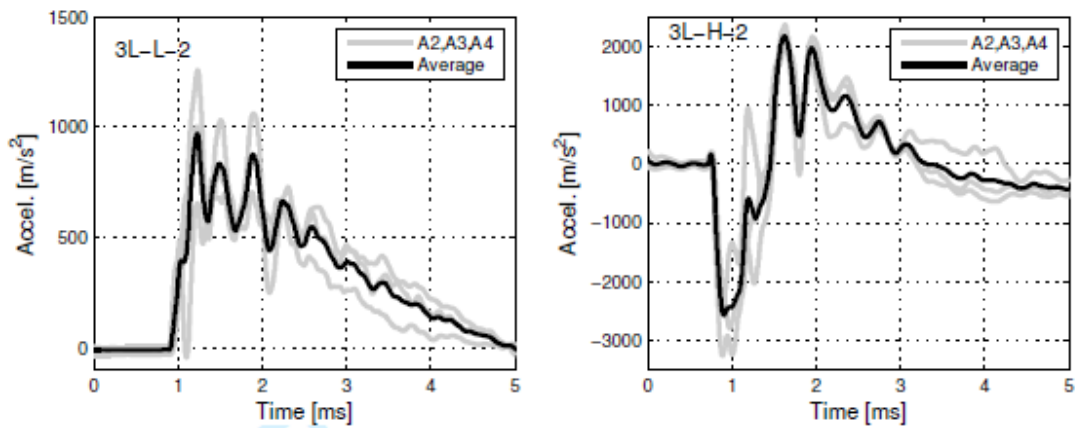

Figure 2.5.10 Cables between the shock tube with the control station (Corti L., Corti L.G., 2012)

2.6 Results of experimental tests (Colombo et al. 2013)

Here are some results of experimental tests.
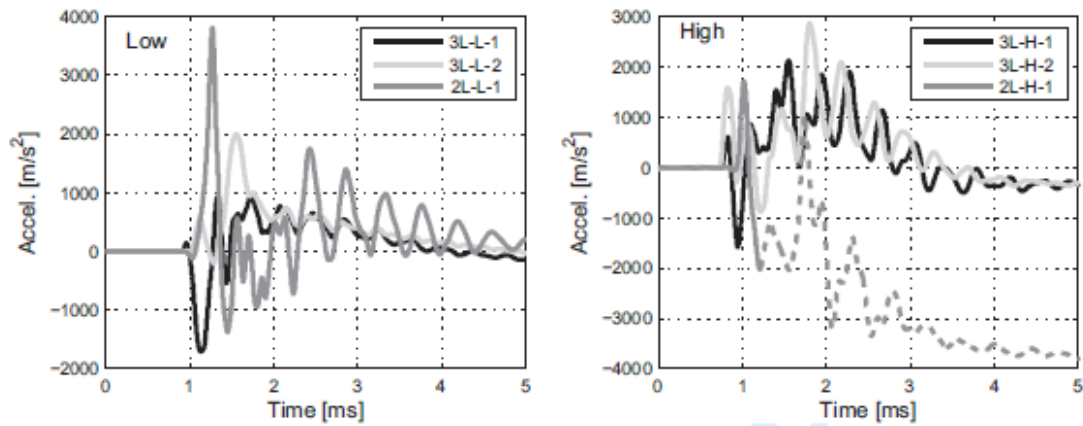
2.6.1 Axial specimen accelerations A1 for (a) low and (b) high pressure tests

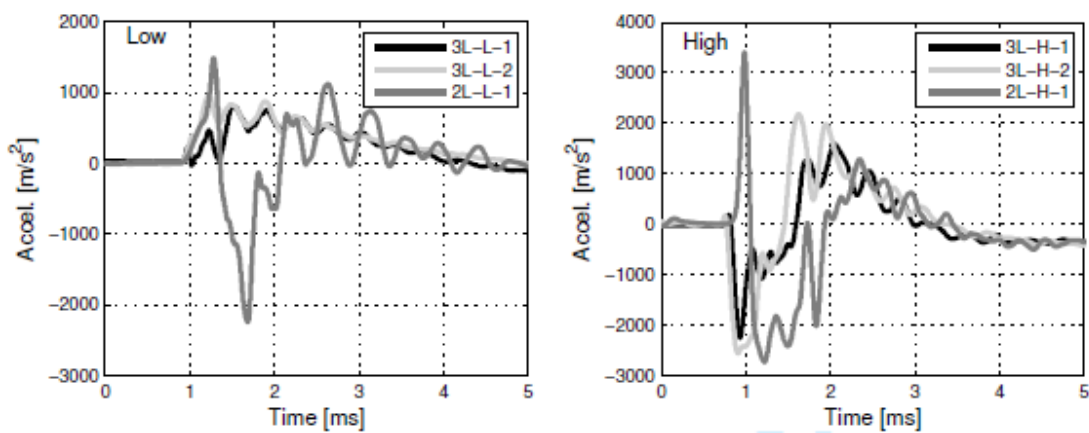2.6.2 Axial specimen accelerations A2-A4 for (a) low and (b) high pressure tests

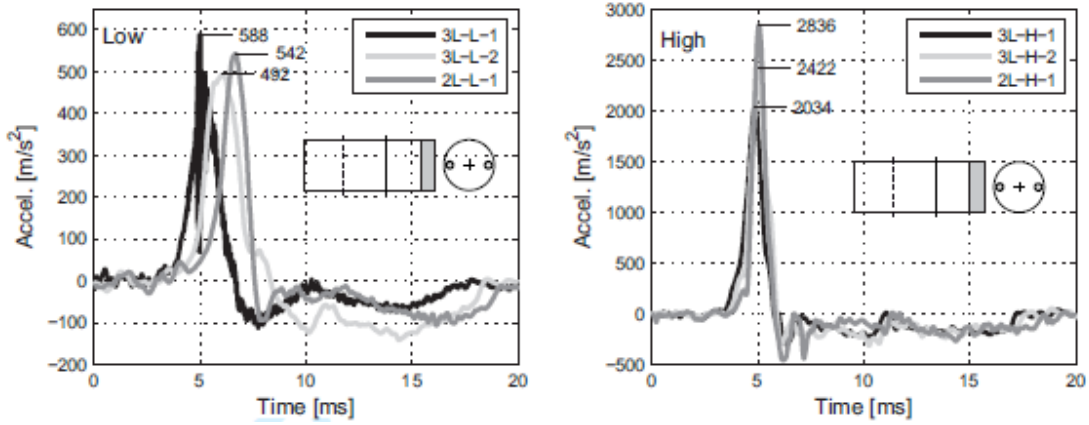Figure 2.6.3 Average axial specimen accelerations A2-A4 for (a) low and (b) high pressure tests

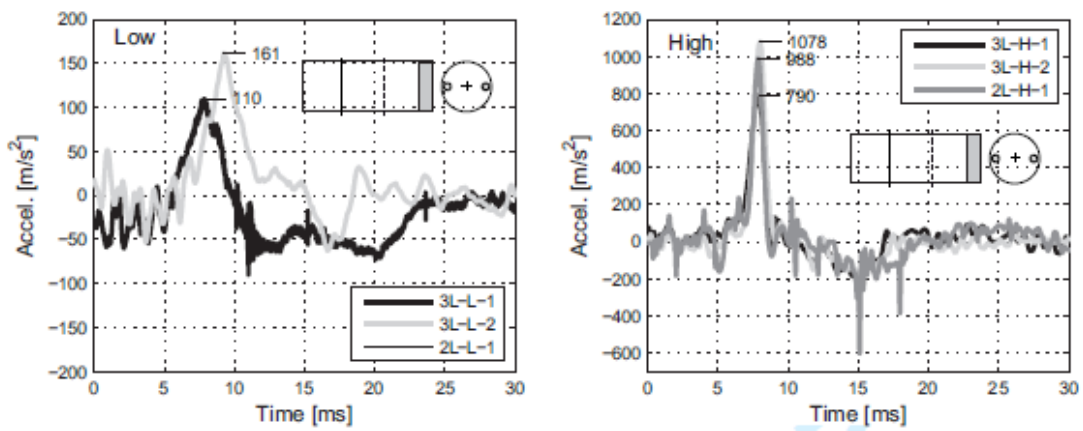Figure 2.6.4 Average axial soil accelerations A5, A5 for (a) low and (b) high pressure tests

Figure 2.6.5 Average axial soil accelerations A9, A11 for (a) low and (b) high pressure tests
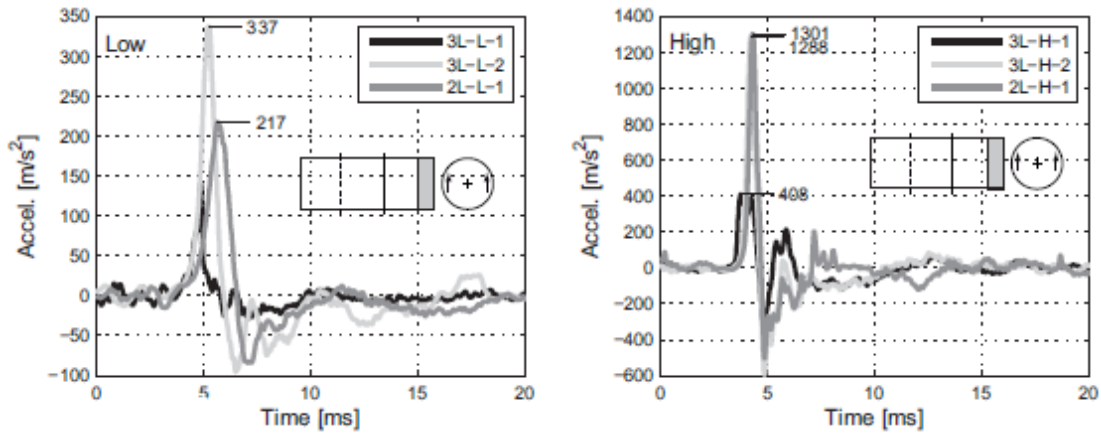

Figure 2.6.6 Average vertical soil accelerations A6, A8 for (a) low and (b) high pressure tests
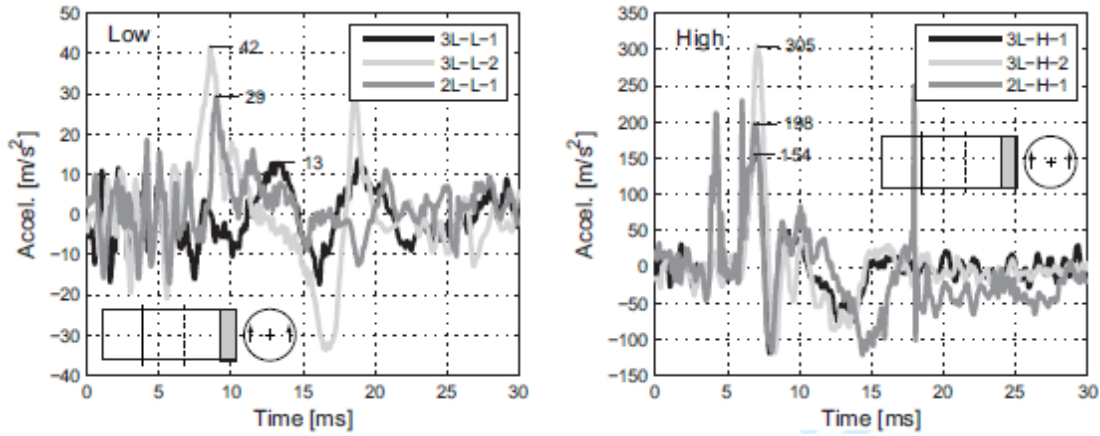
Figure 2.6.7 Average vertical soil accelerations A10, A12 for (a) low and (b) high pressure tests
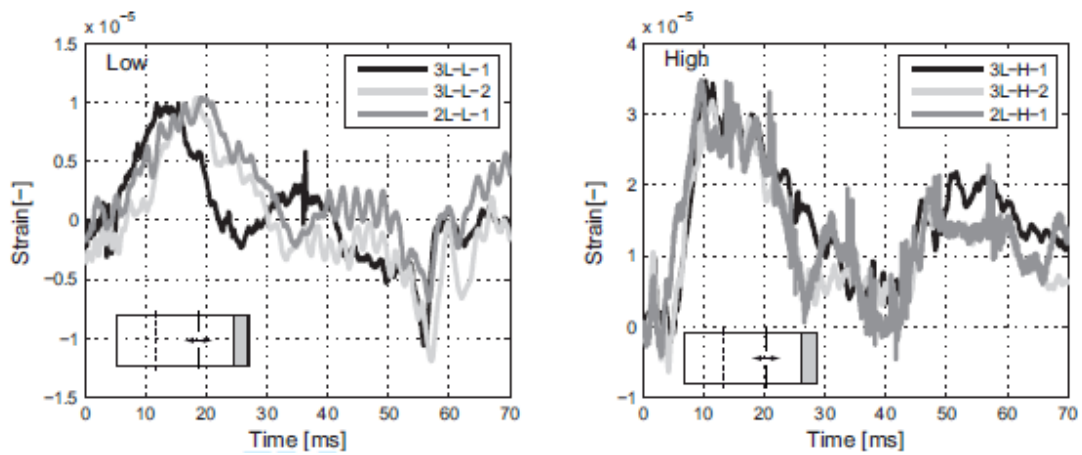

Figure 2.6.8 Longitudinal strain gauges SG1 for (a) low and (b) high pressure tests (section A-A)
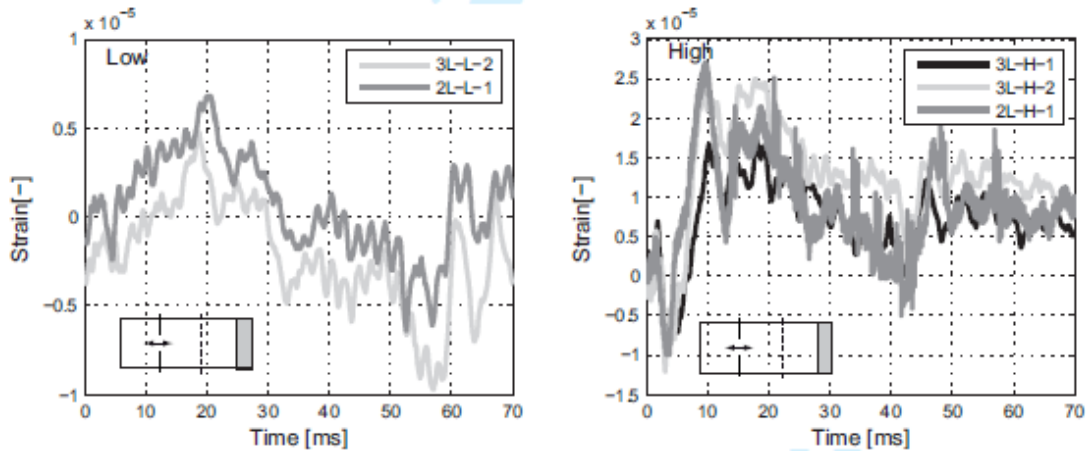

Figure 2.6.9 Longitudinal strain gauges SG4 for (a) low and (b) high pressure tests (section B-B)
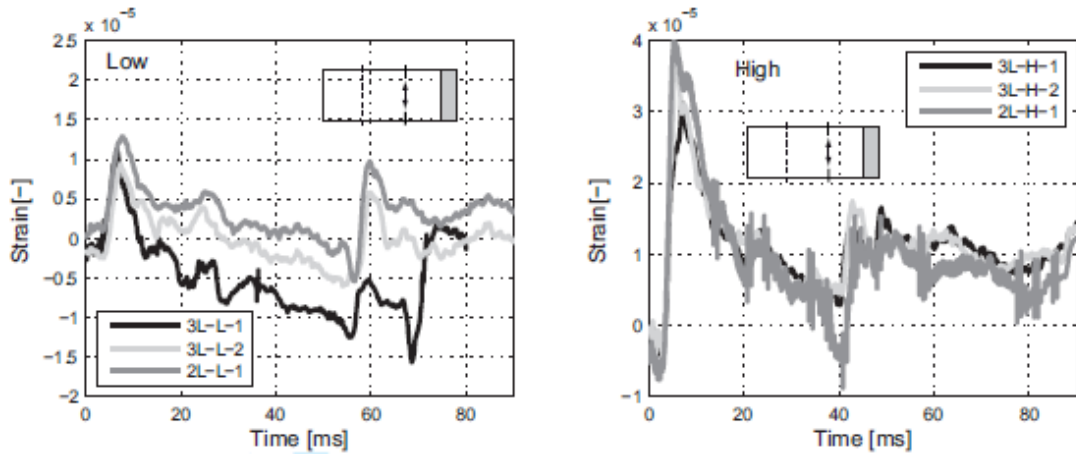
Figure 2.6.10 Average circumferential strain gauge values SG2, SG3 for (a) low and (b) high pressure tests (section A-A)
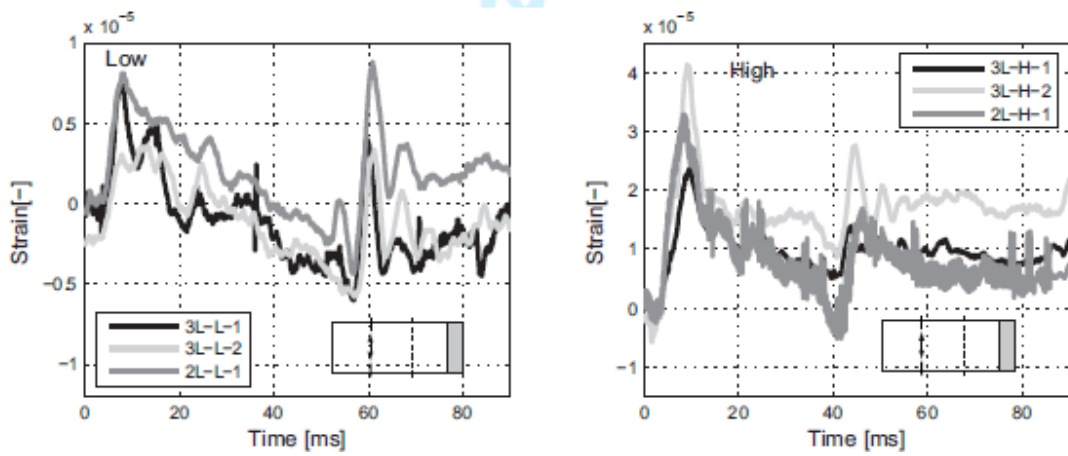

Figure 2.6.11 Average circumferential strain gauge values SG5, SG6 for (a) low and (b) high pressure tests (section B-B)
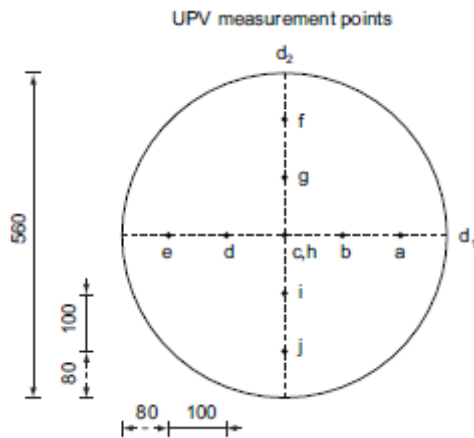

Figure 2.6.12 UPV measurement points (units in mm)

Chapter 3 Numerical Simulation Using PFC[3D]

3.1 Introduction of software

The analyses in this chapter were carried out by using the software PFC3D, produced by the company Itasca. PFC3D ("Particle Flow Code in 3 Dimensions") is able to model the movement and interaction of spherical particles through the method of discrete elements. These spherical particles are not intended as a point, but rather as bodies that occupy a finite space. The model is thus composed of distinct particles whose displacements are independent from that of the other spheres; they interact with each other only when they come into contact.
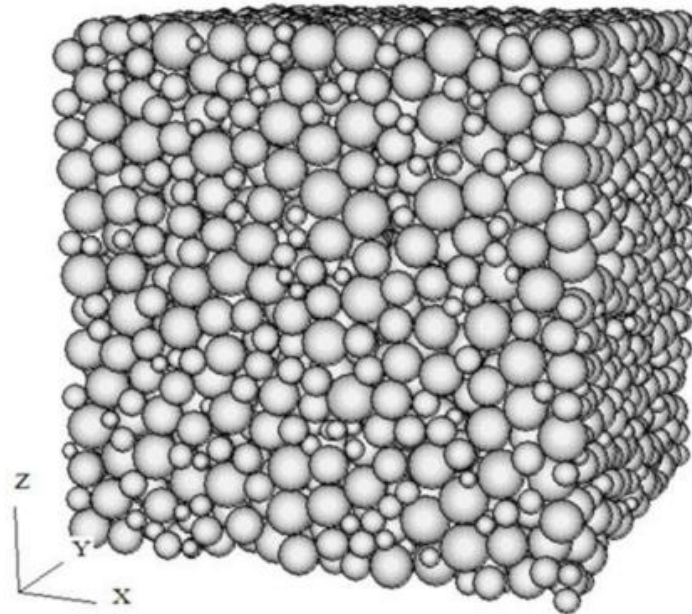
Figure 3.1.1 Numerical model of a sample of sand in cubic PFC3D (PFC3D manual)

Assuming the balls to be infinitely rigid, the relation between forces and displacements is described by the approach to deformable contacts, in which the contacts are idealized through springs with a given value of stiffness in the normal and tangential directions to the contact (figure 3.1.2).
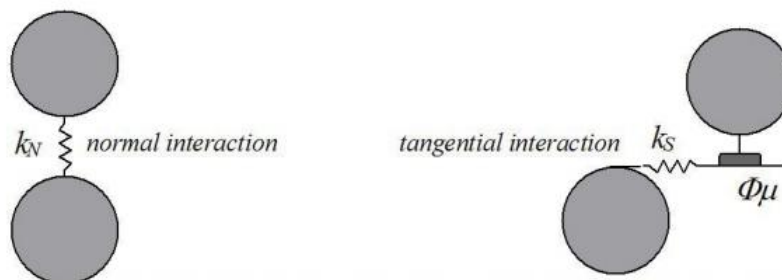

Figure 3.1.2 Schematic view of the approach of deformable contacts (PFC3D manual)

The mechanical behaviour of the system is then described by the forces that are exchanged between the particles in contact and the resulting movement of them. The system of forces can be under static equilibrium or may be such as to cause the movement of particles.

The assumptions on which the model is based are as follows:

- the particles are treated as rigid bodies;
- contacts occur on an area infinitely small;
- behaviour is adjusted to deformable contacts, according to which is permitted the overlap of rigid particles in the contact points;
- the amount of overlap is related to the contact forces through the laws of Newton force-displacement and the overlaps are smaller in scale compared to the size of the particles;

You can create links in the contacts between the particles; all the particles are spherical, however, they can be combined to create clump of arbitrary shape, or rigid bodies made from more particles that take therefore a deformable contour.

The hypothesis of infinite stiffness of the particles is valid when the most of deformation in the system is due to the mutual movements between the particles. In fact, the behaviour of entire groups of particles acts as granular materials like sand, this is well described with these assumptions. The deformation is caused mainly by sliding and relative rotation between the particles, which behave exactly as non-deformable rigid bodies. In order to obtain a good approximation of the mechanical behaviour of these systems, the precise modelling of the deformation of the single particle is not therefore necessary.

In addition to traditional applications related to granular materials, the software can also be used for the analysis of solids subject to initial and boundary conditions. In these models the behaviour of the continuum is approximated by treating the solid as a compact set of particles bounding together. This allows the development of the tensile forces within the model. The bonds created may be broken in case the forces acting on contacts exceed the corresponding values of tensile strength.

In addition to spherical particles, the program allows to create elements called walls, on which boundary conditions on the speed can be applied. The boundary conditions are then transmitted to the particles and the walls confine the particles to collapse. They are elements of zero thickness.

The equations of motion are satisfied for each sphere, but not to the walls, because their handling is specified by the user and it does not take account of the contact forces acting on them, which therefore does not affect the movement. These contact forces exist only between ball and ball and between the wall and ball, while between two walls there is not any exchange of forces.

Generally, the sample is loaded due to its own weight or due to the motion of the walls that can both translate and rotate. As described above, the forces cannot be applied directly on the walls, but only the respective speed can be applied on the walls. On the other hand, initial speeds, external forces and moments can be applied to particles. The latter two remain constant during the simulation. Conversely, the speed, if is not fixed by means of a specific command, it changes to the next step on the basis of the contact forces and the integration of the law of motion.

3.2 The method to separate components

PFC3D is classified as a distinct element code (DEM), as it allows the body to make individual displacements and rotations, it can automatically identify new contacts to the progress of the calculation. The distinct element method was introduced by Cundall in 1971 for the analysis of rock mechanics, and was later applied to the modelling of soil by Cundall and Strack in 1979.

PFC3D can be seen as an implementation of this simplified methodology due to the simplifying hypothesis of rigid spheres, as a method to separate elements which can completely handle polygonal particles.

In DEM the interaction between the particles is treated as a dynamic process in which the equilibrium states are changed continuously to achieve the balance of forces. The contact forces and displacements of a group of particles placed under load are obtained by tracing the movements of each particle. Such movements result from propagation through the particles of the disturbance caused, for example, by the motion of a wall, from the motion of the contiguous particles or by imposed volume forces. This is a dynamic process in which the speed of propagation depends on the physical properties of the discrete system.

The dynamic behaviour is represented numerically by an algorithm (time-stepping algorithm) where it is assumed that the velocities and accelerations are constant during each step (time step). To simulate the dynamic behaviour using temporal computational steps, the basic idea lies in the hypothesis for which the time-step is so small that the disturbances, during a single step, it can only spread to the adjacent particles and no further.

The forces acting on each particle are then determined solely by the interactions of the particles in contact with it. Since the speed at which a disturbance is able to propagate is a function of the physical properties of the discrete system, the time-step can be chosen in such a way to comply with these features. The use of this numerical scheme makes it possible to simulate the interaction of a large number of particles without excessive use of memory, or need iterative procedures.

3.3 Cycle of calculation

Calculations performed in DEM alternate the application of Newton's second law on the particles to the law on force-displacement contacts.

The Newton's second law is used to define the motion of each particle starting from the contact forces and volume and acting on the particle itself, while the force-displacement law is used to update the contact forces caused by the relative motion in each contact. Since the movement of the wall is imposed by the user, it is not applicable for it to the second law of Newton.

The calculation cycle is thus an algorithm based on temporal subsequent calculation steps. It consists of the successive application of the law of motion to each particle and force-displacement law to each contact, continuously updating the position of the particles. The force-displacement law is applied to update the contact forces, based on the relative motion between the two entities in contact. Subsequently, the resulting forces and moments resulting to contact produce the speed and the relative displacements of each ball by applying the law of motion.

The contacts sphere-sphere and sphere-wall are formed and destroyed automatically during the simulation. The calculation cycle is illustrated in figure 3.3.1; the calculations described in each pane can be effectively performed in parallel.
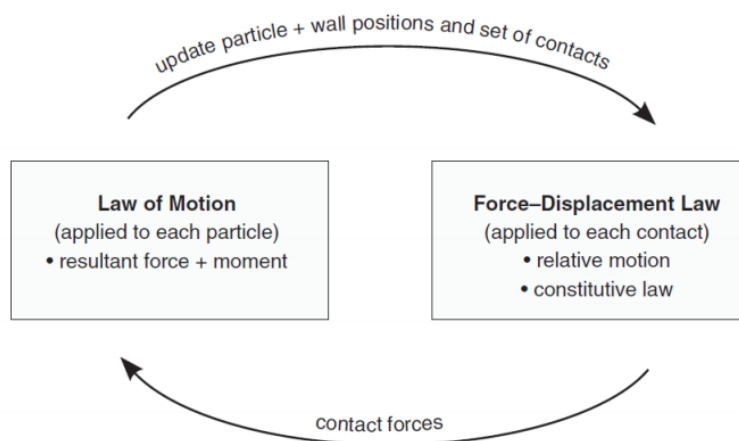

Figure 3.3.1 The two stages of calculation

3.3.1 The force - displacement law

The force-displacement law correlates the relative displacement between the two entities in contact and the forces acting on these entities. For types of contact (sphere-sphere or sphere-wall), forces and moments arise at the point of contact. For contacts sphere-sphere it can also act as a cohesive force (bond). The following describes only the calculation of contact forces without such cohesion.

The force-displacement law is applied to the contact point. This point is defined by a contact plane and a unit vector which is normal to the plane and crosses through it. The contact point is located within the volume defined by the interpenetration of the two objects (sphere-sphere or sphere-wall). For the sphere-sphere type contacts the normal unit is directed as the line joining the centres, while the ball-wall contact is directed as the shortest distance between the centre of

the sphere and the wall. The contact force is then decomposed into two components: the normal component acts in the direction of the normal vector, the tangential component of cut lies in the plane. The force displacement law connects these two components of force with the relative displacements through the normal and tangential contact stiffness. Figure 3.3.2 shows a generic sphere-sphere contact.
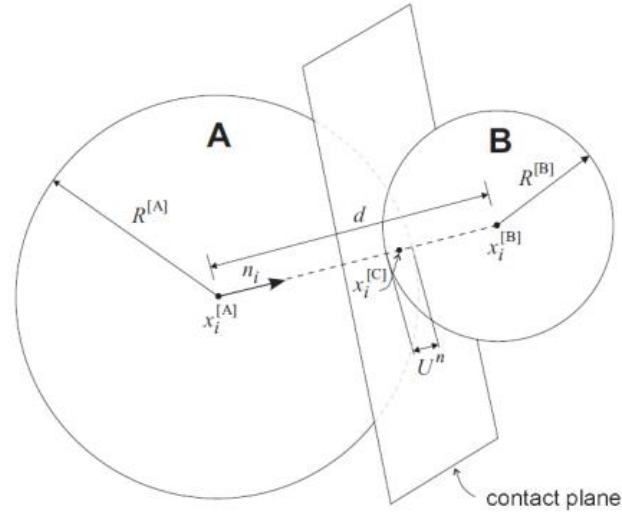

Figure 3.3.2 The contact sphere-sphere (PFC3D manual)

The unit normal vector n_i to sphere A and B is defined as follow:

$$n_i = \frac{x_i^{[B]} - x_i^{[A]}}{d}$$
[Eq. 3.3.1 (PFC3D manual)]

Where $x_i^{[B]}$ and $x_i^{[A]}$ are the centre positions of the sphere, and d is the distance between them.

$$d = \left| x_i^{[B]} - x_i^{[A]} \right| = \sqrt{\left(x_i^{[B]} - x_i^{[A]} \right) \left(x_i^{[B]} - x_i^{[A]} \right)}$$
[Eq. 3.3.2 (PFC3D manual)]

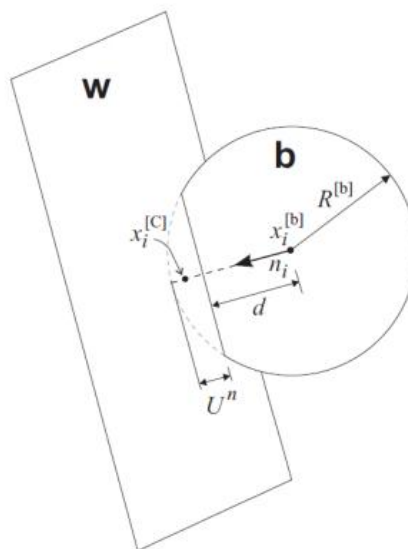As for the ball-wall contacts the reasoning is similar (Figure 3.3.3).

Figure 3.3.3 The wall-ball contact (PFC3D manual)

34

The overlap U^n is defined as the relative displacement to contact in the normal direction, is calculated as follow:

$$U^n = \begin{cases} R^{[A]} + R^{[B]} - d & ball - ball \\ R^{[b]} - d & ball - wall \end{cases}$$ [Eq. 3.3.3 (PFC3D manual)]

Where $R^{[i]}$ is the radius of sphere i.

The contact point is located as follow:

$$x_i^{[C]} = \begin{cases} x_i^{[A]} + \left(R^{[A]} - \frac{1}{2} U^n \right) \underline{n_i} & ball - ball \\ \underline{x_i^{[b]}} + \left(R^{[b]} - \frac{1}{2} U^n \right) \underline{n_i} & ball - wall \end{cases}$$ [Eq. 3.3.4 (PFC3D manual)]

As described previously, the carrier of the contact force, (which represents the action of the sphere A to sphere B for contact sphere-sphere and the action of the ball to the wall for contacts sphere-wall) is broken down into normal and tangential components to the plane, is defined as follow:

$$\underline{F_i} = \underline{F_i^n} + \underline{F_i^s}$$ [Eq. 3.3.5 (PFC3D manual)]

Where $\underline{F_i^n}$ is the normal component and $\underline{F_i^s}$ is the tangential component.

The normal component of contact force is calculated as follow:

$$\underline{F_i^n} = K^n U^n \underline{n_i}$$ [Eq. 3.3.6 (PFC3D manual)]

Where K^n is the normal stiffness of the contact point, and it represented by a constant spring in the approach to deformable contacts. It is important to note that this stiffness is a secant modulus that binds the total displacement with the total force. While the tangential stiffness is a tangent modulus that binds the incremental values of breaking force and tangential displacement:

$$\Delta F_i^s = -k^s \Delta U_i^s$$ [Eq. 3.3.7 (PFC3D manual)]

When the contact is created, the total cutting force is initialized to zero. Any subsequent increase of the displacement is due to an increase of the corresponding cutting force, which is thus updated. The movement of the contact is evaluated and updated at each time-step, and through which it updates the cutting force on the contact, that takes into account the rotation of the normal vector.

3.3.2 The law of motion

The motion of a single rigid sphere is determined from the force. It can be described in terms of translational motion of the centre of gravity and the rotational motion of the particle. The first one is described in terms of the position x_i, the velocity $\dot{x}_i$, and the acceleration $\ddot{x}_i$; the second one is described in terms of the angular velocity ω_i and the angular acceleration $\dot{\omega}_i$.

The equations of motion can be expressed as two vector equations: one that binds the resultant forces to the translational motion, and the other one that binds the resultant moment to the rotational motion. The equation for the translational motion vector is written in the form:

$$\underline{F_i} = m \left(\underline{\ddot{x}_i} - \underline{g_i} \right)$$ [Eq. 3.3.8]

Where $\underline{F_i}$ is the resultant force, is the sum of external forces acting on the ball, m is the mass,

and g_i is the gravity acceleration.

The equation of rotational motion is written as follow:

$$\underline{M_i} = \underline{\dot{H}_t}$$

[Eq. 3.3.9]

Where $\underline{M_i}$ is the resultant moment of sphere, and $\underline{\dot{H}_t}$ is the angular moment of particle.

This equation is referred to a local coordinate system placed in the centre of the sphere. In the case of homogeneous spheres, the centre of the sphere coincides with the centre of mass and under this assumption the equation above can be rewritten as:

$$\underline{M_i} = I\underline{\dot{\omega}_t} = \left(\frac{2}{5}mR^2\right)\underline{\dot{\omega}_t}$$

[Eq. 3.3.10]

In which I are the principal inertia moments of the particles, $\underline{\dot{\omega}_t}$ are the angular acceleration and $\underline{M_i}$ are the components of the resultant moment, all refer to the same principal axes of inertia.

These two equations of motion are then integrated using a procedure of centred finite differences which involves a time-step Δt. The quantities of $\dot{x}_t$ and ω_i are measured in half interval, or $t \pm n\Delta t/2$, while $\ddot{x}_i$, x_i and $\dot{\omega}_i$ are measured in the whole interval ($t - t\Delta, t, t + \Delta t$, ecc).

So that the translational and rotational acceleration are calculated as follow:

$$\ddot{x}_i^{(t)} = \frac{1}{\Delta t}\left(\dot{x}_i^{(t+\frac{\Delta t}{2})} - \dot{x}_i^{(t-\frac{\Delta t}{2})}\right)$$

[Eq. 3.3.11]

$$\dot{\omega}_i^{(t)} = \frac{1}{\Delta t}\left(\omega_i^{(t+\frac{\Delta t}{2})} - \omega_i^{(t-\frac{\Delta t}{2})}\right)$$

[Eq. 3.3.12]

The equation of motion is:

$$\dot{x}_i^{(t+\frac{\Delta t}{2})} = \dot{x}_i^{(t-\frac{\Delta t}{2})} + \left(\frac{F_i^{(t)}}{m} + g_i\right)\Delta t$$

[Eq. 3.3.13]

$$\omega_i^{(t+\frac{\Delta t}{2})} = \omega_i^{(t-\frac{\Delta t}{2})} + \left(\frac{M_i^{(t)}}{I}\right)\Delta t$$

[Eq. 3.3.14]

Finally, the speeds calculated in the equations above are used to update the position of the particles' centre:

$$x_i^{(t+\Delta t)} = x_i^t + \dot{x}_i^{(t+\frac{\Delta t}{2})}\Delta t$$

[Eq. 3.3.15]

So, the calculation cycle can be schematized as follow: determine the value of $\dot{x}_i^{(t-\frac{\Delta t}{2})}$, $\omega_i^{(t-\frac{\Delta t}{2})}$, x_i^t, $F_i^{(t)}$ and $M_i^{(t)}$, they are used for get the value of $\dot{x}_i^{(t+\frac{\Delta t}{2})}$ and $\omega_i^{(t+\frac{\Delta t}{2})}$. After that update the position for the next step $x_i^{(t+\Delta t)}$. The values of $F_i^{(t+\frac{t\Delta}{2})}$ and $M_i^{(t+\frac{\Delta t}{2})}$ to be used in the next step, are obtained by application of forces-displacement law.

3.4 Determination of step calculation of time

The equations of motion are integrated by using the scheme of PFC3D, central finite differences described above. This solution remains stable only when the time step is less than or equal to a critical value, which will therefore be taken as the calculation step in the analysis. Because the system is constantly changing during a simulation, to calculate this critical time step, the following simplified procedure is used, applied at the beginning of each step.

First, consider a mass-spring system with point mass and spring stiffness k (Figure 3.4.1).
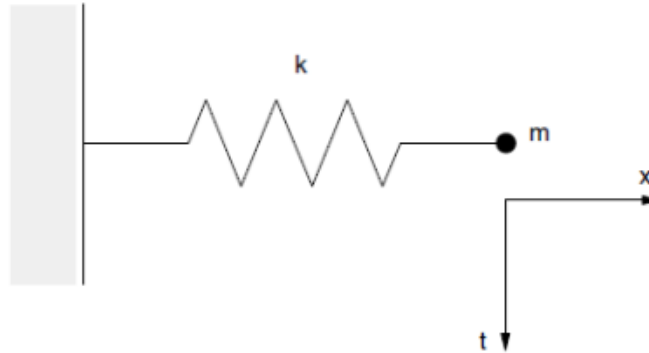

Figure 3.4.1 Mass-spring system (PFC3D manual)

The motion of the point is described in differential equations as follow:

$$-kx = m\ddot{x}$$ [Eq. 3.4.1]

The critical time-step calculated with a finite difference method of second order, is given by:

$$t_{crit} = \frac{T}{\pi}$$ [Eq. 3.4.2 (PFC3D manual)]

With the period of system equal to $T = 2\pi\sqrt{m/k} \Rightarrow t_{crit} = 2\sqrt{m/k}$ [Eq. 3.4.3].

Next, consider an infinite number of point masses and springs. In this system, the smallest period is obtained when the masses move in opposite motion and synchronized, so that the centre of each spring does not result in movement. The motion of each mass point can be described by the two equivalent systems shown in Figure 3.4.2 (b) and (c).
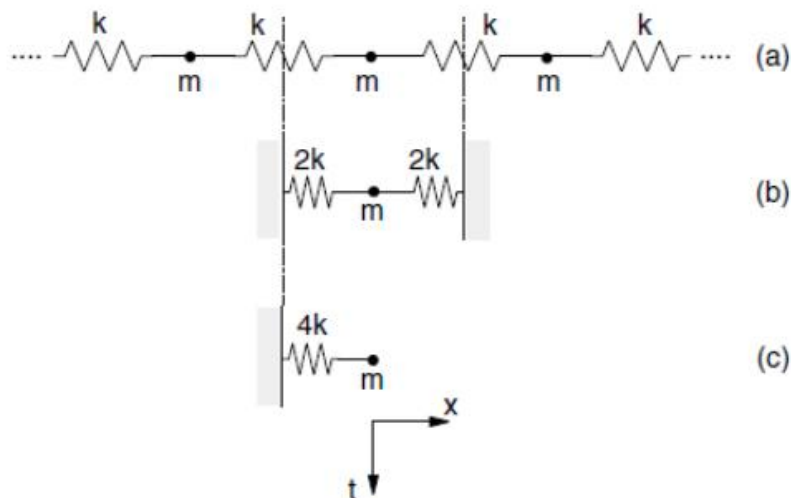

Figure 3.4.2 Mass-spring systems in series (PFC3D manual)

k is the stiffness of each spring, critical time-step for the latter system turns out to be:

$$t_{crit} = 2\sqrt{m/4k} = \sqrt{m/k}$$ [Eq. 3.4.4]

Up to now what has been described concerns the translational motion. For the rotational motion, the system characterizes it in the same way, with the moment of inertia substituent the mass m, and the stiffness replaced by the rotational stiffness:

$$t_{crit} = \sqrt{I/k^{rot}}$$ [Eq. 3.4.5]

The systems modelled with PFC3D three-dimensional systems are composed of discrete bodies (or spherical agglomerates of different shape) and springs. Each body may have different mass and each spring may have different stiffness. The time step is then determined for each body by applying the equations described above for each degree of freedom, assuming that these are independent. The stiffness is determined by adding up the contributions of all the contacts. The critical time-step is considered to be the minimum of all those calculated simultaneously for all the bodies and for all degrees of freedom. Consequently, since the number of contacts varies in subsequent iterations, even the numerical value of the time step may be subject to slight variations during the analysis.

3.5 Damping

The energy supplied to the spheres is dissipated by friction. Nevertheless, it is possible to add a more meaningful dissipative factor (damping), capable of dissipating kinetic energy and useful especially in static analysis to accelerate the convergence to the solution. There are two types of damping: local and viscous. The local damping acts on each sphere, on which a damping force is applied proportionally and opposite to the unbalanced force that determines the motion, on the contrary the viscous damping is applied with the shock absorbers normally and tangentially on the single contact. These shock absorbers act in parallel with the model of the existing contact and determine forces proportionally to the relative speed difference between the two bodies in contact.

Usually, the local damping appears to be the most appropriate form to establish the balance and for conducting simulations of quasi-static deformation. In the case in which dynamic simulations are requested, it is possible to adopt two different choices: the first consists in the use of viscous damping to the contacts; the second is obtained by setting the local damping coefficient to low values, so that there is not a large dissipation of dynamic wave energy.

The local damping used in PFC3D consists in a force $F_{(i)}^d$ that is given by the equation of motion:

$$F_{(i)}^d + F_{(i)} = m_{(i)}a_{(i)}$$ [Eq. 3.5.1]

These equation and vector of the ball are decomposed in the six degrees of freedom (three translational and three rotational).

$$m_{(i)}a_{(i)} = \begin{cases} m\ddot{x}_{(i)} & per\ i = 1,2,3 \\ I\dot{\omega}_{(i-3)} & per\ i = 4,5,6 \end{cases}$$ [Eq. 3.5.2]

The direction of the damping force will be opposite to the velocity vector of the ball in motion. The module, however, is proportional to the forces $F_{(i)}$ applied to the sphere through a multiplicative factor α:

$$F_{(i)}^d = -\alpha |F_{(i)}| sign(v_{(i)})$$ [Eq. 3.5.3]

Where $v_{(i)}$ is the generalized velocity:

$$v_{(i)} = \begin{cases} \dot{x}_{(i)} & per\ i = 1,2,3 \\ \omega_{(i-3)} & per\ i = 4,5,6 \end{cases}$$ [Eq. 3.5.4]

This form of damping has the advantage that it does not give problems in quasi-static situations, being damped only in acceleration of motion, and just have a damping constant α and non-dimensional constant.

3.6 Linear model of contact

PFC3D offers the possibility of choosing between different models of contact, of which the two most used are the linear model and the model "Hertz". In the following only the contact of the linear type is described, used for this study, paying attention to the description of the parameters associated with it.

3.6.1 Stiffness

The stiffness of a contact is defined by the normal and tangential stiffness, of the two entities in contact (sphere-sphere or sphere-wall). As already described, they relate the contact forces to the relative displacements in the two directions.

The normal stiffness is a secant stiffness, which binds total forces and displacements in the normal direction to the plane of contact:

$$F_i^n = K^n U^n n_i \qquad \text{[Eq. 3.6.1 (PFC3D manual)]}$$

The shear stiffness is instead a tangent stiffness, which correlates the strength increments and displacement:

$$\Delta F_i^S = -k^S \Delta U_i^S \qquad \text{[Eq. 3.6.2 (PFC3D manual)]}$$

In the model of linear contact, the stiffness is determined by assuming that of both elements in contact act in series:

$$K^n = \frac{k_n^{[A]} k_n^{[B]}}{k_n^{[A]} + k_n^{[B]}} \qquad \text{[Eq. 3.6.3 (PFC3D manual)]}$$

$$K^S = \frac{k_S^{[A]} k_S^{[B]}}{k_S^{[A]} + k_S^{[B]}}$$

In addition, it is important to note that for this model, the normal secant stiffness is equal to the normal tangent stiffness:

$$k^n = \frac{dF^n}{dU^n} = \frac{d(K^n U^n)}{dU^n} = K^n \qquad \text{[Eq. 3.6.4 (PFC3D manual)]}$$

3.6.2 Friction

The contact model allows to obtain a linear behaviour of slipping, so that the two entities can slide relatively on each other. This is possible by imposing zero strength in the normal direction and limiting the shear force. Such behaviour is defined by a coefficient of friction μ to contact [dimensionless], where μ appears to be the minimum coefficient of friction between the two bodies in contact.

$$\mu = \tan(\varphi_\mu) \qquad \text{[Eq. 3.6.5]}$$

Where the friction angle φ_μ is of the virtual particle, which must be the object of initial calibration.

The maximum allowable shear force to the contact is thus defined:

$$F_{max}^S = \mu |F_i^n| \qquad \text{[Eq. 3.6.6]}$$

When $\left|F_i^S\right| > F_{max}^S$, the slipping is allowed for the next cycle of calculation by placing F_i^S equal to F_{max}^S.

3.6.3 Cohesion

PFC3D allows simulating the behaviour of cohesive particles to contacts. This bond can be seen as a sort of glue joining the two entities in the single point of contact that only transmits forces. Once the bond is formed at the contact between two spheres, it continues to exist until the limit is reached beyond which it fails. The particles can be linked to each other, but not to the walls.

In the model, the binding of contact is implemented assuming a tensile strength for the normal spring and a maximum resistance to the break for the tangential spring. In this way, the breaking force is limited only by the shear strength and no longer by the friction coefficient, the relative sliding between the two spheres occurs. The presence of a tensile strength for the normal direction allows, instead, the formation of the tensile forces which tend to bring the balls to one another. These forces are derived from the equation below, placing shift values $U^n < 0$ (there is no overlap of the spheres to the contact).

$$F_i^n = K^n U^n n_i \qquad \text{[Eq. 3.6.7 (PFC3D manual)]}$$

When the normal tensile force equals or exceeds the ultimate tensile strength, the bond is broken, both the normal contact force and the shear force become null. Conversely, if the tangential forces are equal to or exceed the strength corresponding to the cut, the bond is broken, but the contact forces are not altered, unless the tangential forces do not exceed the limit of friction imposed.

The force-displacement behaviour that relates the normal and shear components of the contact forces with the corresponding displacements of the particles is shown in the following figures 3.6.1 and 3.6.2.
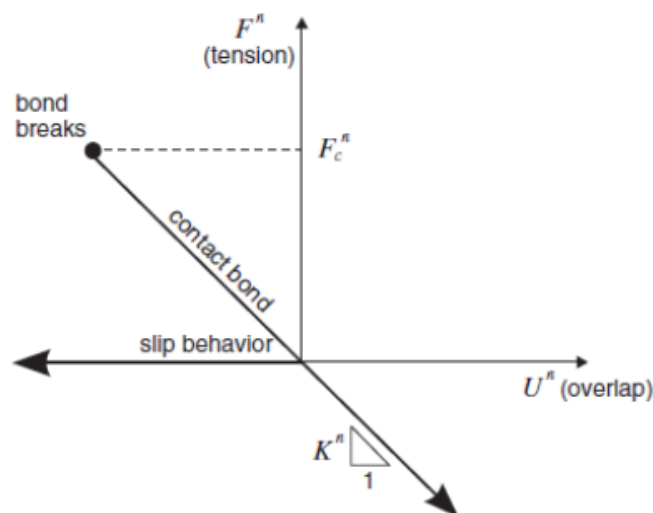

Figure 3.6.1 The relationship force/displacement with cohesion (normal stiffness)
(PFC3D manual)

In the figure above, F^n is the normal contact force, where $F^n > 0$ indicates tensile when U^n is relative normal displacement, where $U^n > 0$ indicates the overlap of the particles.
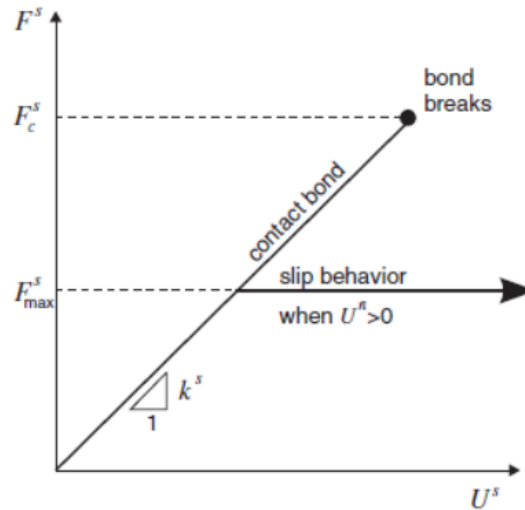
41

Figure 3.6.2 The relationship force / displacement with cohesion (tangential stiffness) (PFC3D manual)

In the figure above, F^S is the total shear force on the contact, while U^S is the total displacement measured relative tangentially to the point where it has come to create the bond.

A general pattern of behaviour at the contact between two distinct elements is shown in the figure below (Figure 3.6.3).
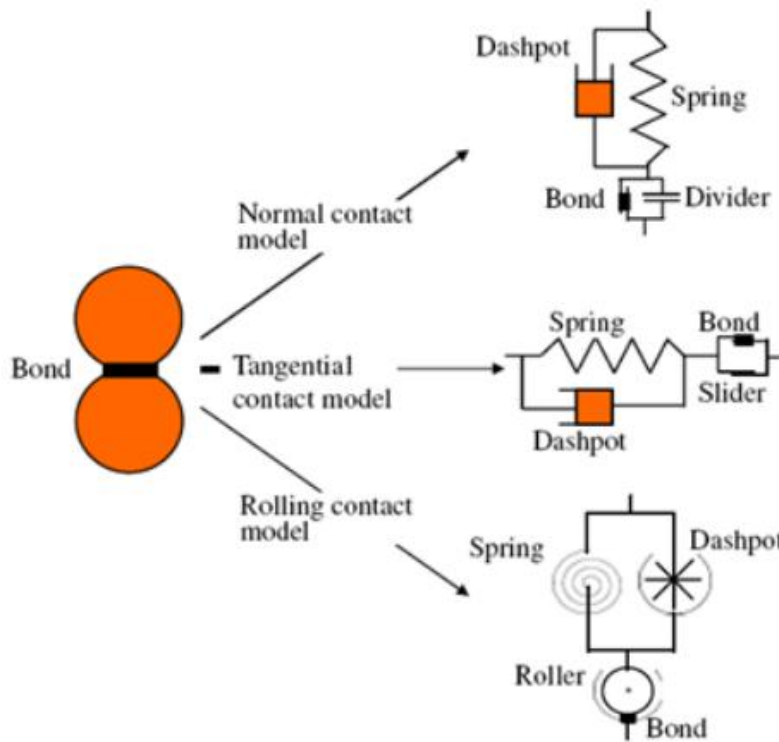

Figure 3.6.3 Behaviour at the contact between two elements (PFC3D manual)

3.7 Numerical model

The numerical model that simulates this shock-tube test has already been created by other researchers. Here is a brief introduction of the model, the test procedure simulated and the numerical results. Much more details can be found in the master degree dissertation of Francesco Bonacina and Giulio Dell'era (2013).

The tube chamber is modelled as walls without thickness. The length is 1.55m and the radius is 0.2915m figures 3.7.1 and 3.7.2.
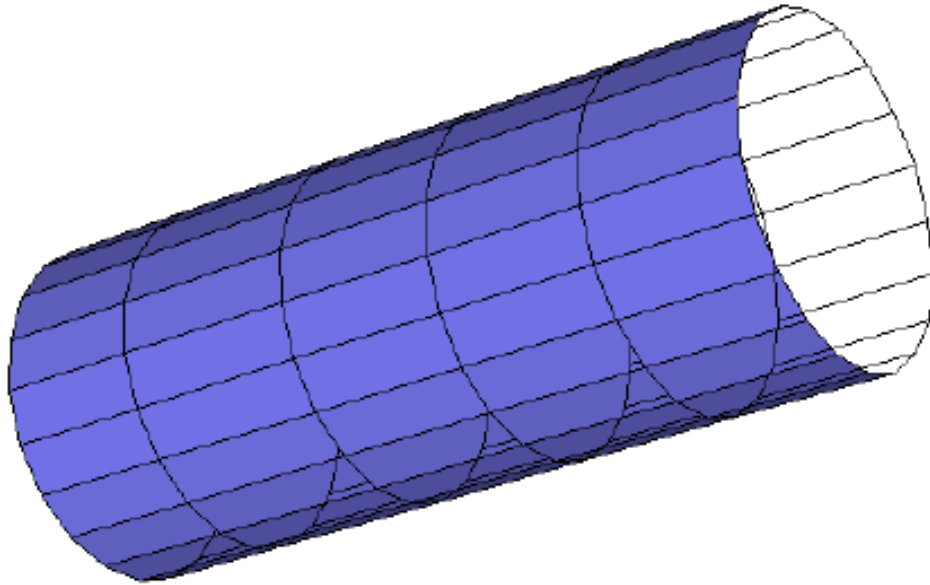
Figure 3.7.1 Modelled chamber with PFC3D (Bonacina F., Dell'era G. 2013)
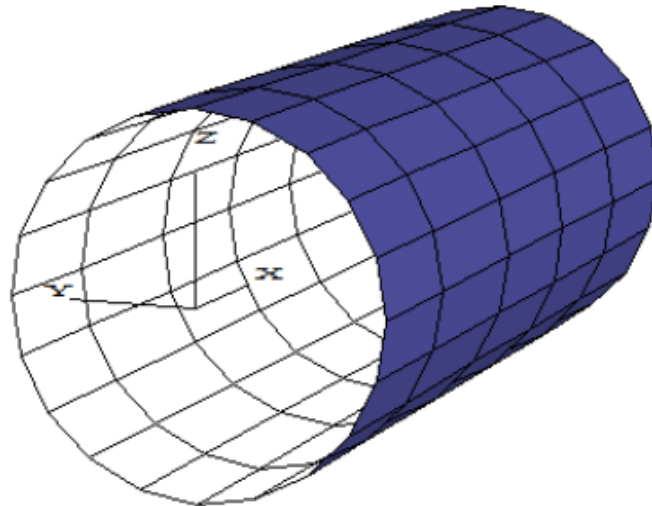
Figure 3.7.2 The reference system of numerical model (Bonacina F., Dell'era G. 2013)

The sand inside the chamber is modelled as discrete balls full filled in the volume that is enclosed by the walls (figure 3.7.3(a)). In order to make the sand have the same properties used in the test, The total length of sand is set 1.42m, the porosity is 0.52 and the density is 1400kg/m³ (figure

3.7.3(b)). The grain composition is simplified as figure 3.7.4.
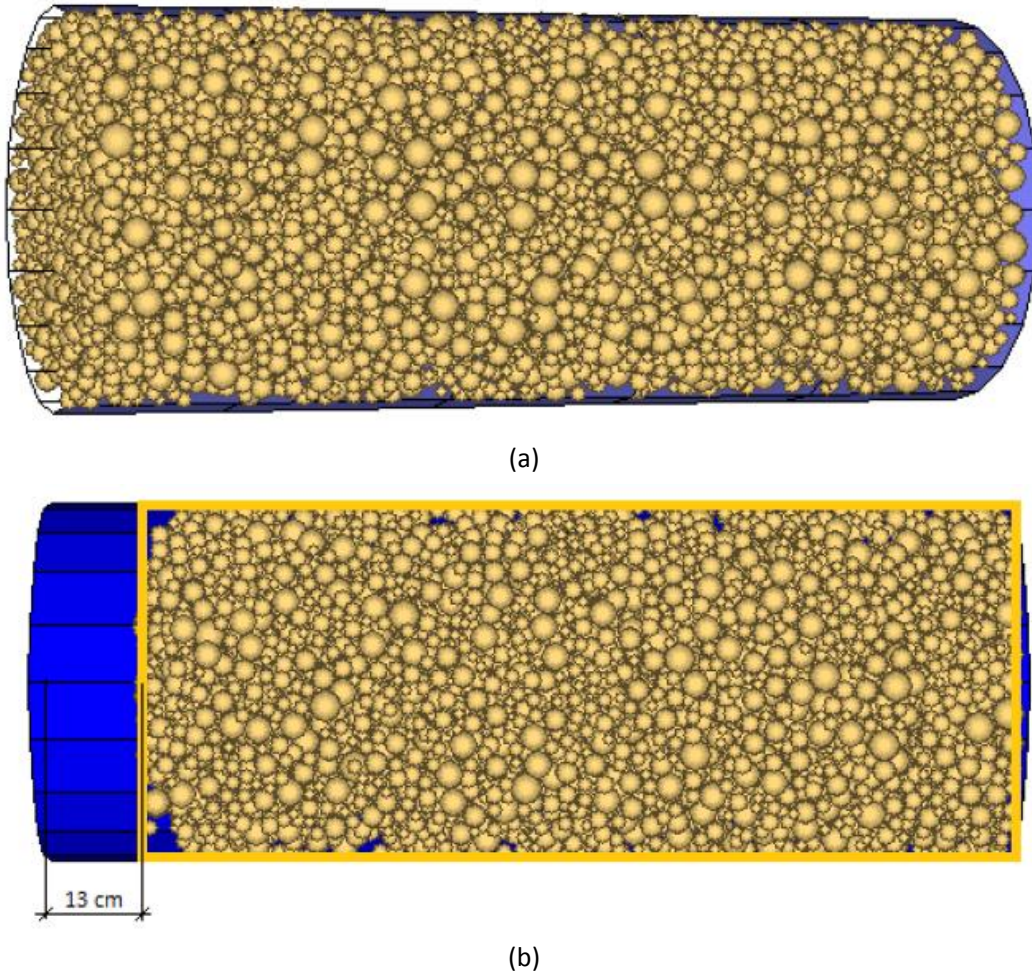

(a)

13 cm

(b)

Figure 3.7.3 The model of sand inside the chamber (Bonacina F., Dell'era G. 2013)
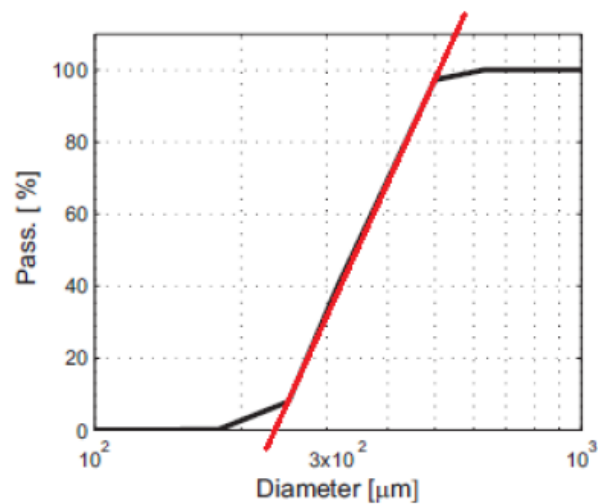

Figure 3.7.4 Simplification of the curve of grain size distribution in modelling in PFC3D
(Bonacina F., Dell'era G. 2013)

The friction coefficient between the balls is constant equal to 0.35, the stiffness between balls is

satisfied $K^n : K^S = 4 : 1$, (In order to obtain a realistic value of Poisson's ratio, this ratio should be around 0.25). So far, the model structure is completed.

The loading procedure is divided into three steps.

Apply the gravity in x axis direction (figure 3.7.5).

Rotate from vertical to horizontal, change the gravity direction into y axis (figure 3.7.6).

Add static confinement in x axis (figure 3.7.7).
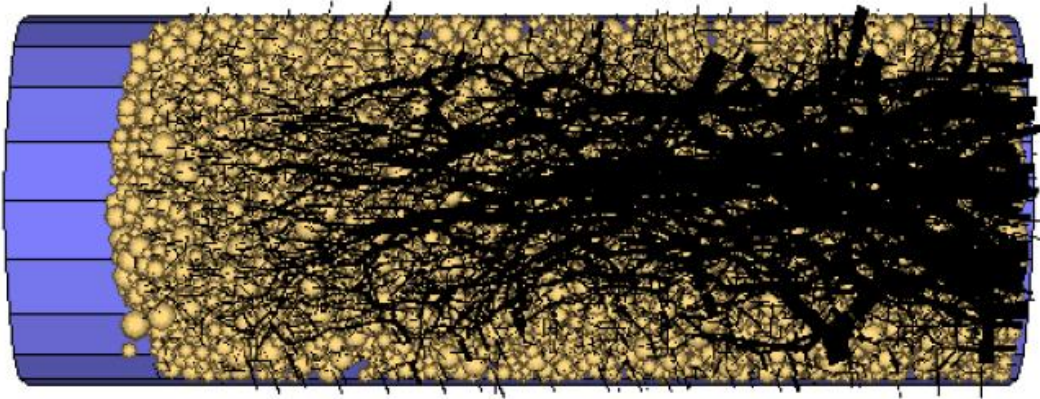
Load the test wave in x axis (figure 3.7.8).

Figure 3.7.5 The model after the application of gravity in x axis
(Black branches means the compressive stress) (Bonacina F., Dell'era G. 2013)
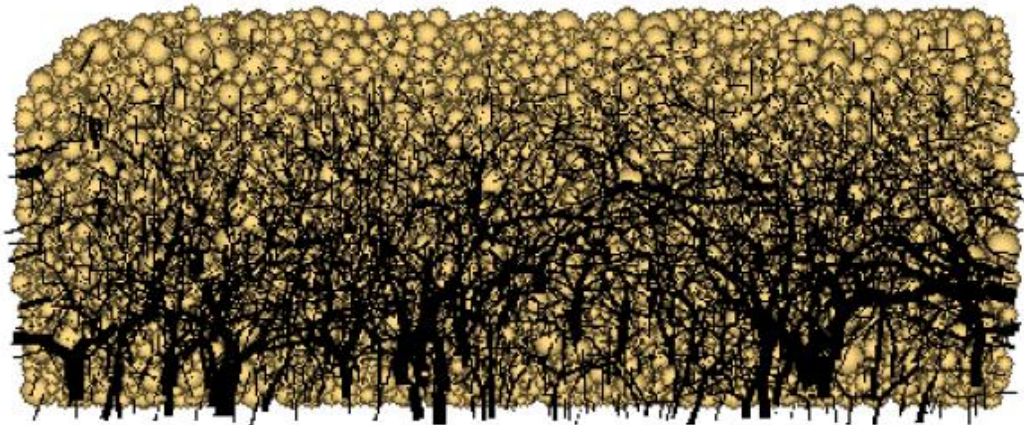
Figure 3.7.6 The modelled sand after rotation of gravity
(Black branches means the compressive stress) (Bonacina F., Dell'era G. 2013)
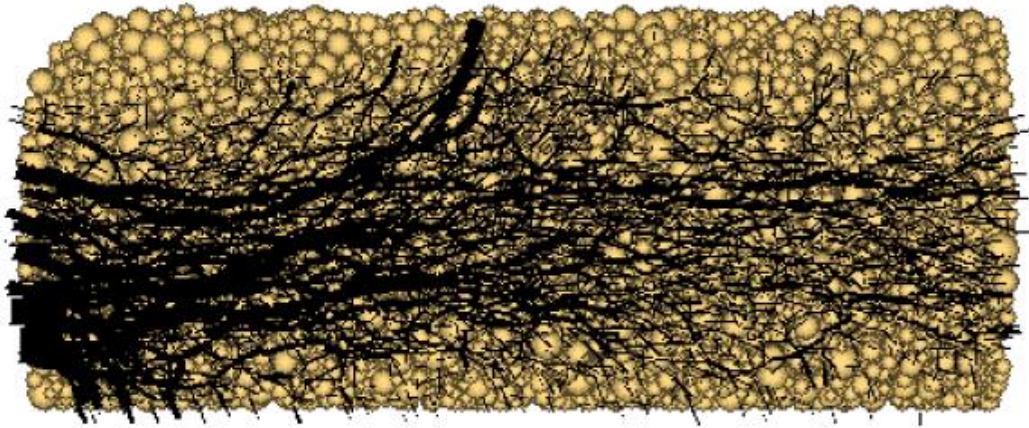
Figure 3.7.7 The sample of sand as a result of the application of static confinement
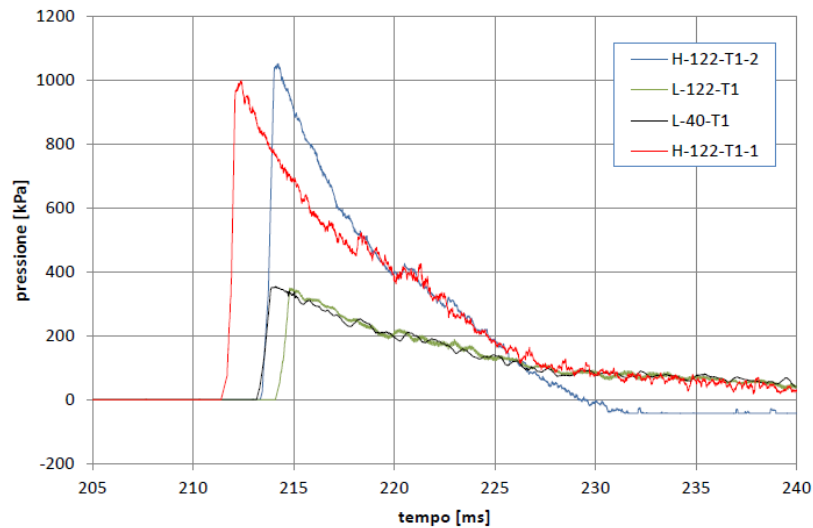(Black branches means the compressive stress) (Bonacina F., Dell'era G. 2013)

Figure 3.7.8 The input data of test wave (Bonacina F., Dell'era G. 2013)

3.8 Numerical results (Bonacina F., Dell'era G. 2013)

There're many numerical results from PFC3D model, such as accelerations, longitudinal forces, longitudinal displacement, velocities of four load waves. Here only longitudinal accelerations of test H-122-T-1-1 are shown. More details of PFC3D model is referred to the master degree dissertation of Francesco Bonacina and Giulio Dell'era (2013).
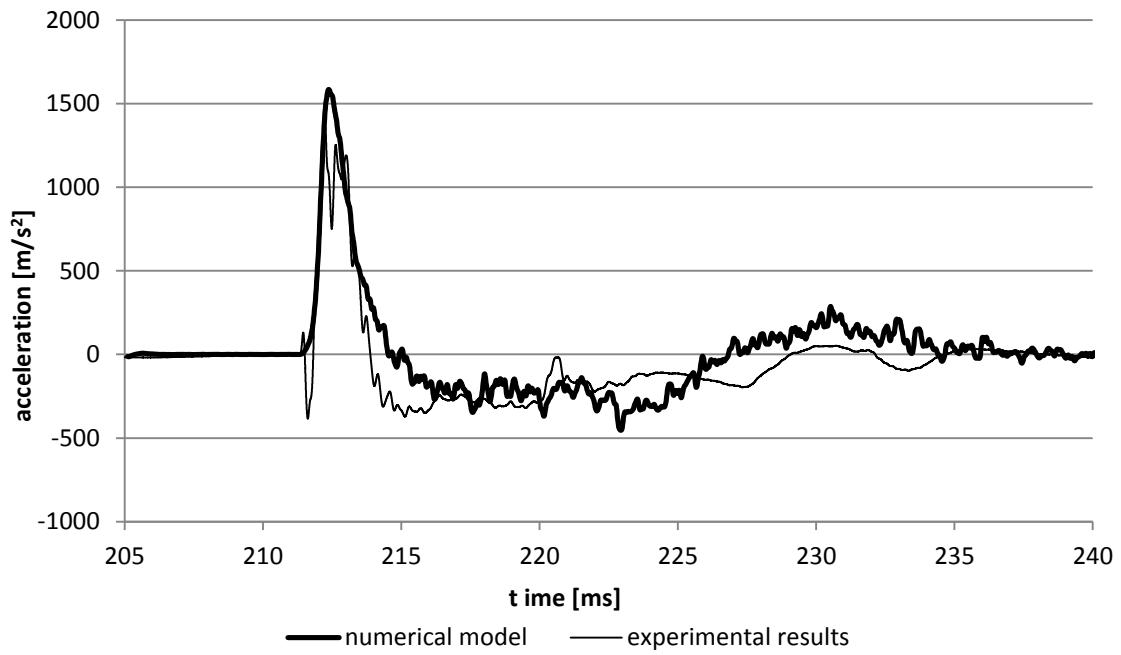
46

3.8.1 Contact section

Figure 3.8.1 Experimental and numerical results of accelerometer A1
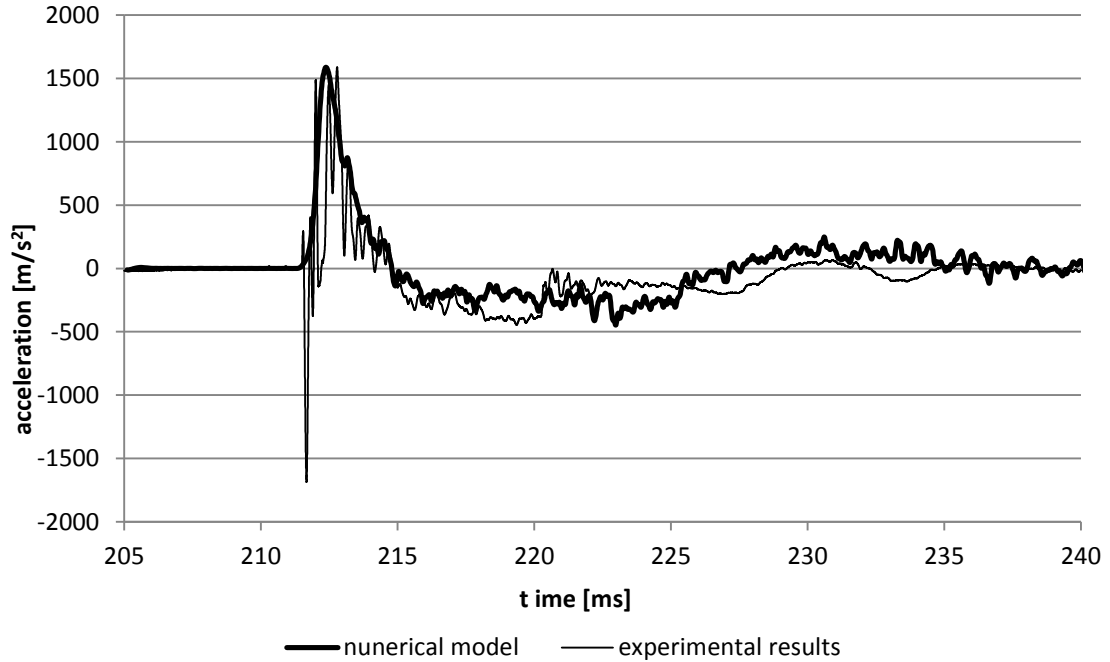

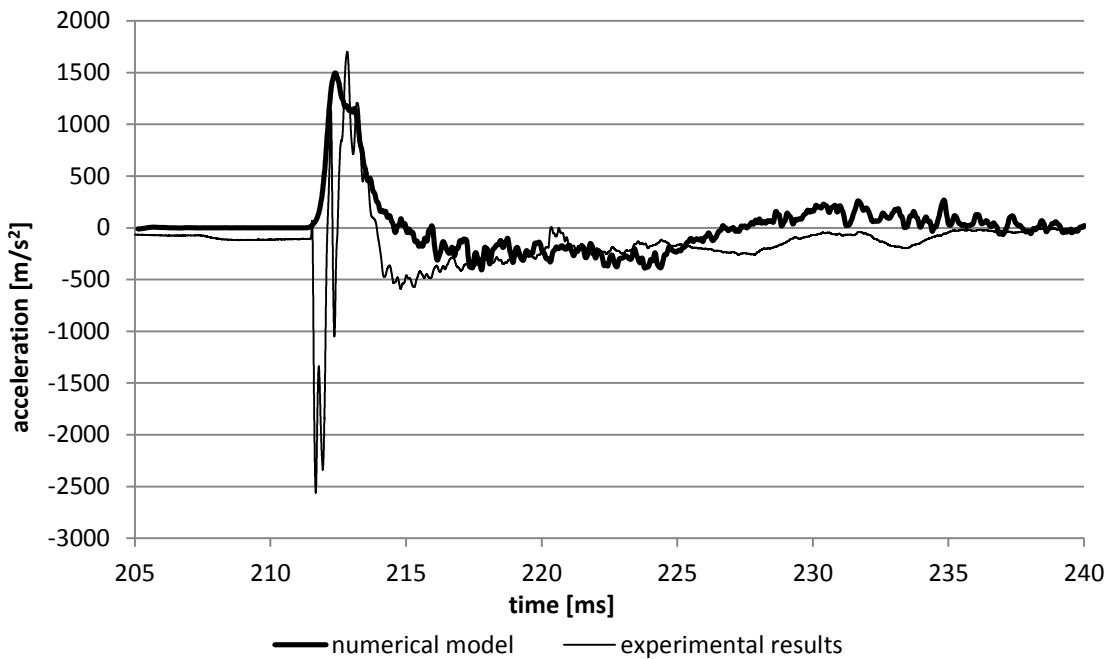Figure 3.8.2 Experimental and numerical results of accelerometer A2

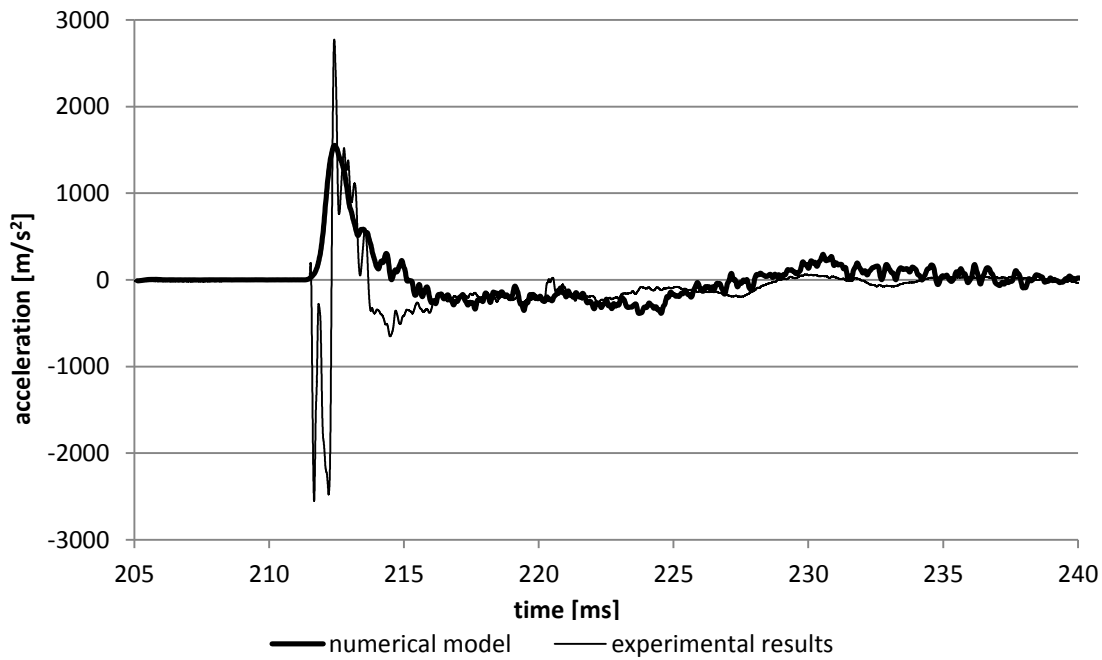Figure 3.8.3 Experimental and numerical results of accelerometer A3

Figure 3.8.4 Experimental and numerical results of accelerometer A4
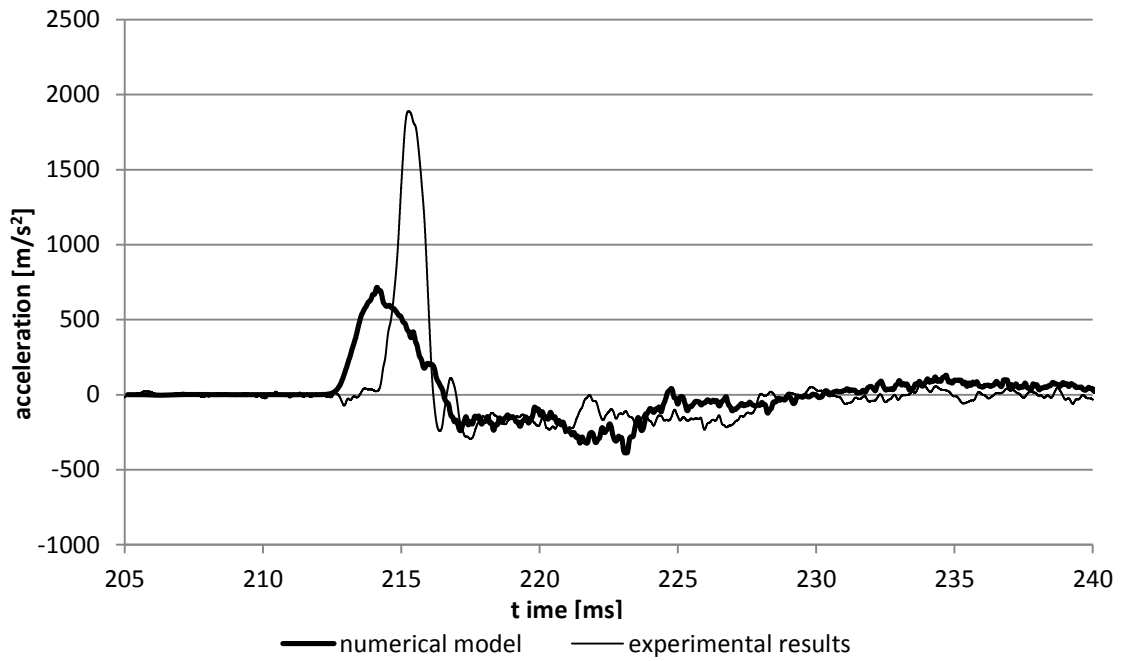
3.8.2 Section A-A

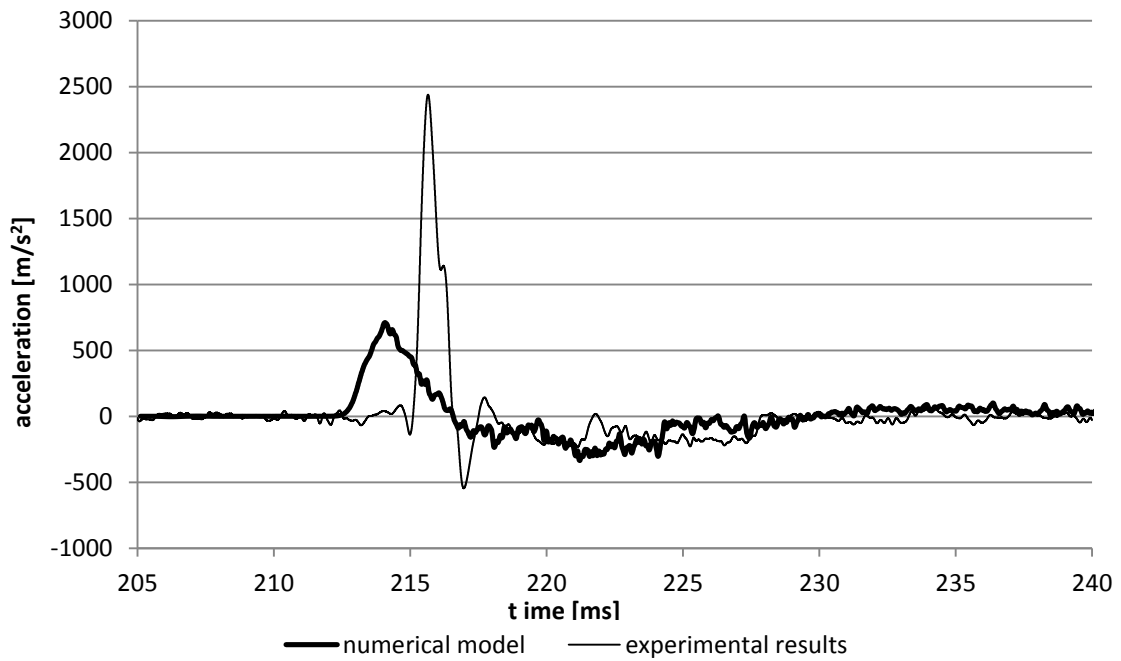Figure 3.8.5 Experimental and numerical results of accelerometer A5

Figure 3.8.6 Experimental and numerical results of accelerometer A7
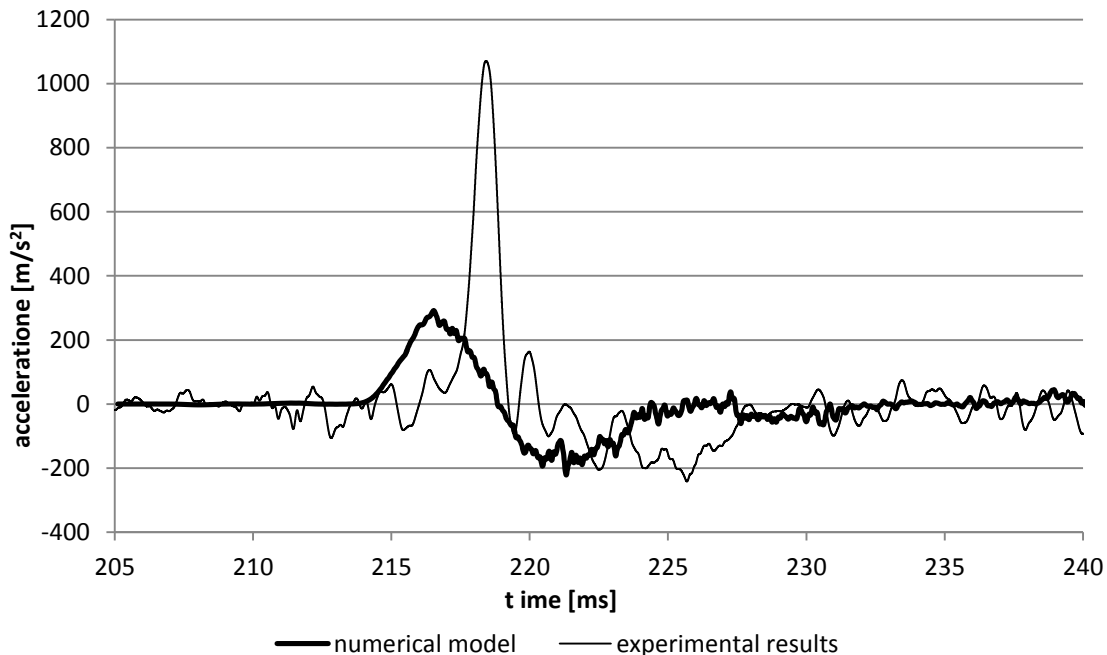
3.8.3 Section B-B

Figure 3.8.7 Experimental and numerical results of accelerometer A9
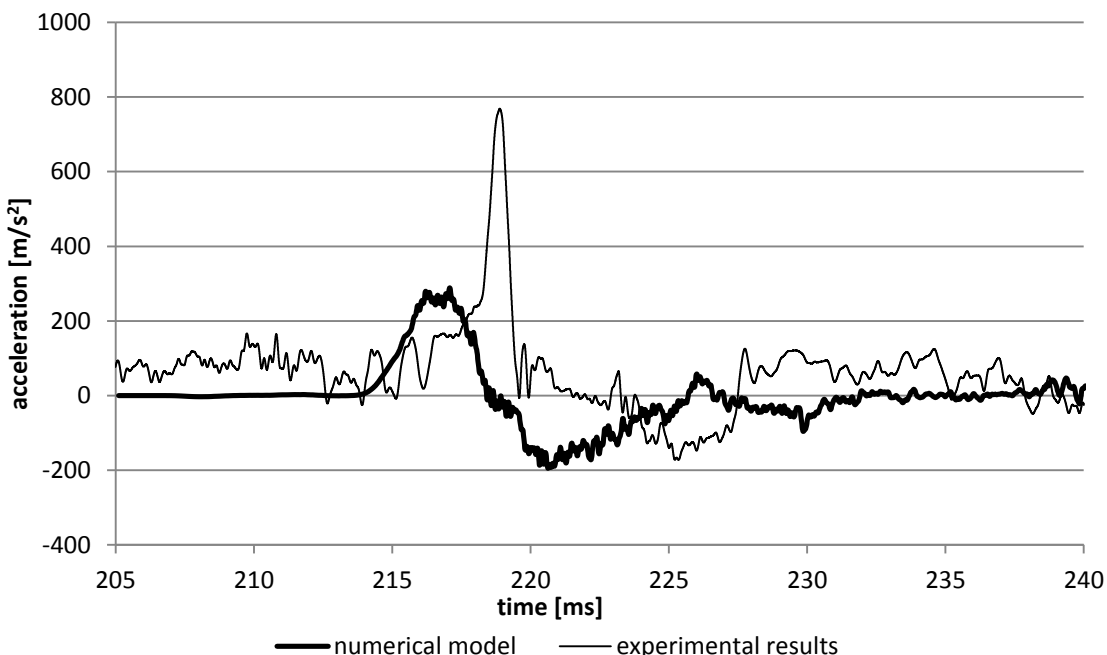

Figure 3.8.8 Experimental and numerical results of accelerometer A11

Chapter 4 Numerical Modeling Using Abaqus – continuous model

In this chapter, the continuous model using Abaqus is created; three feasible models are described in chapter 4.1, and are compared and selected. Then a static load and a dynamic load were applied for model check and analyses in chapter 4.2 and chapter 4.3 respectively.

4.1 Model Description

The numerical calculations have been performed by means of the finite element code ABAQUS, developed by Dassault Systemes Simulia Corp.

4.1.1 Model

Considering the real experiment, a pre-cast specimen resting on soil and rotate into horizontal direction. Then it is hit by a blast wave, characterized by a very sharp time during of the event, an explicit time integration scheme is the most suitable method to optimize the computational efficiency of the numerical simulations. In fact, high-speed dynamic events, such as blast or impact, require many small increments to obtain a good resolution of the solution. The explicit method requires a small time increment size which depends only on the highest natural frequencies of the model and is independent from the type and duration of load. Abaqus/Explicit is a suitable method for analyzing the transient dynamic response of structures interested by blast loads and to take into account the contact interaction within the structure due to the blast. The explicit methods use a central difference rule to integrate the equations of motion explicitly through time, using the kinematic conditions at one increment to calculate the kinematic conditions at the next increment (Abaqus, 2007).

From the experimental results the behavior of the model has been observed to axial-symmetric. For this reason, this characteristic has been adopted into the numerical simulation. So, only an axis-symmetrical slice of the model has been analyzed. It decreases the amount of elements dramatically, and increases the computational speed to a large extent. Here, three simple models are created, and the best one will be picked to do the simulation after comparing the differences among them.

(a) Soil with roller boundary condition (figure 4.1.1)

The length of soil specimen is 1.42m, the radius is 0.2915m.

The shock tube can move forward and backward on a linear guide in order to perform all operations of preparation and subsequent disassembly of the test. Nevertheless, during the test execution, all the equipment remains practically immobile. So, in order to guarantee adequate boundary conditions, the soil and chamber modeled has been stuck at the end.

In the figure 4.1.1, the yellow dash line is the symmetric axis, and the whole blue part is the soil.

At the bottom of soil, the constraint is vertical roller. Consider that the chamber is looked as infinite stiff, the lateral constrain is longitudinal roller. But in this model, it is impossible to simulate the interaction between soil and chamber.

(b) Soil and analytical rigid tube

The dimension of this model is the same with model (a). The bottom boundary condition is the same too. Here, the chamber is added in the model, which is simulated by an analytical rigid element in Abaqus. So in fact, the chamber is still looked as infinite stiff. In the figure 4.1.2, "RP" is the reference point of chamber. In Abaqus every analytical rigid element should has a reference point, which can represent the whole analytical rigid element, since it is a rigid body. The constraint and load acting on the analytical rigid element should just be acted on this reference point. So the constrain of the chamber is a vertical and a longitudinal rollers on the reference point. It is possible obviously to simulate the interaction between soil and chamber.

(c) Soil and tube with real stiffness (figure 4.1.3)

Here, in this model, the dimension of soil is the same. The steel chamber is also an axial-symmetric deformed element. Its thickness is 13.5mm. I set the real material stiffness of the steel chamber. The constraint is only the vertical roller on the bottom of both soil and chamber. It is also possible to simulate the interaction between soil and chamber in this model. However, the dimension of these two parts in the longitudinal direction differs too much, almost 20 times; it will much influence the bandwidth of stiffness matrix, and leads to computational inaccuracy and decreases of computational speed.
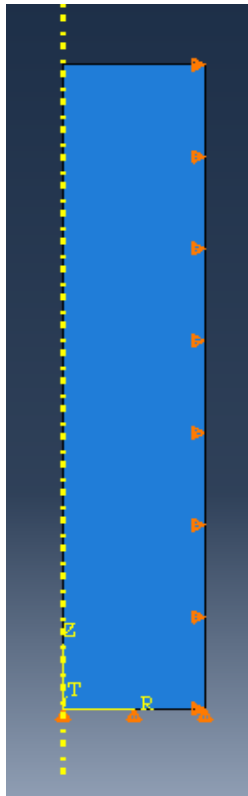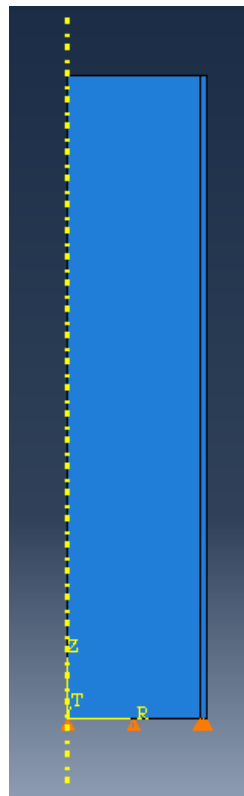

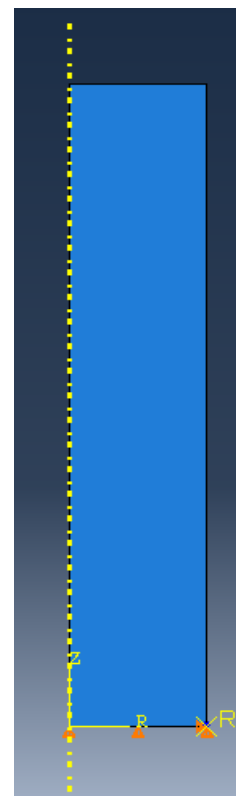Figure 4.1.1 Model a   Figure 4.1.2 Model b   Figure 4.1.3 Model c

4.1.2 Materials

4.1.2.1 Steel Chamber

The small deformations experimentally observed on the tube by means of the strain gauges installed, have shown that the tube has remained in the elastic domain. So, for the steel tube, a linear elastic isotropic constitutive law has been adopted. The mechanical parameters adopted for the steel chamber at room temperature are: Young modulus E=209GPa, Poisson ratio ν=0.3, density ρ=7850 kg/m^3.

4.1.2.2 Soil

Experimentally the soil has shown a residual displacement. This behavior is not reproducible by means of a purely elastic isotropic model. Since the soil used in the experiment is Hostun Sand which density is equal to 1400kg/m^3, I consider elastic model, porous elastic model, Drucker Prager Cap model, and extended Drucher-Prager linear model.

(I) Elastic parameter: Young Modulus equal to 75MPa and Poisson Ratio equal to 0.3.

(II) Porous elastic model (Abaqus 2007): The porous elastic model in Abaqus/Standard ("Elastic behavior of porous materials) is used for porous materials in which the volumetric part of the elastic strain varies with the logarithm of the equivalent pressure stress. This form of nonlinear elasticity is valid for small elastic strains. But it can be used only in Abaqus/Standard.

The elastic part of the volumetric behavior of porous materials is modeled accurately by assuming that the elastic part of the change in volume of the material is proportional to the logarithm of the pressure stress (figure 4.1.4).
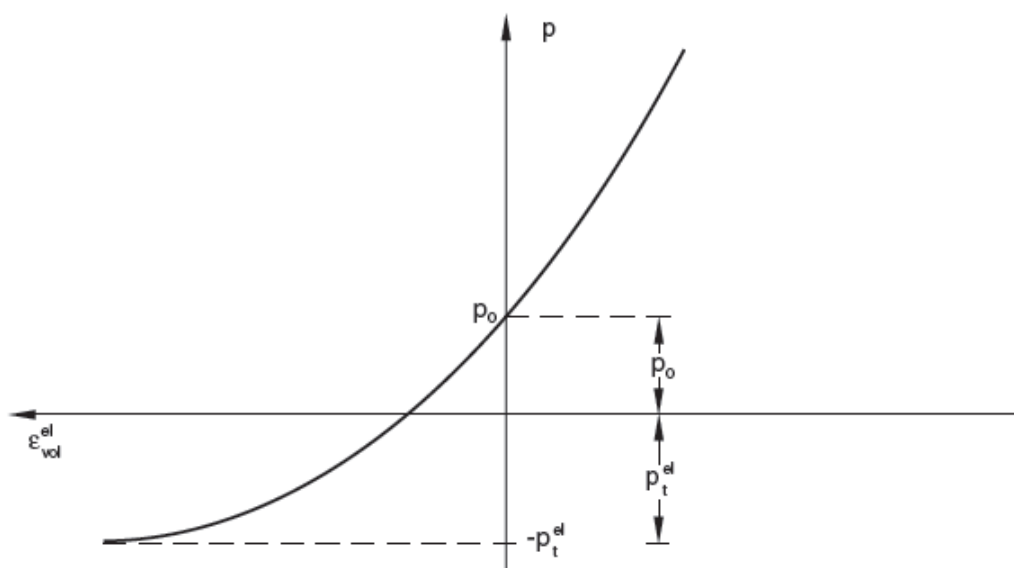

Figure 4.1.4 Porous elastic volumetric behavior (Abaqus 2007)

$$\frac{\kappa}{(1+e_0)}\ln\left(\frac{p_0+p_t^{el}}{p+p_t^{el}}\right) = J^{el} - 1 \qquad\qquad \text{4.1.1 (Abaqus 2007)}$$

Where κ is the "logarithmic bulk modulus"; e_0 is the initial void ratio; p is the equivalent pressure stress, defined by

$$\text{p} = -\frac{1}{3}trace\boldsymbol{\sigma} = -\frac{1}{3}(\sigma_{11} + \sigma_{22} + \sigma_{33}) \qquad\qquad \text{4.1.2 (Abaqus 2007)}$$

p_0 is the initial value of the equivalent pressure stress; J^{el} is the elastic part of the volume ratio between the current and reference configurations; and p_t^{el} is the "elastic tensile strength" of the material (in the sense that $J^{el} \to \infty$ as $\text{p} \to -p_t^{el}$).

The instantaneous shear modulus is defined from the instantaneous bulk modulus and Poisson's ratio, ν, as follow:

$$\text{G} = \frac{3(1-2\nu)(1+e_0)}{2(1+\nu)\kappa}(p + p_t^{el})\exp(\varepsilon_{vol}^{el}) \qquad\qquad \text{4.1.3 (Abaqus 2007)}$$

Where $\varepsilon_{vol}^{el} = \ln J^{el}$ is the logarithmic measure of the elastic volume change. In this case

$$\text{dS} = 2Gde^{el} \qquad\qquad \text{4.1.4 (Abaqus 2007)}$$

Thus, the elastic shear stiffness increase as the material is compacted. This equation is integrated to give the total stress-total elastic strain relationship.

(III) Drucker Prager Cap model: the elastic response is governed by the same parameters previously, while the inelastic part is defined by a shear failure surface and a cap yield surface characterized by a cohesion value equal to 1.1E-6 (this value in Abaqus is starting from 1E-6), a friction angle equal to 42°, an initial yield position equal to zero (the material starts from a virgin condition) and a flow stress ratio equal to 1. So, in the principal deviate stress plane, the Drucker Prager surface coincides with the Von Mises circle. Other two parameters are necessary to define the geometry of the cap. These parameters are the cap eccentricity (R), sets equal to 1, and the transition surface ratio (α), sets equal to 0.01.
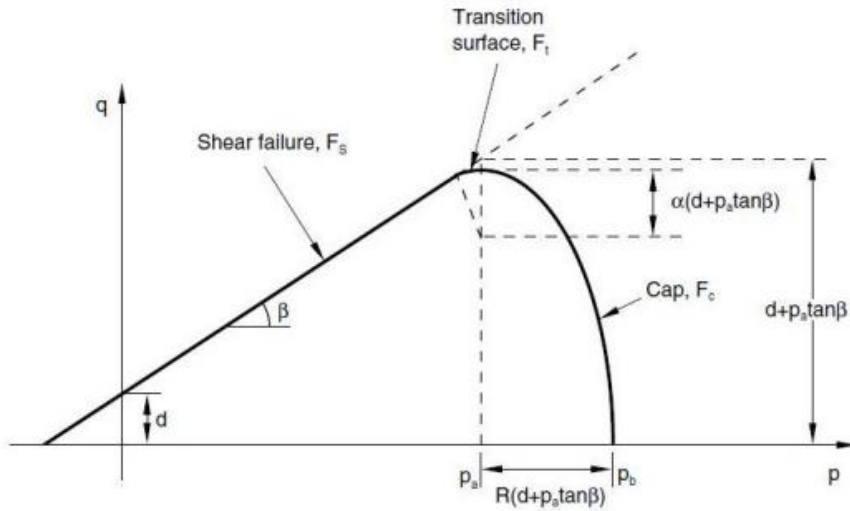

Figure 4.1.5 Drucker-Prager cap model: yield surface in the q-p plane (Abaqus 2007)

The cap evolution is defined by a hardening law that is a piecewise linear function which relates the hydrostatic compression yield stress with the corresponding plastic strain deformation. The available data, found in literature, is an experimental isotropic triaxial test conducted pressurizing the virgin sample equally in all directions, and recording the pressure and the volume change.

This test has been performed on a Hostun sand sample with a density of 1620kg/m^3 and a relative density 100% (Di Prisco, 1993), the sand used in the shock tube experimental tests, is characterized by a mean density of 1400kg/m^3 and a relative density of about 30%. The data are summarized in following table. Unfortunately, the available data start from a mean pressure of 0.5MPa. So in order to obtain pressure value starting nearest zero, as in the experiments, the real data have been interpolated and shifted. The interpolating function adopted is:

$$P' = 0.5e^{103.86\varepsilon_v}$$ 4.1.5

The data I use is from this interpolating function shifted of 3%.

Table 4.1.1 Experimental isotropic triaxial test data (Di Prisco 1993)

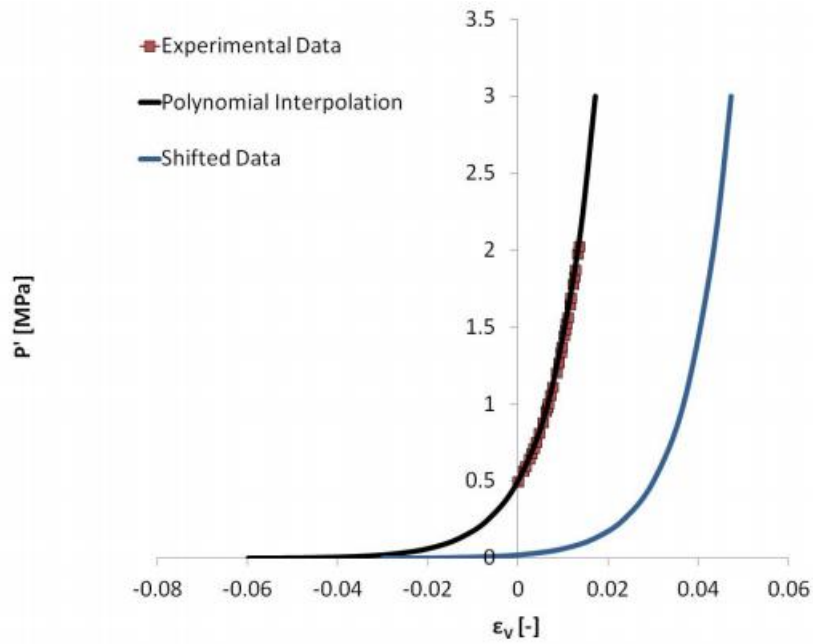| P'[MPa]	ε_v
0.5	0
0.54695	0.000075
0.54795	0.00125
0.57695	0.00175
0.59545	0.0025
0.62495	0.003
0.65395	0.004
0.70195	0.00475
0.72045	0.0055
0.73945	0.00625
0.77895	0.0065
0.81895	0.00675
0.84795	0.00725
0.87695	0.00775
0.89545	0.0085
0.92495	0.009
0.95395	0.0095
0.99395	0.00975
1.02295	0.01025
1.06245	0.0105
1.10195	0.01075
1.14145	0.011
1.16895	0.0115

Figure 4.1.6 Isotropic experimental triaxial test data;
polynomial interpolation function and shifted data (Corti L., Corti L.G., 2012)

(IV) extended Drucker-Prager linear model (Abaqus 2007):

The linear model provides for a possibly noncircular yield surface in the deviatoric plane to match different yield values in triaxial tension and compression, associated inelastic flow in the deviatoric plane, and separate dilation and friction angles.
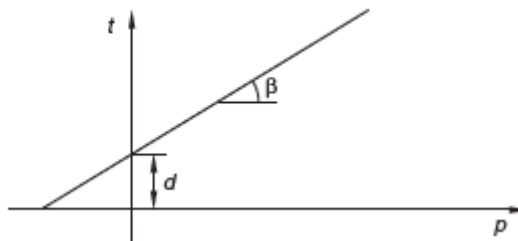

Figure 4.1.7 Linear Drucker-Prager yield surface in the meridional plane (Abaqus 2007)

The linear Drucker-Prager criterion is written as:

$$F = t - p\tan\beta - d = 0 \qquad\qquad 4.1.6 \text{ (Abaqus 2007)}$$

4.1.3 Interaction between soil and chamber

Regarding the interaction properties, a contact pair interaction has been selected in order to define the interactions between soil and chamber. The following properties are necessary to define the interactions:

- The contact pair algorithm;
- The surfaces that interact one each other;
- The contact surface properties.

As contact pair algorithm, the surface-to-surface contact (explicit), with the penalty constraint

enforcement method, has been selected. In the contact formulation, a finite sliding formulation, which takes into account the relative motion (arbitrary separation and sliding) of two surfaces forming a contact pair, has been selected. For the soil-chamber interaction surface, the tangential and the normal behavior have been defined.

For the normal behavior a hard contact model has been adopted. This contact implies that the surface transmit no contact pressure unless the nodes of the slave surface (the surface that belong to the more deformable material) contact the master surface (the surface that belong to the more rigid material), (The analytical rigid surface must be set to be master surface.); no penetration is allowed at each con constraint location and the surfaces could separate themselves if the contact pressure reduces to zero.

Instead, for the tangential behavior a penalty friction formulation has been used. This is the classical isotropic Coulomb friction model which relates the maximum allowable friction (shear) stress, across an interface, to the contact pressure between the contacting bodies. In the basic form of the Coulomb friction model, two contacting surfaces can carry shear stress up to a certain magnitude across their interface before they start sliding relative to one another; this state is known as sticking. More complex models have not been adopted due to the lack of data.

$$\tau_{critical} = \mu P \qquad\qquad\qquad 4.1.7 \text{ (Abaqus 2007)}$$

The stick/slip calculation determines when a point transitions from sticking to slipping or from slipping to sticking. Actually this is the static friction coefficient; nevertheless, the coefficient adopted is the dynamic one. In fact, the impulsive phenomenon causes a very rapid transition from the static coefficient to the dynamic one. The friction coefficient adopted is equal to 0.4. this is not the true value but a reasonable one. A more detailed discussion about this value will be shown in the later chapter.
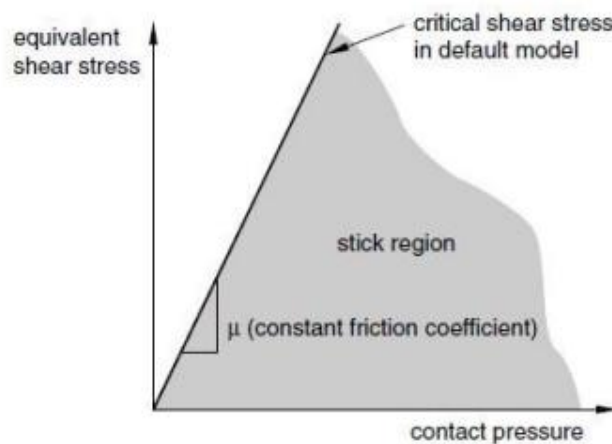

Figure 4.1.8 Stick Region for the Basic Coulomb Friction Model (Abaqus 2007)

4.1.4 Step and load

For what concerns the load, a basic concept in Abaqus is the division of the problem history into steps. A step is any convenient phase of load history. In the experiment test, the procedures before the impact load are complex, which are necessary to well-prepare the soil specimen to be longitudinal and to be a right stress state. Then, in the numerical model, I divided into two step: the first one is the vertical gravity loading. It relate to the procedure in the experiment when the

chamber is vertical; the second step is loading the vertical pressure (since the model is veritical) on the soil surface, which related to the impact load in the experiment when the chamber is longitudinal after rotation.

- Step1: vertical gravity
- Step2: loading

Table 4.1.2 The loads used in step 2

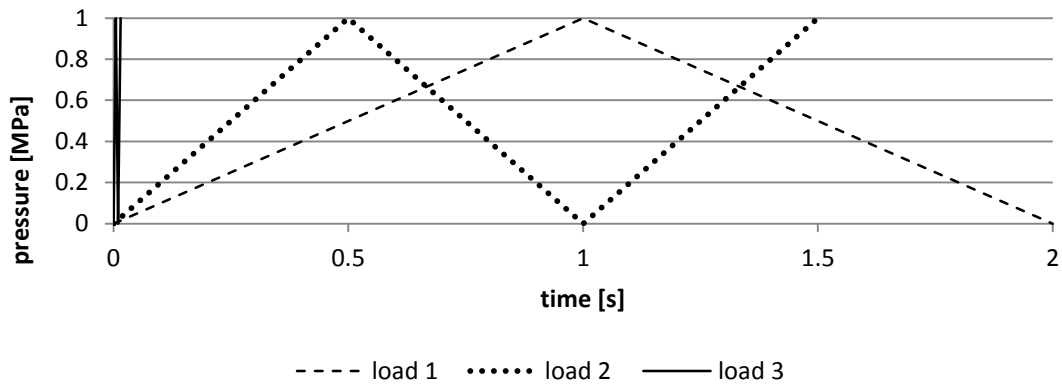| load 1	static	time[s]	0	1	2		Used in C4.1.5
		magnitude[MPa]	0	1	0		
load 2	static	time[s]	0	0.5	1	1.5	Used in C4.2
		magnitude[MPa]	0	1	0	1	
load 3	dynamic	time[s]	0	0.005	0.01	0.015	Used in C4.3
		magnitude[MPa]	0	1	0	1	

Figure 4.1.9 The loads used in step 2

4.1.5 Comparisons of the three models considered

According to the previous description, I consider three possible models which have their advantages and disadvantages. By comparisons of two loading step, I want to pick the best one as numerical model used in simulation of experiment. The soil is considered only with elastic constitutive model. Six points (figure 4.1.10) on the soil are picked for analysis. Points A1, B1, C1 are on the symmetric axis, while Points A2, B2, C2 are on the interaction surface.

To model the soil, CAX4R elements (4-node bilinear axisymmetric quadrilateral, reduced integration, hourglass control) have been adopted. The total number of soil elements used is 4118, with a smallest size of $10mm \times 10mm$. For accurate analysis, a fine mesh is necessary. In fact, for reducing the artificial energy (AE), which is the accumulated energy used to control the hourglass deformation, it is necessary to refine the mesh. Refine the mesh is also useful to avoid the penetration between two surfaces that belong to two different parts. So, the element mesh dimensions have been evaluated in order to satisfy these requirements.
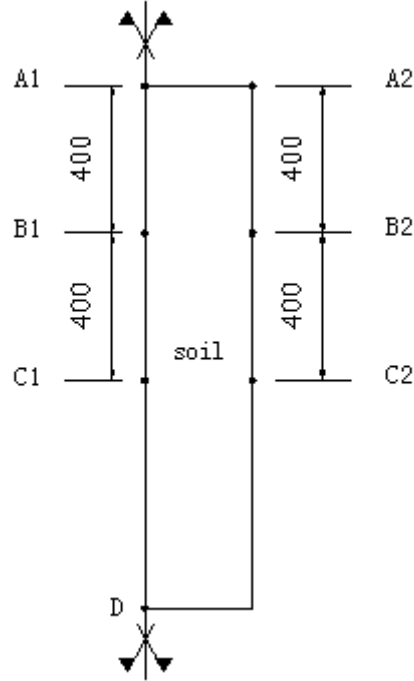
Figure 4.1.10 The positions of points

(I) step 1

Under the gravity, without frictional interaction between soil and chamber, the analytical solutions of the vertical displacement at top center (point A1) and the vertical stress at bottom center (point D) are as follow:

Point D:

$$\sigma_v^D = \rho g l = \frac{9.81\text{m}}{s^2} \times \frac{1400\text{kg}}{m^3} \times 1.42m = 1.9502 \times 10^4 Pa$$

$$\frac{\sigma_h^D}{\sigma_v^D} = \frac{\nu}{1-\nu} = \frac{0.3}{1-0.3} = 0.4286$$

Point A1:

$$\varepsilon_h^{A1} = -\nu \frac{\sigma_v^{A1}}{E} + (1-\nu)\frac{\sigma_h^{A1}}{E} = 0 \ \Rightarrow\ \sigma_h^{A1} = \frac{\nu}{1-\nu}\sigma_v^{A1}$$

$$\varepsilon_v^{A1} = \frac{\sigma_v^{A1}}{E} - 2\nu\frac{\sigma_h^{A1}}{E} = \frac{\sigma_v^{A1}}{E}\left(1 - \frac{2\nu^2}{1-\nu}\right) = \frac{1}{E}\frac{1-\nu-2\nu^2}{1-\nu}\sigma_v^{A1}$$

$$s_v^{A1} = \int_0^l \varepsilon_v^{A1}\, dz = \frac{1}{E}\frac{1-\nu-\nu^2}{1-\nu}\int_0^l \rho g l\, dz = \frac{1}{2}l^2 \times \frac{\rho g}{E} \times \frac{1-\nu-\nu^2}{1-\nu} \ \Rightarrow$$

$$s_v^{A1} = \frac{1}{2} \times 1.42^2 \times \frac{9.81 \times 1400}{75 \times 10^6} \times \frac{1-0.3-2\times(0.3)^2}{1-0.3} = 1.3715 \times 10^{-4}m$$

The numerical results of model a, b and c are shown in table 4.1.3.

Table 4.1.3 The comparisons of strain and stress among three models

	analytical	units	model a	relative error	model b	relative error	model c	relative error
σ_v^D	1.950E+04	Pa	1.943E+04	0.37%	1.944E+04	0.32%	1.944E+04	0.32%
σ_h^D/σ_v^D	0.4286	-	0.4286	0.00%	0.4247	0.90%	0.4202	1.97%
s_v^{A1}	1.372E-04	m	1.371E-04	0.04%	1.376E-04	0.33%	1.381E-04	0.69%

From the numerical results, in this step they are almost the same, the differences of each model compared to analytical solution are reasonable and negligible small.

(II) Step 2

Under load 1, a static and simply load, without friction between soil and chamber, the vertical displacements of Point A1 computed using different models are as follow table 4.1.4. Since friction is not considered here, the point on the interface will have the same behavior as the point on the symmetric axis.

Table 4.1.4 Displacements of Point A1 of tree models

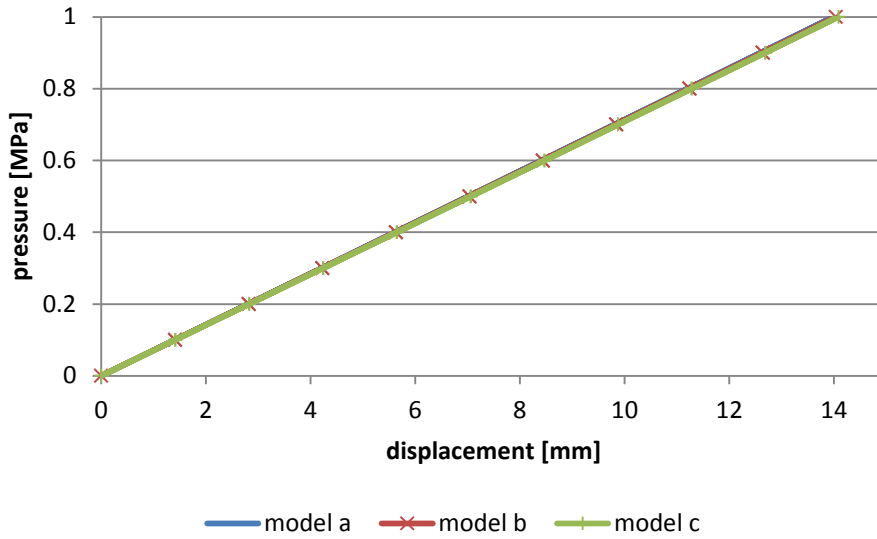| time [s]	Load pressure [MPa]	displacement of Point A1 [mm]		
		model a	model b	model c
0	0	0.00	0.00	0.00
0.1	0.1	1.41	1.41	1.42
0.2	0.2	2.81	2.82	2.83
0.3	0.3	4.21	4.23	4.24
0.4	0.4	5.61	5.63	5.65
0.5	0.5	7.01	7.04	7.06
0.6	0.6	8.41	8.44	8.47
0.7	0.7	9.81	9.84	9.88
0.8	0.8	11.21	11.24	11.28
0.9	0.9	12.60	12.64	12.69
1	1	13.99	14.04	14.09
1.1	0.9	12.60	12.64	12.69
1.2	0.8	11.21	11.24	11.28
1.3	0.7	9.81	9.84	9.88
1.4	0.6	8.41	8.44	8.47
1.5	0.5	7.01	7.04	7.06
1.6	0.4	5.61	5.63	5.65
1.7	0.3	4.21	4.23	4.24
1.8	0.2	2.81	2.82	2.83
1.9	0.1	1.41	1.41	1.42
2	0	0.00	0.00	0.00

Figure 4.1.11 P-s cureve of Point A1

Consider friction coefficient 0.4, the displacements of A1 and A2 are as follow table 4.1.5:

Table 4.1.5 The displacements of Point A1 and A2 of model b and c

time [s]	pressure [MPa]	displacement of A1 [mm]		displacement of A2 [mm]	
		model b	model c	model b	model c
0	0	0	0	0	0
0.1	0.1	0.74	0.74	0.66	0.67
0.2	0.2	1.47	1.49	1.33	1.34
0.3	0.3	2.21	2.24	1.99	2.02
0.4	0.4	2.95	2.98	2.66	2.69
0.5	0.5	3.68	3.73	3.32	3.36
0.6	0.6	4.42	4.48	3.98	4.04
0.7	0.7	5.16	5.22	4.65	4.71
0.8	0.8	5.90	5.97	5.31	5.39
0.9	0.9	6.63	6.72	5.98	6.06
1	1	7.37	7.46	6.64	6.73
1.1	0.9	7.03	7.12	6.58	6.67
1.2	0.8	6.69	6.77	6.55	6.63
1.3	0.7	6.35	6.42	6.51	6.58
1.4	0.6	6.00	6.07	6.41	6.48
1.5	0.5	5.64	5.70	6.19	6.25
1.6	0.4	5.24	5.29	5.80	5.85
1.7	0.3	4.72	4.76	5.20	5.23
1.8	0.2	3.97	4.00	4.31	4.34
1.9	0.1	2.76	2.77	2.93	2.94
2	0	0.17	0.17	0.18	0.17
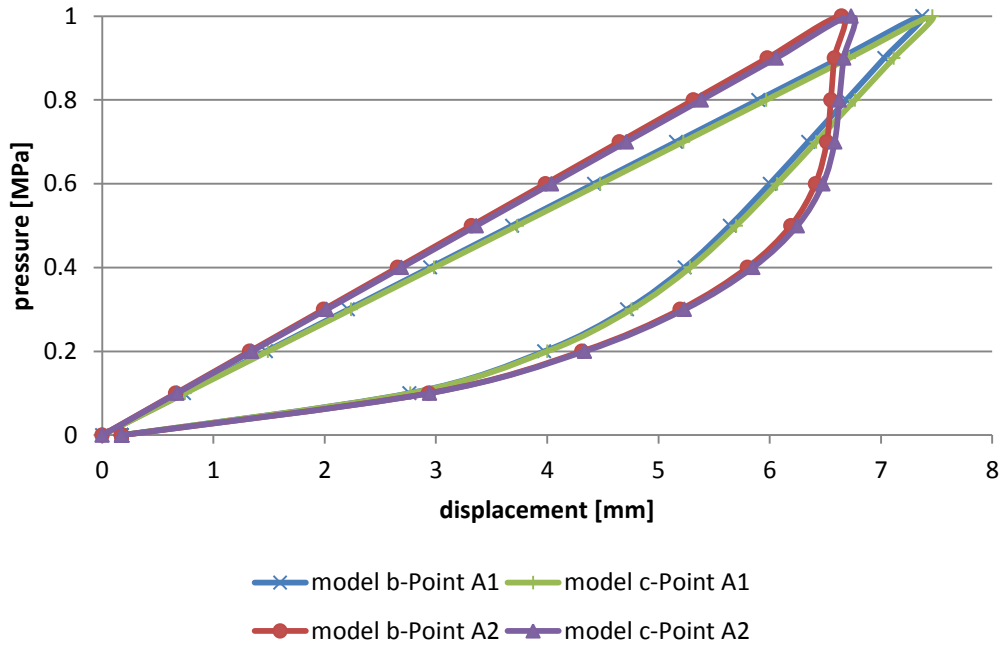
Figure 4.1.12 P-s curve of Point A1 and A2

It is obviously that the results from model a, b and c are almost same, no matter whether the friction is considered or not. As expected, the friction will influence the behavior of the point on the interface. So, in order to be simplest, most efficient and sufficient, **model b (Soil with analytical rigid tube)** is selected.

4.1.6 Comparison with the result of PFC3D

The static load 1 is loaded on the model of PFC3D described in the chapter 3.7, with different friction coefficient 0.2, 0.4 and 0.6. The pressure-displacement curves on Point A1 of the PFC model and ABAQUS model are shown in figure 4.1.13.
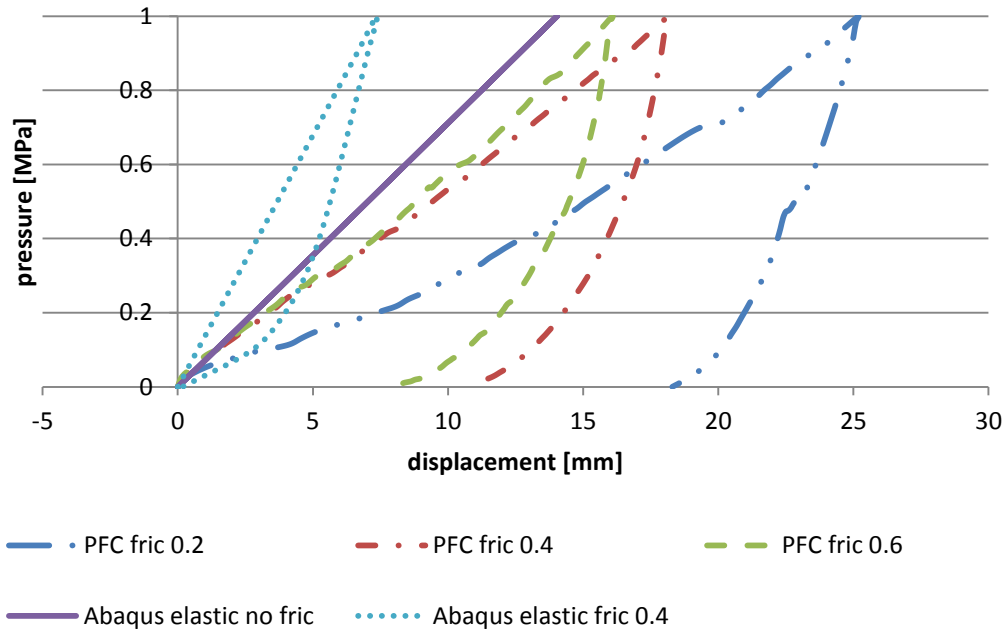
Figure 4.1.13 P-s curves on Point A1 of both models using PFC and ABAQUS

Point A1 is at the center of loading cross section. The displacement calculated by PFC is uniform on the loading section, on which every points have same displacements. By comparison, the results of PFC are much bigger than that of Abuqus both of the peak displacement and residual displacement. The difference of peak displacement is larger than 10mm (Abaqus elastic friction 0.4 and PFC friction 0.4). Because the material properties used in Abuqus are elastic. While the model of PFC is consist of discrete particles, where the balls are rigid and there're voids between balls. The displacement of PFC model comes from the decrease of void ratio rather than the deformation of material. So it will have larger peak and residual displacements and show more unrecoverable and plastic behavior.

4.2 Model check under static load

For the analysis in this part, load 2 which has loading phase, unloading phase and reloading phase is used.

4.2.1 Friction sensitivity

Figure 4.2.1 – Figure 4.2.4 show the results of pressure-displacement curve with different friction coefficients at each Point (Point A1, B1, C1 are at the center of section, A2, B2, C2 are on the interface, Figure 4.1.10). In order to divide the source of non-elastic dissipation which can come from both the material and the friction, the material used in the part is only elastic.
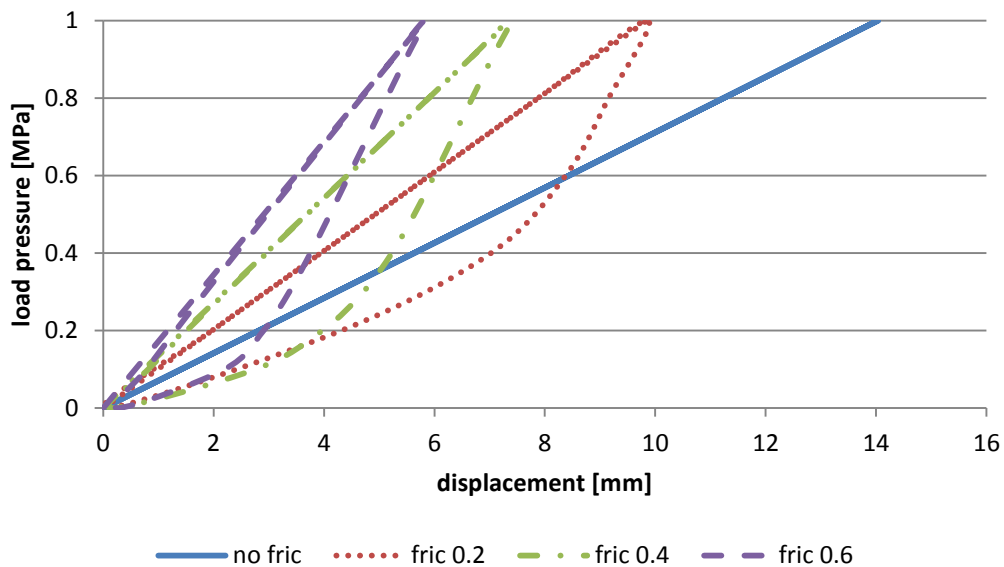
Figure 4.2.1 P-s curve of Point A1 with different friction
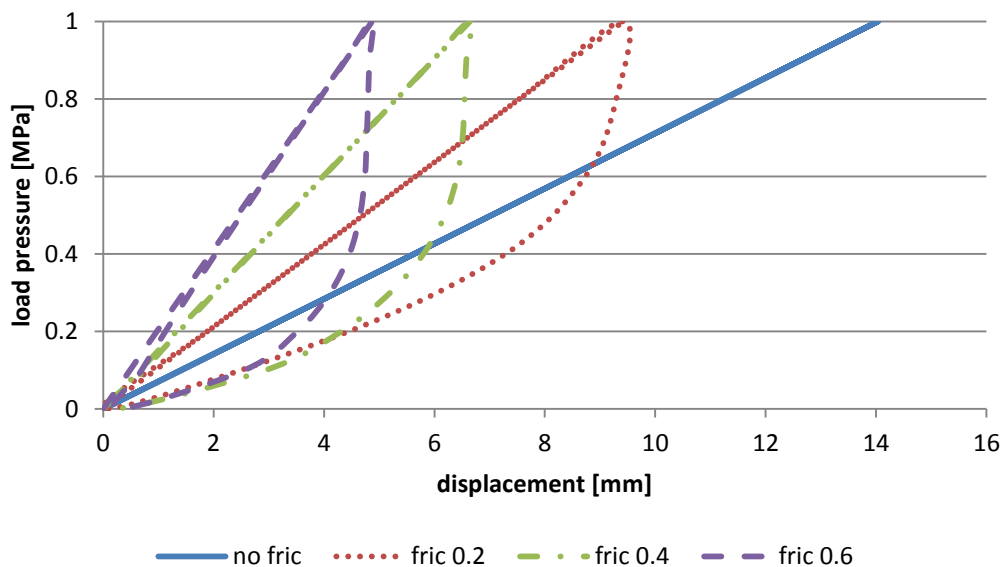
Figure 4.2.2 P-s curve of Point A2 with different friction

As the theoretical analyses, the maximum displacement decreases with friction coefficient increasing. In the loading phase, the pressure-displacement behavior is linear, which corresponds to the elastic material behavior. In the unloading phase, it shows the non-linear behavior caused by the friction. And the bigger the friction coefficient is, the more obvious the non-linear behavior is shown. This is shown both on the center point and the interface point.
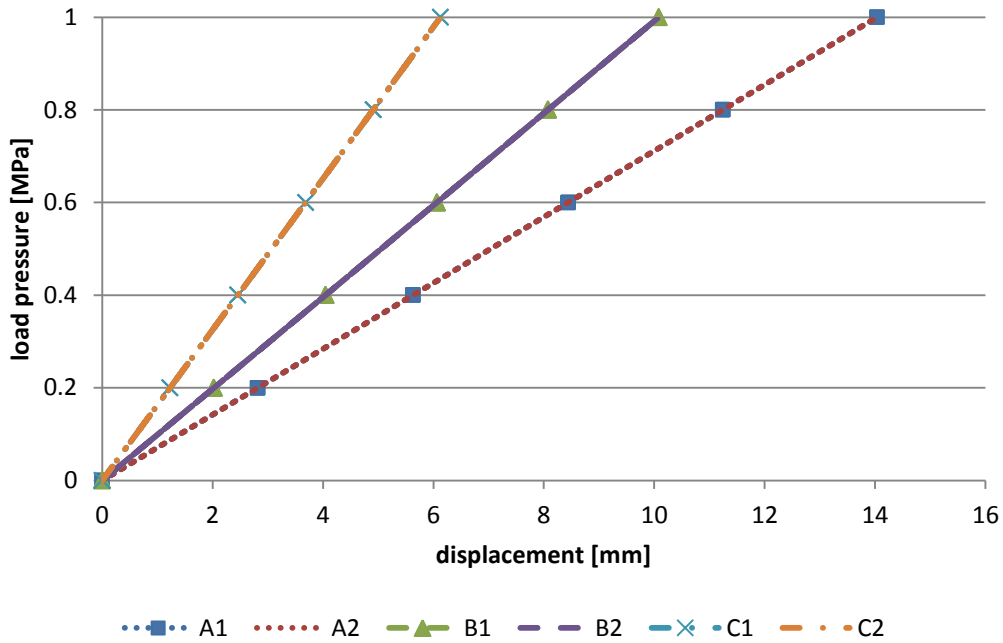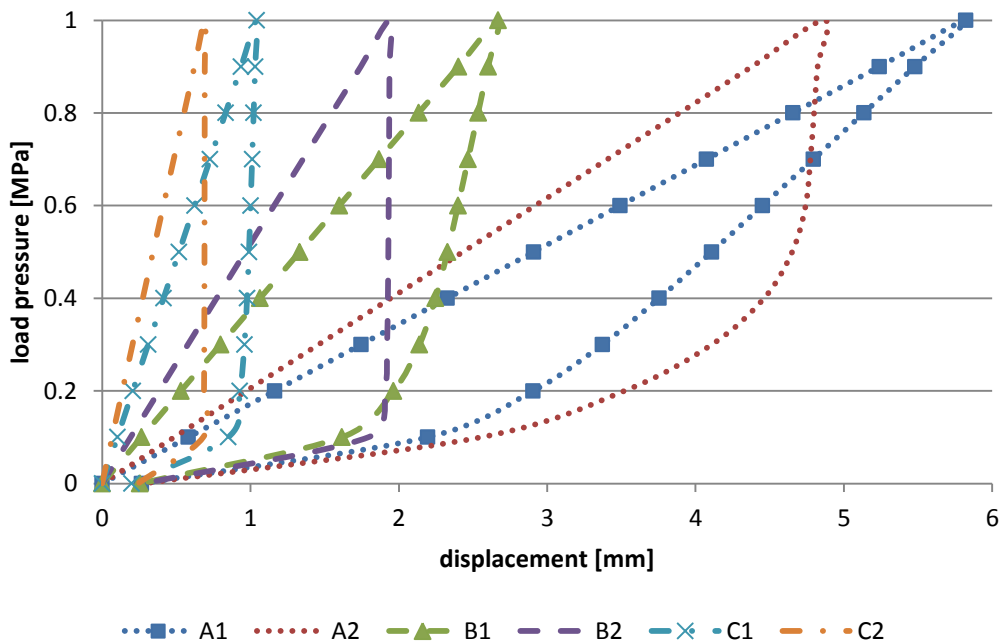

Figure 4.2.3 P-s curves without friction

Figure 4.2.4 P-s curves with friction coefficient 0.6

From figure 4.2.3 and 4.2.4, the previous discussion can also be proofed. At the same time, it also shows that the position of point is another factor. As the depth of point gets larger, the maximum

displacement decreases, in other words, the influence of loading decreases. On the other hand, the point on the interface which is at the same cross section with the corresponding center point, shows much more non-linear behavior than the center point, except in the case without friction. And also, this difference gets larger with larger friction coefficient.

Table 4.2.1 and table 4.2.2 list the data of maximum displacement after loading.

Table 4.2.1 Maximum displacement after loading [mm]

	no friction	friction 0.2	friction 0.4	friction 0.6
A1	14.1749	9.853485	7.370876	5.821513
A2	14.03735	9.423611	6.640143	4.867239
B1	10.08284	6.2472895	4.021886	2.668262
B2	10.08286	5.9005829	3.446275	1.938078
C1	6.128625	3.3885118	1.89007	1.041522
C2	6.128626	3.1170239	1.534666	0.691905

The influence of point positions is almost the same from the point of view of residual displacement. As the position of point goes deeper, the material behavior is stiffer, the residual displacement decreases. And with bigger friction the residual displacement increases both on the center points and interface points. Compared with the results on these two kinds of points, the ones on the interface points is larger than that on the center points. And the bigger the friction coefficient is, the bigger this difference is.

Table 4.2.2 Residual displacement after unloading [mm]

	NO FRIC	FRIC 0.2	FRIC 0.4	FRIC 0.6
A1	0.0000	0.0658	0.1646	0.2643
A2	0.0000	0.0692	0.1724	0.2756
B1	0.0000	0.0648	0.1596	0.2542
B2	0.0000	0.0657	0.1724	0.2746
C1	0.0000	0.0535	0.1297	0.1984
C2	0.0000	0.0646	0.1532	0.2411

4.2.2 Constitutive model

In this part, the influence of material constitutive model without friction is considered, which is another source of non-linear behavior. In this case there is no difference between center point and interface point which are on the same cross section.

Figure 4.2.5 shows the pressure-displacement relationships of different material properties on Point A1. It is obvious that the results of elastic model and Drucker-Prager linear model are almost the same. While Drucker-Prager cap model and porous elastic model behave in much different ways which are all non-linear. The p-s relationship of Drucker-Prager cap model has big maximum displacement and residual displacement. Furthermore it goes in rather different paths in loading and unloading. While the p-s relationship of porous elastic model has the biggest

deformation among that of these four models. However the loading-unloading path is the same. Table 4.2.3 and table 4.2.4 list the data of maximum displacement and residual displacement on each point respectively.
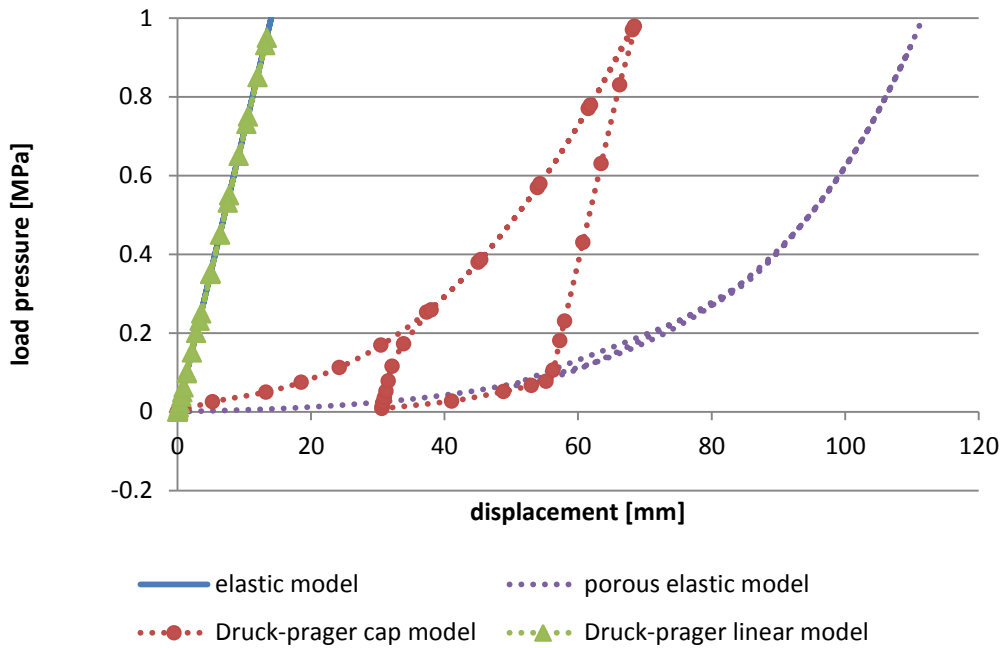

Figure 4.2.5 P-s curve of Point A1 of different models

Table 4.2.3 Residual displacement after unloading without friction [mm]

	points on the center of cross section			points on the interactive face		
	A1	B1	C1	A2	B2	C2
elastic	7E-06	3E-06	1.2E-06	7E-06	3E-06	9E-07
porous elastic	51.2549	31.7772	17.5023	51.255	31.7771	17.5023
Drucker-Prager cap	30.60306	23.65655	15.1849552	30.57138	23.65247	15.18398
Drucker-Prager linear	14.12612	10.13724	6.1623749	14.10995	10.13806	6.162316

Table 4.2.4 Maximum displacement after loading without friction [mm]

	points on the center of cross section			points on the interactive face		
	A1	B1	C1	A2	B2	C2
elastic	14.03732	10.08284	6.1286249	14.03735	10.08286	6.128626
porous elastic	111.6217	74.6267	43.2508	111.6217	74.6267	43.2508
Drucker-Prager cap	69.07516	49.55505	30.1401552	68.91388	49.55697	30.14168
Drucker-Prager linear	14.12612	10.13724	6.1623749	14.10995	10.13806	6.162316

Because of no friction, the results of center points and interface points are the same. However the influence of depth is still larger.

4.3 Model check under dynamic load

For the analysis in this part, the dynamic load 3 (Table 4.1.2.) is used.

4.3.1 Friction sensitivity

The material used in this part is only elastic.

Displacement

From figure 4.3.1 and 4.3.2, it can be seen that the elastic results without friction have perfect accordance to the theoretical analyses. The lager friction leads to smaller oscillation. Especially on the interface point (A2), there's nearly no oscillation when it has friction. At the same time, the friction also leads to decrease of displacements.
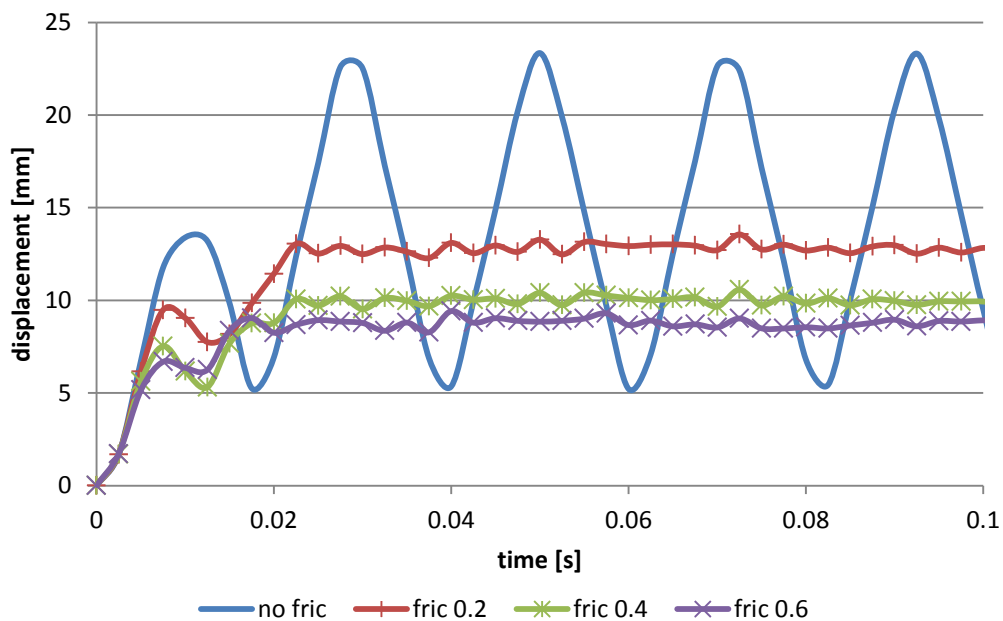
Figure 4.3.1 S-t curves of Point A1 with different friction coefficients
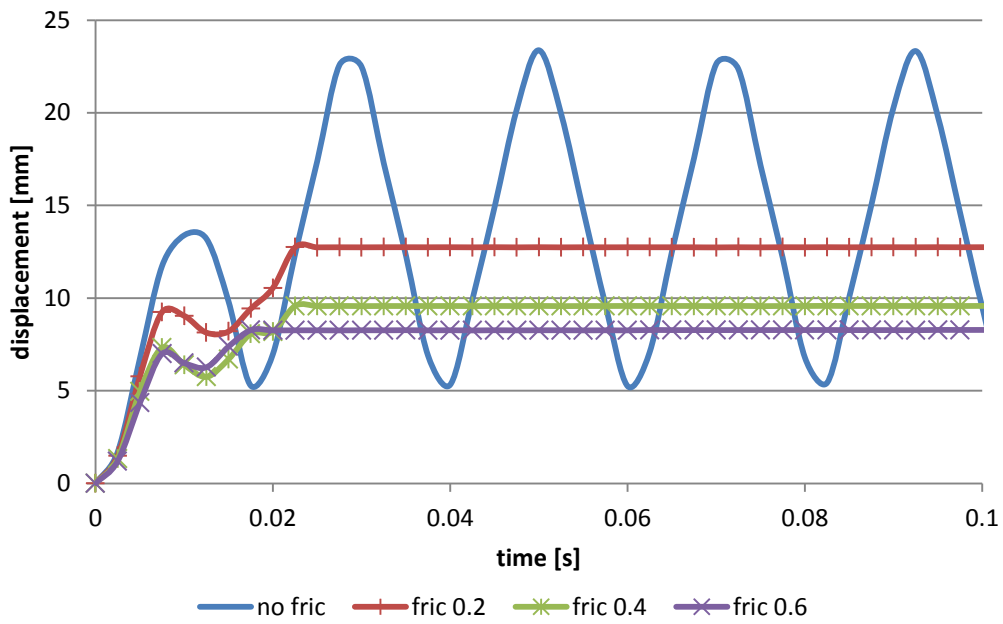
Figure 4.3.2 S-t curves of Point A2 with different friction coefficients

As brief summarizing previously, the position of point is also a factor. The points on the deeper section have fewer displacements no matter the first peak or the following oscillation on both center points and interface points. However there's still a little difference of the results between these two kinds of points on the same section. The friction causes less or nearly no oscillation on interface points. And the larger friction coefficient leads to larger differences. These are drawn from Figure 4.3.3 – Figure 4.3.6.
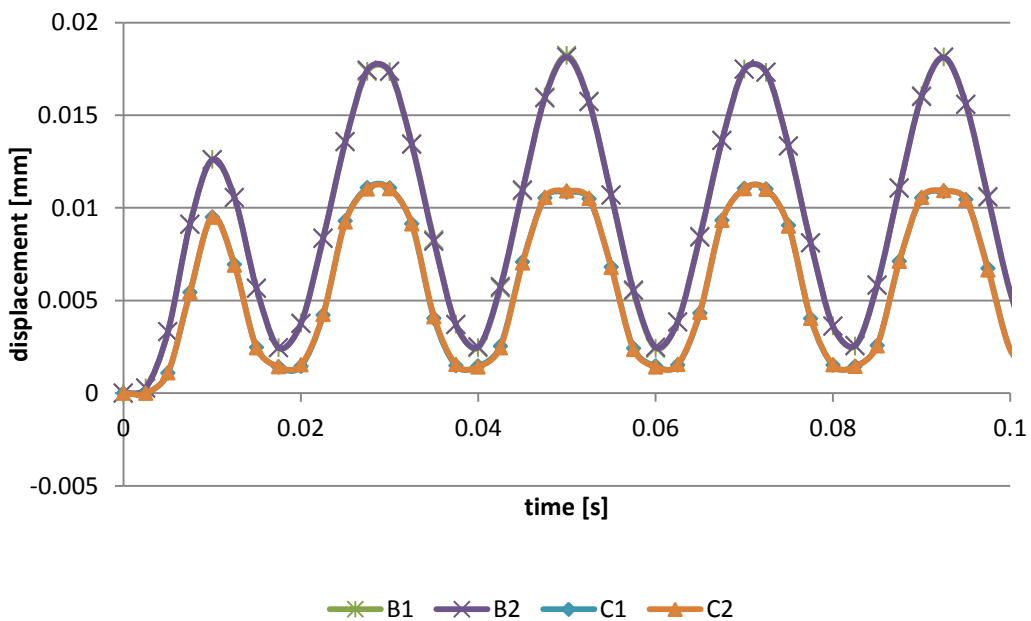
Figure 4.3.3 S-t curves without friction
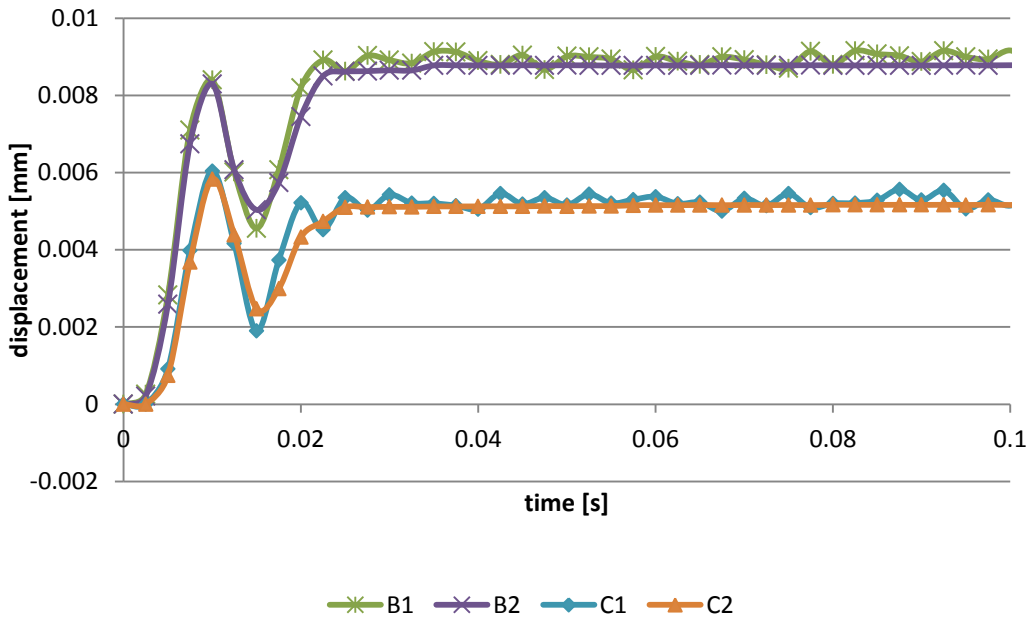
Figure 4.3.4 S-t curves with friction coefficient 0.2
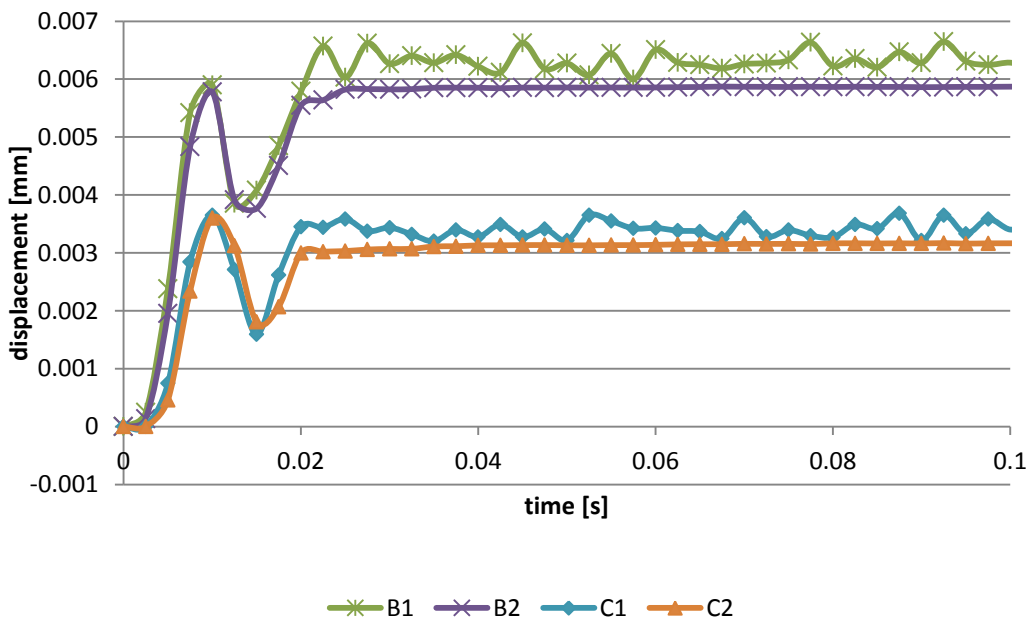
Figure 4.3.5 S-t curves with friction coefficient 0.4
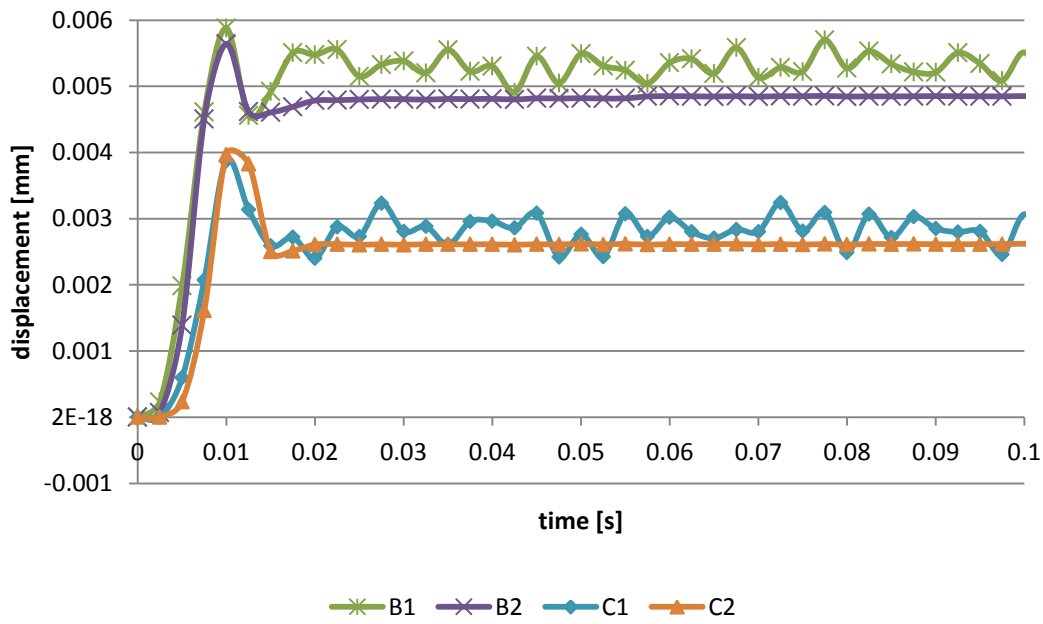
Figure 4.3.6 S-t curves with friction coefficient 0.6

Table 4.3.1 is the first peak of displacement with different friction coefficients on each point.

Table 4.3.1 The first peak of elastic displacement [mm]

	no friction	friction 0.2	friction 0.4	friction 0.6
A1	13.3939	9.47216	7.52289	6.6853
A2	13.3936	9.23887	7.32293	6.99702
B1	0.012601	0.00839908	0.00589997	0.005879
B2	0.012592	0.00829586	0.00577895	0.005643
C1	0.009492	0.00603835	0.00364974	0.003873
C2	0.009491	0.00582929	0.00359931	0.003966

Strain energy and viscous dissipation

Figure 4.3.7 and figure 4.3.8 show the strain energy on Point A1 and Point 2, which represent the center points and interface points. The points on the interface are influenced directly by the friction. The more friction causes more deformation, more strain and more strain energy certainly. It behaves completely opposite of displacement.
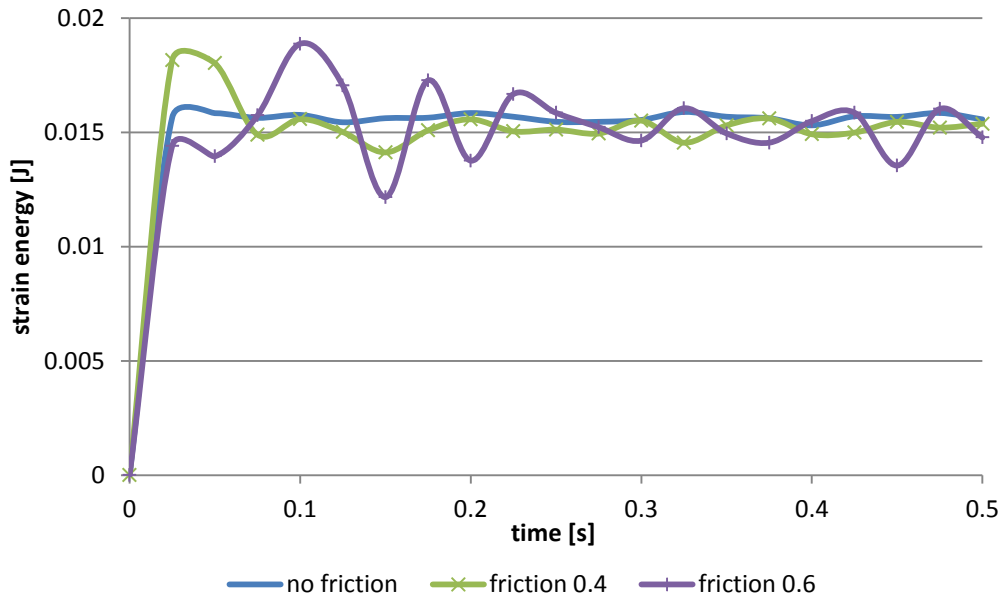
Figure 4.3.7 Strain energy of Point A1 of elastic model
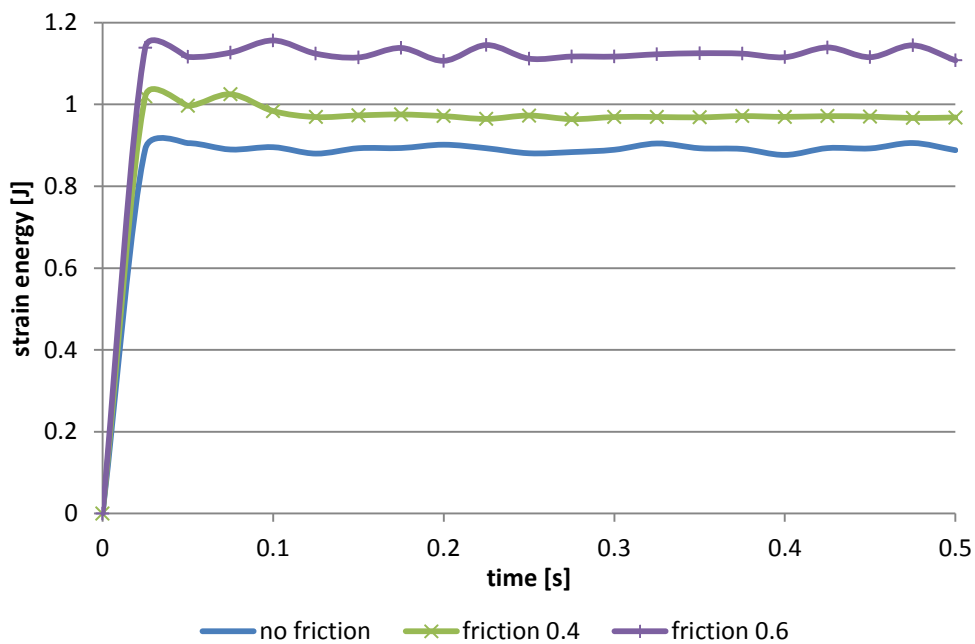
Figure 4.3.8 Strain energy of Point A2 of elastic model

Here the viscous dissipation is only caused by friction. The effect of friction on the viscous dissipation is the same with that on strain energy. But what the differences between Point A1 and Point A2, that are shown here, are that the increase of viscous dissipation of center point is gradual, however the viscous dissipation of the points on the interface with large friction coefficient (0.4 and 0.6) increases rapidly at the beginning, then maintains at peak level in the following. But there is no this phenomenon in the case of friction 0.2. Because when there's enough friction to resist the impulse loading, the point on the interface will have larger deformation first, and in the following, as the effect of loading grows the friction is not enough to

resist, the point on the interface will start to move and leads to displacement. And the friction, is the slipping friction exactly, maintain stable. It needs to be pointed out, Point A1 is at the center and is not affected by the friction directly, at the same time the material used here is only elastic. These are the reason why the value of viscous dissipation energy of Point A1 is very small.
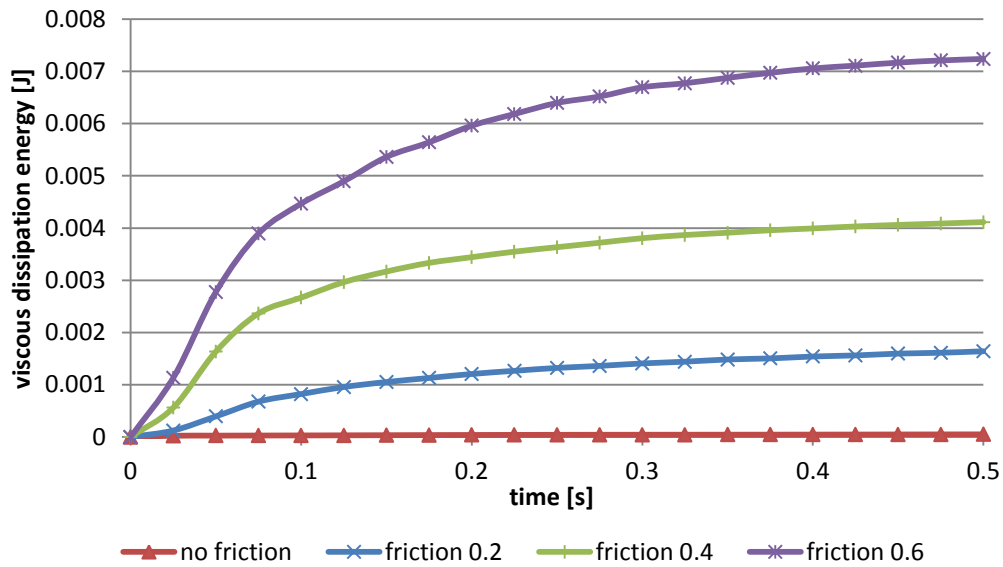
Figure 4.3.9 Viscous dissipation energy of Point A1 of elastic model
with different friction coefficient
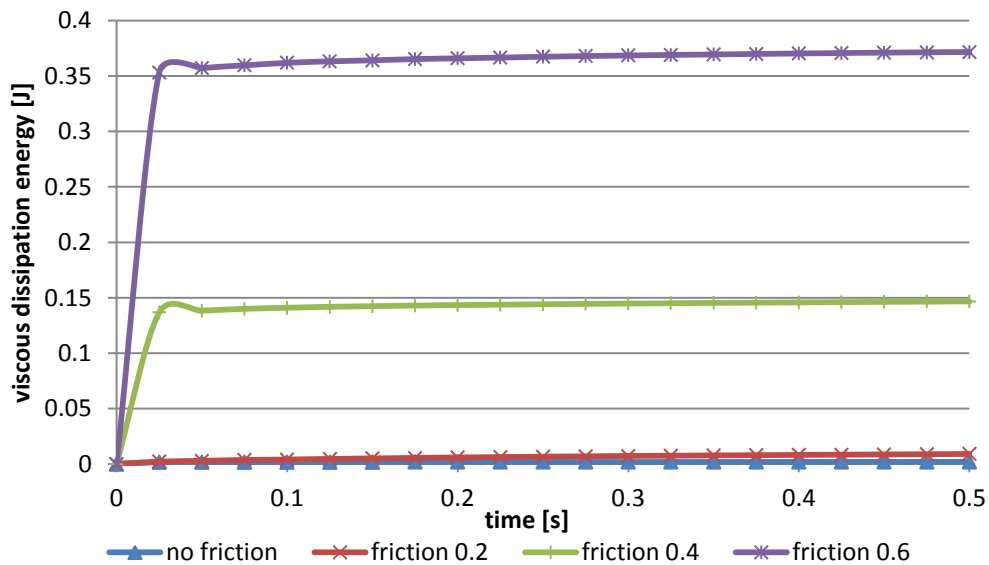
Figure 4.3.10 Viscous dissipation energy of Point A2 of elastic model
with different friction coefficient

4.3.2 Constitutive model

Figure 4.3.11 shows the displacement of Point A1 of different constitutive models without friction. It is obvious that the results of elastic model and Drucker-Prager linear model are the same. While the Drucker-Prager cap model shows a much more displacement. The first peak is

nearly 100mm, 80mm larger than that of elastic model.
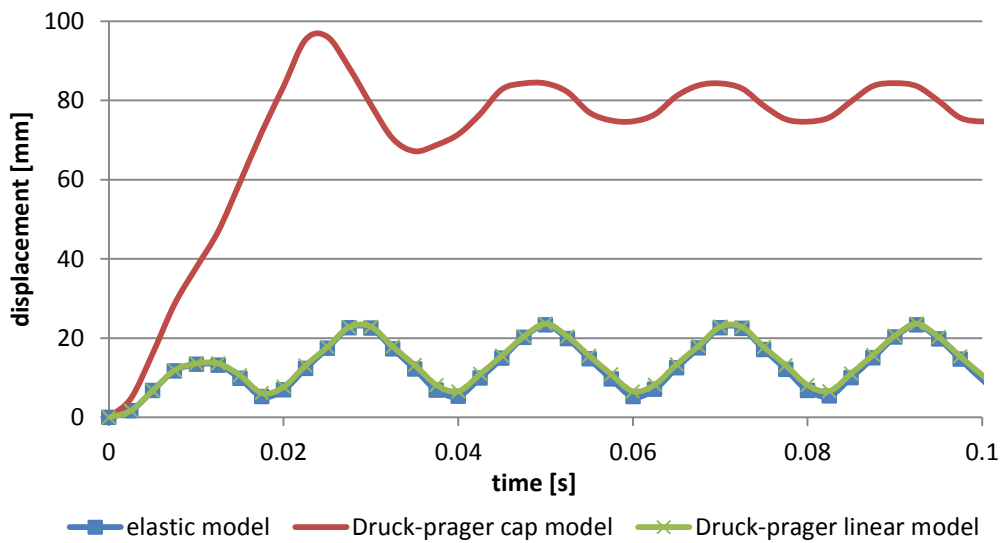
Figure 4.3.11 S-t curve of Point A1 without friction

When with friction coefficient 0.2, the displacement of Drucker-Prager cap model increases gradually at beginning and maintain stable at peak level in the following. But the s-t relation of Drucker-Prager linear model has the first peak and then continues growing to a higher level. The friction leads to only a little difference between Point A1 (at the center) and Point A2 (on the interface) in both two models. Except Point A1 and Point A2, the displacements of others are very small because of their deep positions.
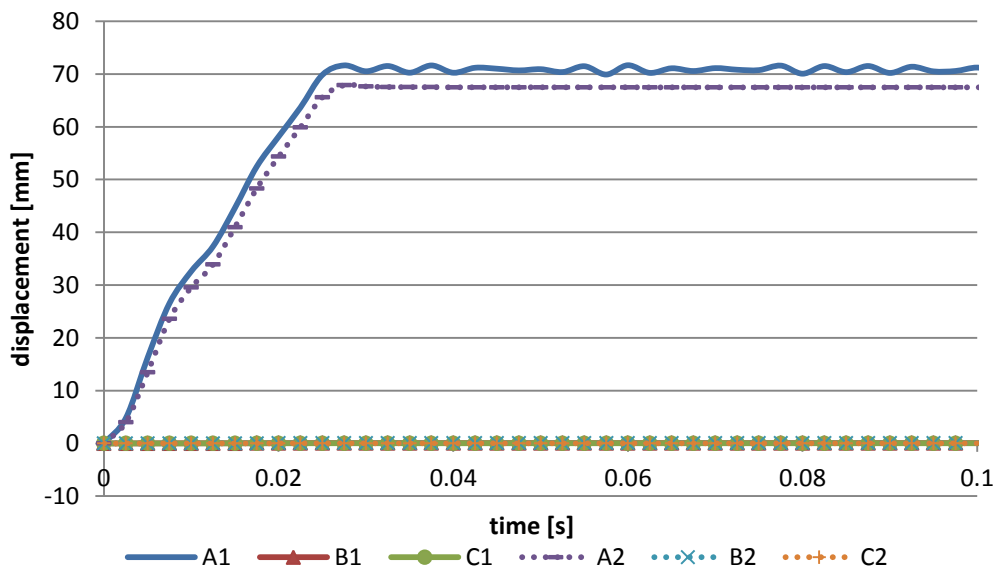
Figure 4.3.12 S-t curve of Drucker-Prager cap model with friction coefficient 0.2
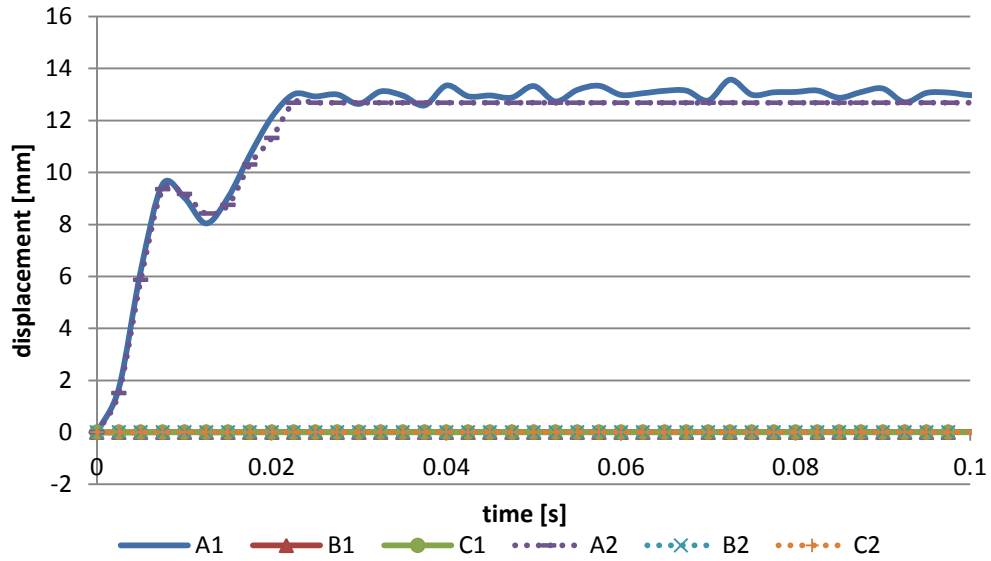
Figure 4.3.13 S-t curve of Drucker-Prager linear model with friction coefficient 0.2

Figure 4.3.14 and figure 4.3.15 show the differences between elastic model and Drucker-Prager linear model. The results of these two models are almost same. The differences are very small, and become a little larger with the friction increasing.
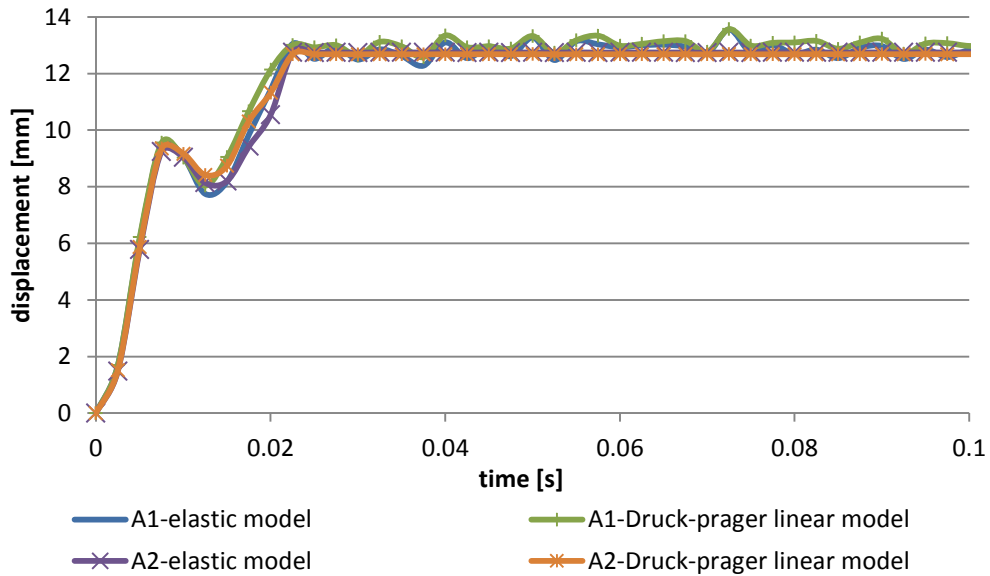

Figure 4.3.14 S-t curve of elastic model and Drucker-Prager linear model
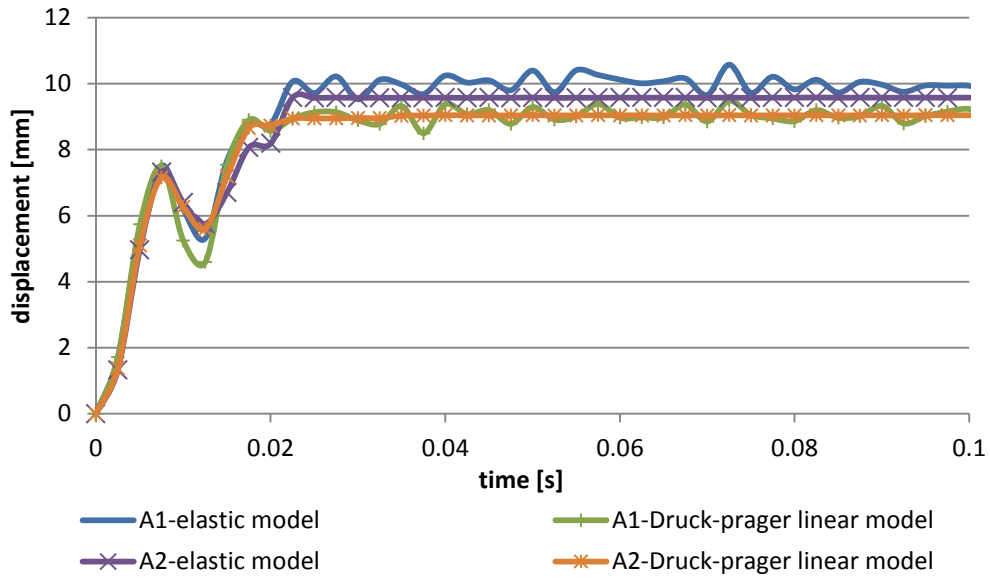with friction coefficient 0.2

Figure 4.3.15 S-t curve of elastic model and Drucker-Prager linear model
with friction coefficient 0.4

Figure 4.3.16 and figure 4.3.17 show the comparisons between Drucker-Prager cap model and Drucker-Prager linear model with different friction coefficients. In cap model around 0.01s, it appears a first peak but it is very week and inconspicuous. And around 0.02s or just after 0.02s, it appears the real first peak, and then maintains stable at this peak level when with friction or starts oscillating when without friction. However in the linear model, around 0.01s, it shows the really obvious first peak and then reincreases. When with friction it reaches next higher peak around 0.02s earlier than that of cap model, then remains stable. When without friction it reaches next higher peak at almost the same time then starts oscillating. From the point of view of quantity, the displacement of cap model is nearly 4 times of displacement of linear model.
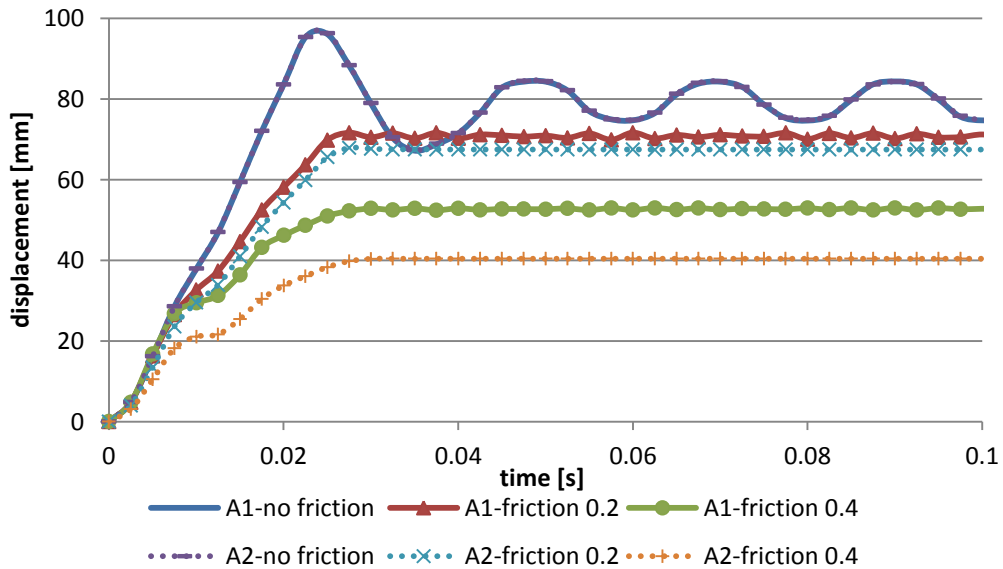

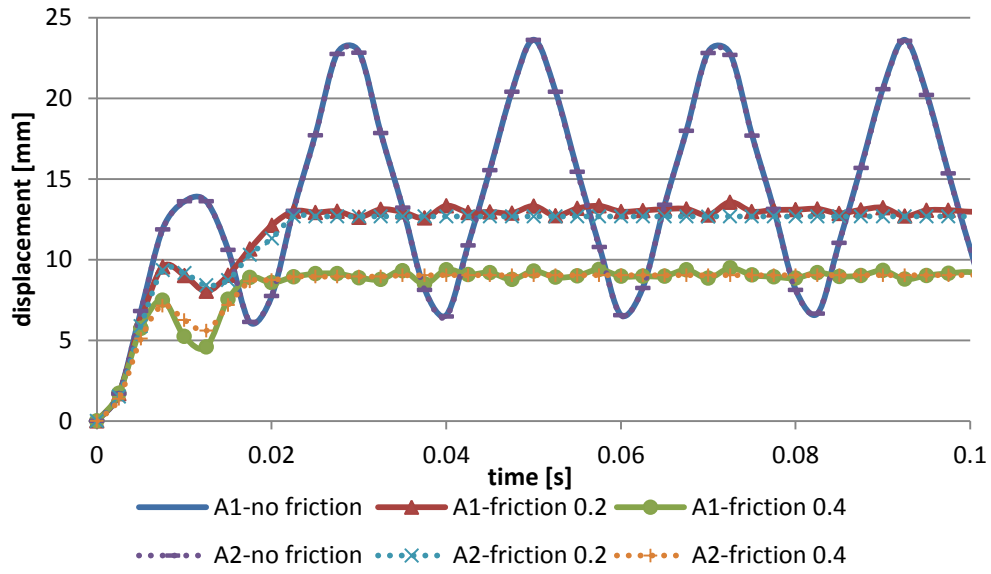Figure 4.3.16 S-t curve of Drucker-Prager cap model

Figure 4.3.17 S-t curve of Drucker-Prager linear model

Chapter 5 Numerical Results of Experimental Waves

In this chapter, the four experimental waves are loaded on the Abaqus model respectively. The input waves are illustrated in Figure 5.1. It shows the results of acceleration, displacement and stress under each load wave. And comparisons with the experimental results and PFC model results are processed.
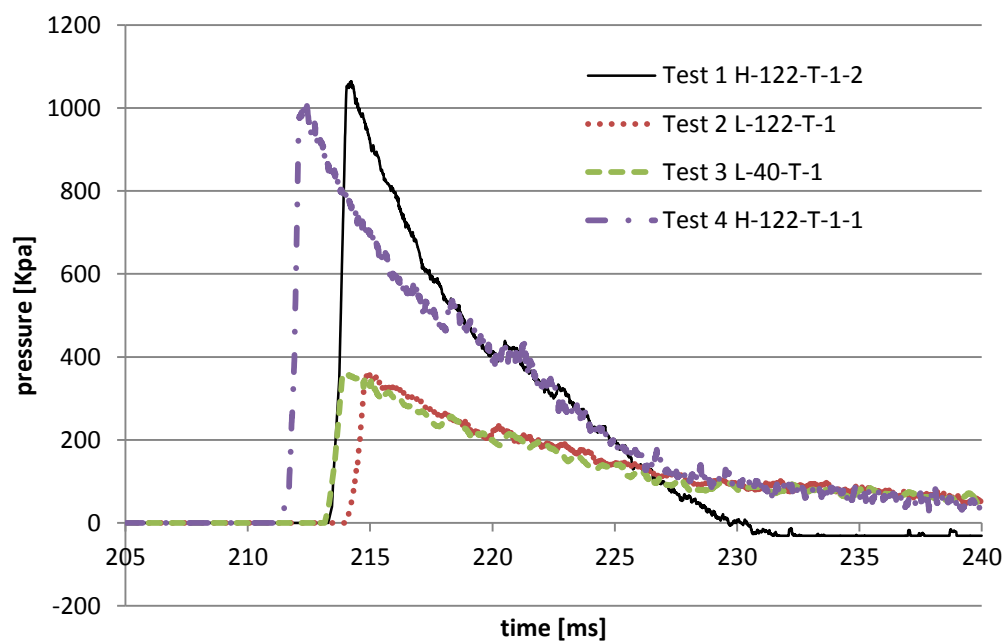

Figure 5.1 Input waves

In the experimental tests, the results of acceleration are obtained from the accelerometers A1-A12. The directions of them are listed in Table 5.1.

Table 5.1 Directions of accelerometers

section	Name of accelerometers	Directions of acceleration
Loading section	A1	Longitudinal
	A2	Longitudinal
	A3	Longitudinal
	A4	Longitudinal
section A-A	A5	Longitudinal
	A6	Vertical
	A7	Longitudinal
	A8	Vertical
section B-B	A9	Longitudinal
	A10	Vertical
	A11	Longitudinal
	A12	Vertical

Since the Abaqus model is created as axial-symmetric and the rotation of the shock tube in the real test procedure is not considered, the accelerometer results of vertical direction are not taken to analyze and compared with numerical results. So here only accelerometer A1 (respect to Point A1 of Abaqus model), accelerometer A2 (respect to Point A2 of Abaqus model), accelerometer A5 (respect to Point B2 of Abaqus model) and accelerometer A9 (respect to Point C2 of Abaqus model) are considered to analyze. And also the longitudinal force of both top and bottom section and longitudinal displacement of the soil specimen are considered to analyze between PFC model and Abaqus model.

5.1 Test 1 H-122-T-1-2

The input impulse of pressure can be seen as two parts. The first one is at high level of pressure more than 800KPa from around 213ms to 216ms. And the following period after 216ms is at relatively low and negative level of pressure (-30KPa) compared to the peak pressure. This loading character will affect directly the characters of results.

5.1.1 Results of acceleration

5.1.1.1 Chamber friction coefficient 0.4

Figure 5.1.1 – Figure 5.1.4 illustrate the results of accelerometer A1, A2, A5 and A9 from experimental test and two numerical model. In the PFC model, the friction coefficient used between soil specimen and tube chamber is 0.4, which is the same used in the Abaqus model. But from the comparisons in the figures, it seems the results from Abaqus model have a little big difference from that of other two, no matter in which case of material constitutive law.
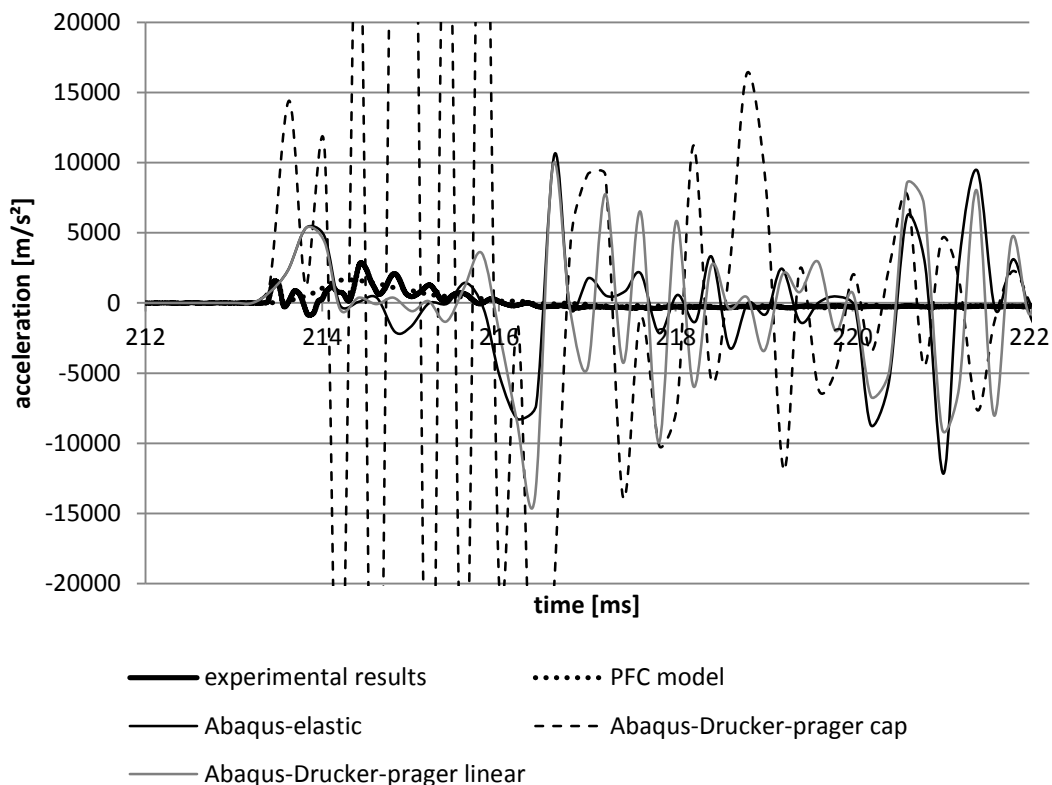
Figure 5.1.1 Experimental and numerical results of accelerometer A1
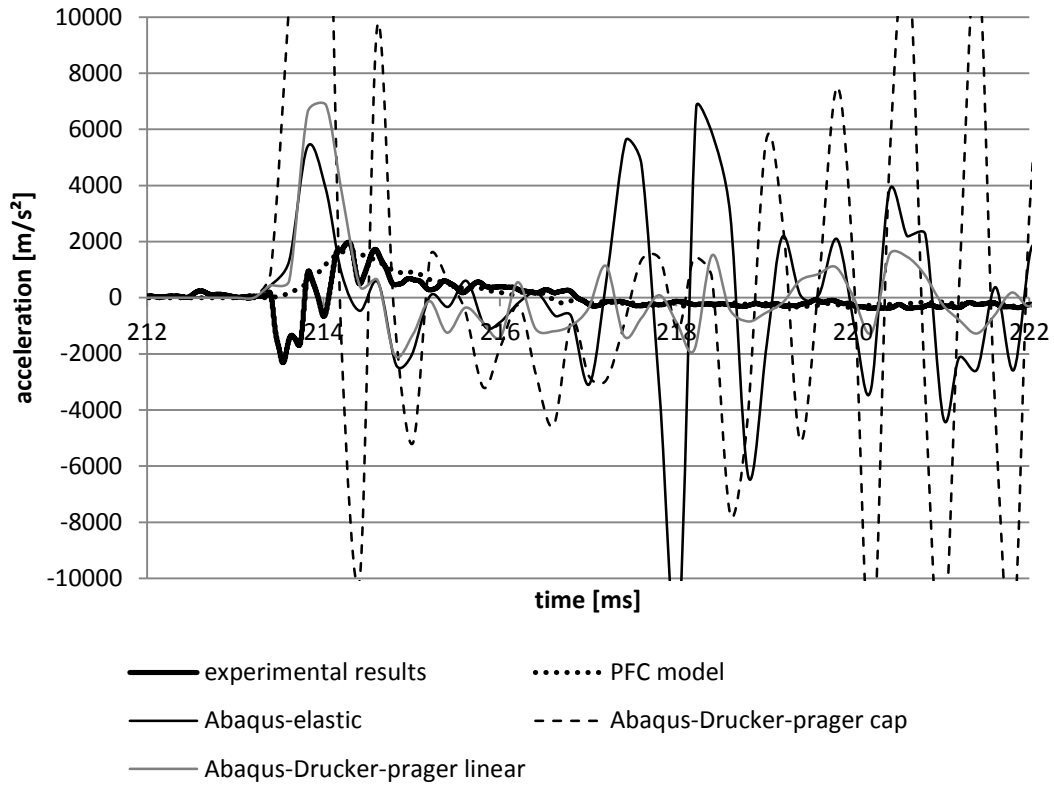
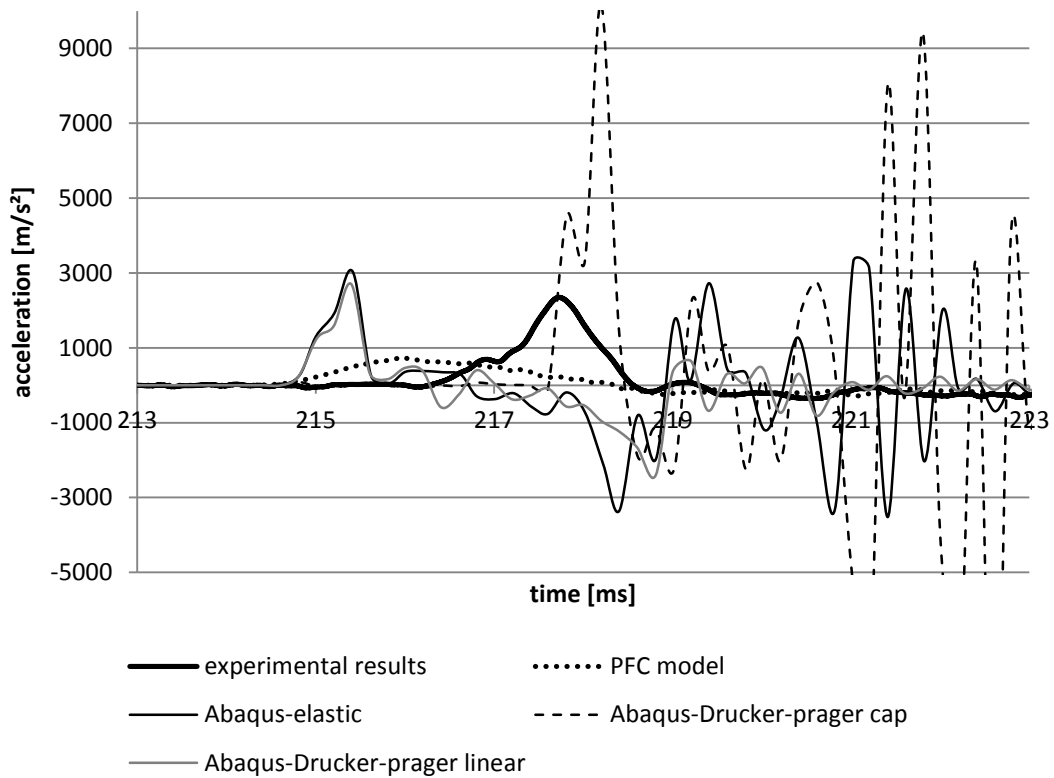Figure 5.1.2 Experimental and numerical results of accelerometer A2

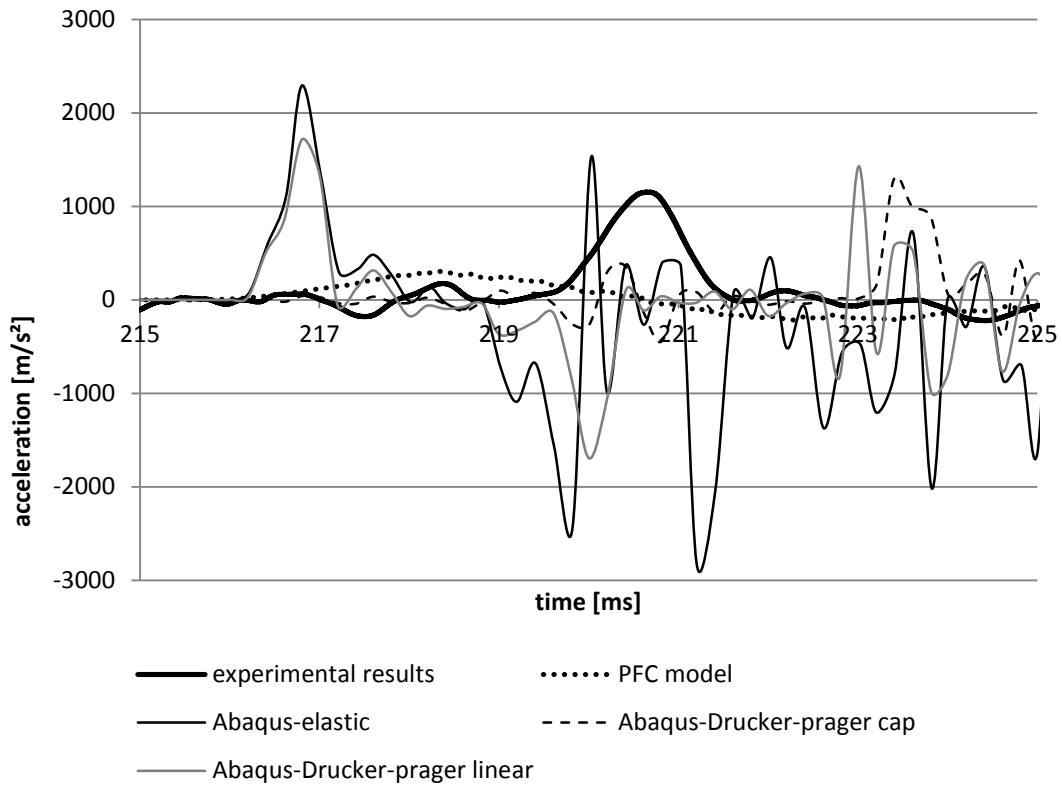Figure 5.1.3 Experimental and numerical results of accelerometer A5

Figure 5.1.4 Experimental and numerical results of accelerometer A9

5.1.1.2 Chamber friction coefficient 0.6

In the Figure 5.1.5 - Figure 5.1.8, the friction coefficient 0.6 is used in the Abaqus model to calibrate the acceleration results. In order to show clearly in the both whole and detail scales, each figure has an enlargement of the important detail, which is putted under the main figure. It is easy to draw that the results with friction 0.6 are better than that with friction 0.4 compared to experimental results. All the amplifications of the vibration are reduced, while the shape and tend of vibration do not change.
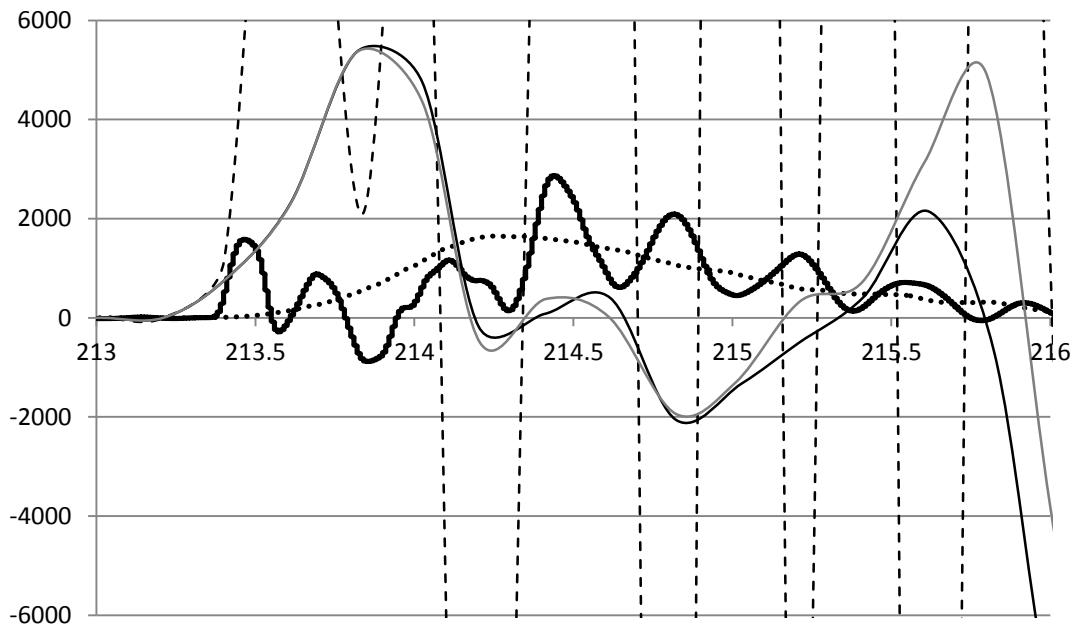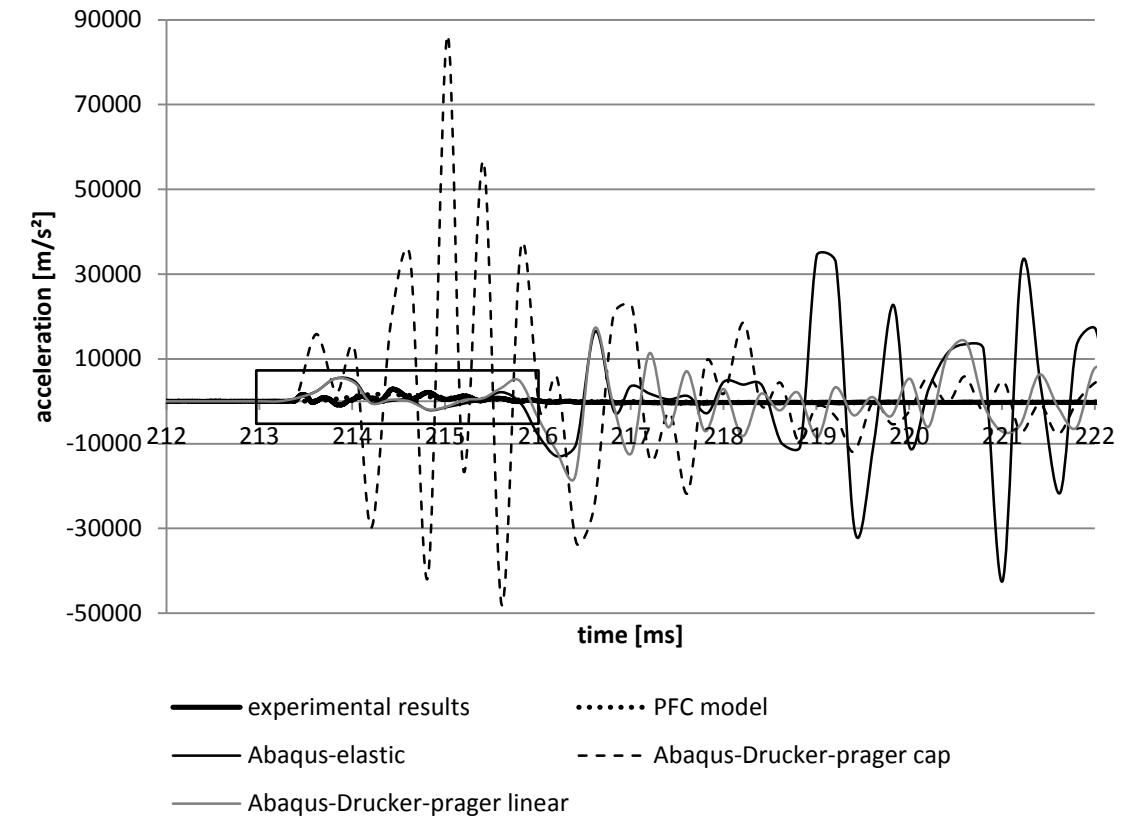
(I) Loading section

Figure 5.1.5 Experimental and numerical results of accelerometer A1

The numerical results of accelerometer A1 with the chamber friction coefficient 0.6 are shown in the upper Figure 5.1.5. A1 is on the center of loading section, it gives the longitudinal

acceleration. From the figure, it can be seen that the numerical results of PFC model are nearly smooth and steady average of experimental results. The first peak of experimental acceleration appears around 213.5ms, while the highest peak appears around 214.5ms. So the PFC model shows the larger plasticity, viscosity and insensitivity. The main oscillations are in the period around 213ms to 216ms, in which the input load appears the peak and the pressure is at high level. After this, the results of experiments and PFC all tend to be zero, as the input pressure goes to be a lower level.

The accelerations of A1 from Abaqus model show different characters from different materials. They are larger at different levels than that from experiment and PFC model. The trend of vibrations given by Drucher-prager model is the same with that from experiment and PFC model. At the period of peak and high level of pressure, it behaves big vibrations, of which the highest peak reaches $80000m/s^2$, it is more than 20 times of experimental and PFC results ($3000m/s^2$). After this, at lower level of pressure, it goes to rather less oscillations around zero.

While on the opposite, the elastic model gives the complete different trend. In the period of high level of pressure, the first peak reaches more than $5000m/s^2$, which is much lower than that of cap model, and it appears a little later. However, in the next period, when the input pressure goes to a relative low level, the oscillation of acceleration of elastic model goes rather large, which absolute is more than $30000m/s^2$. This is caused by the material characteristic, elastic model. Under the high impulse of load, the larger input energy is stored in the material, and there's no way of energy dissipation because of elasticity. The friction directly effect on the interface between soil and chamber, thus the center of section will be influenced later (after 222ms) and lower.

On the other hand, the Drucher-prager linear model seems multiplied the characters of cap model and elastic model. At high level of pressure, it shows the similar behavior of elastic ones, while at the next period, it goes to be similar with cap model.
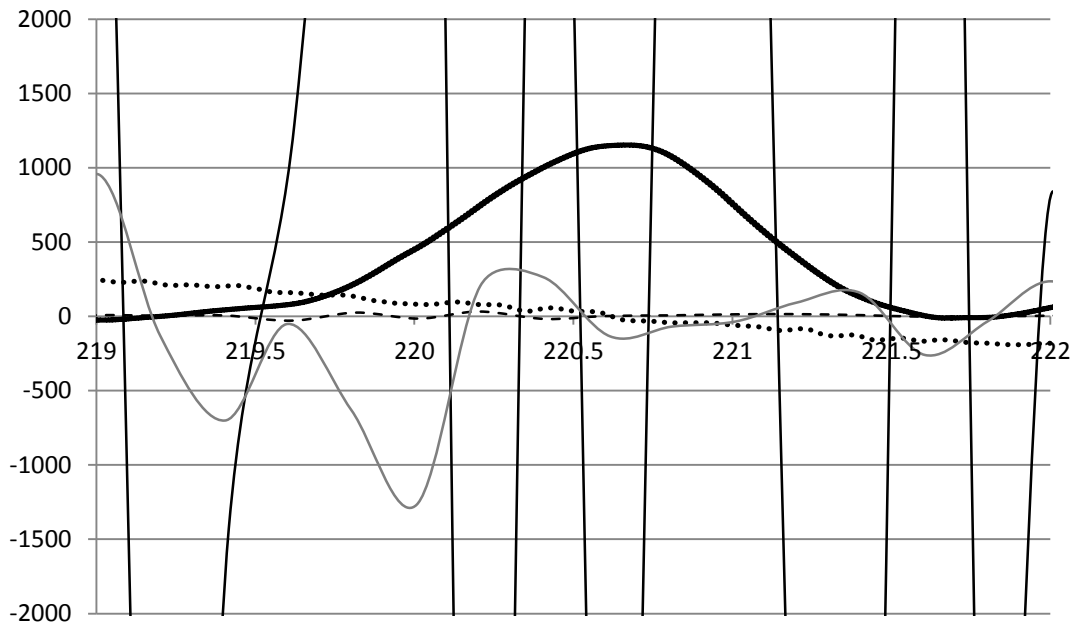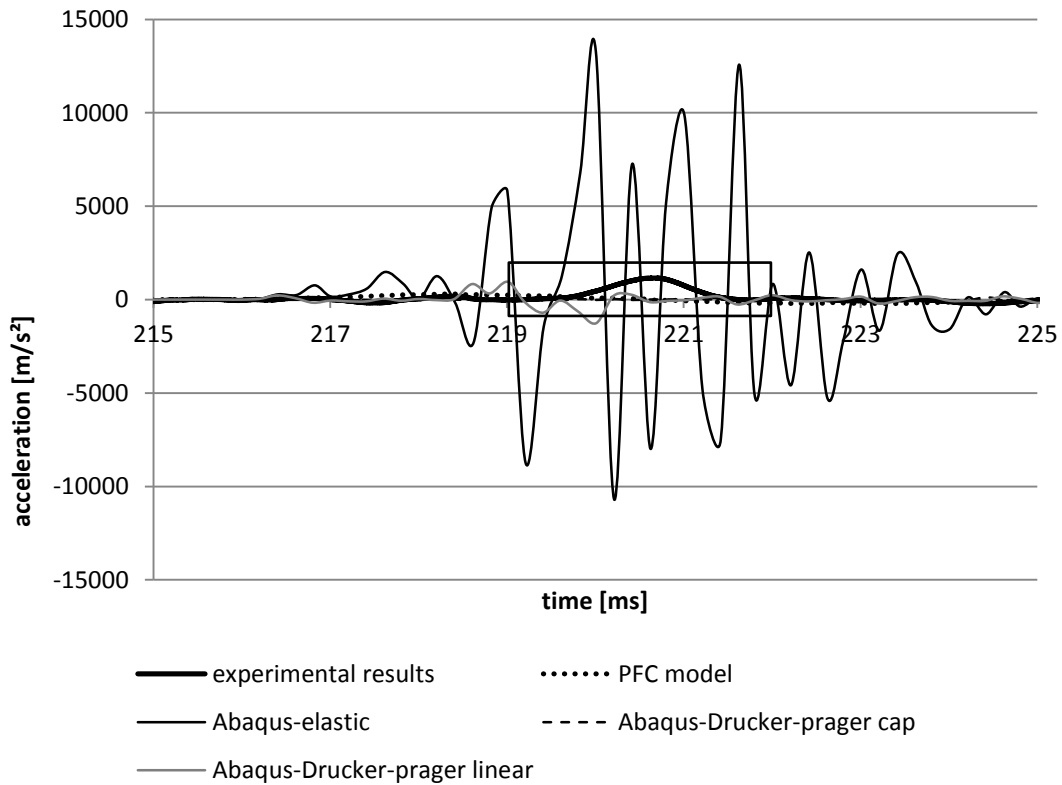
Figure 5.1.6 Experimental and numerical results of accelerometer A2

Accelerometer A2 is near the interface which is directly influenced by friction. The experimental and numerical results are illustrated in the Figure 5.1.6, the regularity is mostly similar but clearer and more apparent with that of A1. The effect of friction is performed around 220ms, which is earlier than that of A1, because of its position.

(II) Section A-A

Accelerometer A5 is placed on the section A-A near the interface, recording the longitudinal acceleration. Section A-A is 400mm deep from the loading section, which shows the influence of impulse at a little further position.
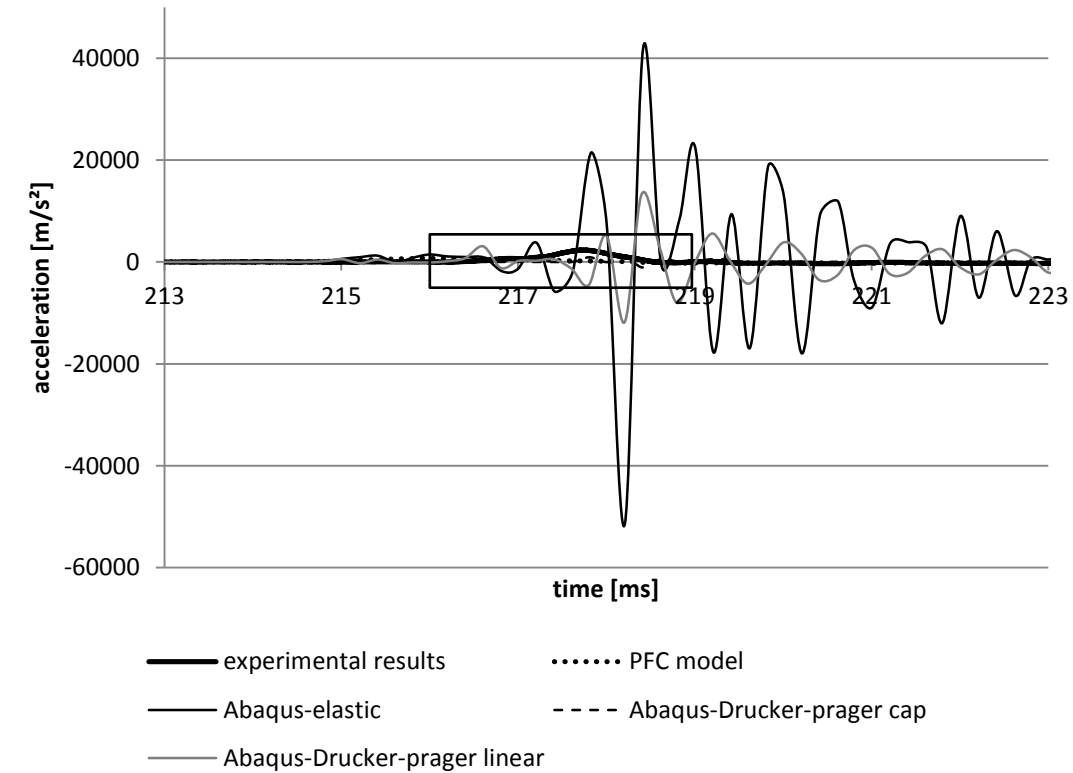

Figure 5.1.7 Experimental and numerical results of accelerometer A5

Figure 5.1.7 illustrates the experimental and numerical results of accelerometer A5, the friction coefficient between chamber and soil is 0.6. It can be seen from the figure that the features of two periods which is clearly shown previously in the loading section are not obvious here at the deeper position in soil specimen. Under all the cases of models, there seems only one peak period of vibration, which is the range of biggest influence caused by impulse.

The experimental results give only one maximum value of acceleration, around 2500m/s^2, appears near 217.75ms. However the acceleration of PFC model seems more stable, the only one peak of PFC model is very unobvious, which appears earlier than that of experiment, around 216ms with amplification of 1000m/s^2, less than the half of experimental value.

The results from Abaqus model have some vibration in the biggest influenced range. The elastic model shows the widest range of 6ms (from 217ms to 223ms) and the largest amplification. While the Drucher-prager linear model is at second rank, its range is from 218ms to 220ms, during 2ms. But it has to be noticed, this period is not very clear and easy to be distinguished. Because the vibration does not go sharply and dramatically in this case. At last the acceleration from Drucher-prager cap model gives more reasonable results compared to experimental ones. The influenced period is from 217.7ms to 218.7, lasts for 1ms. The amplification is about 1000m/s^2. Out the influenced period, there seems no oscillation.

It can be draw from the descriptions; the impulse of the loading pressure is reduced at further depth.

(III) Section B-B

Section B-B is 400mm deeper than section A-A. Accelerometer A9 is near the interface recording the longitudinal acceleration. Figure 5.1.8 shows the experimental and numerical results of A9.
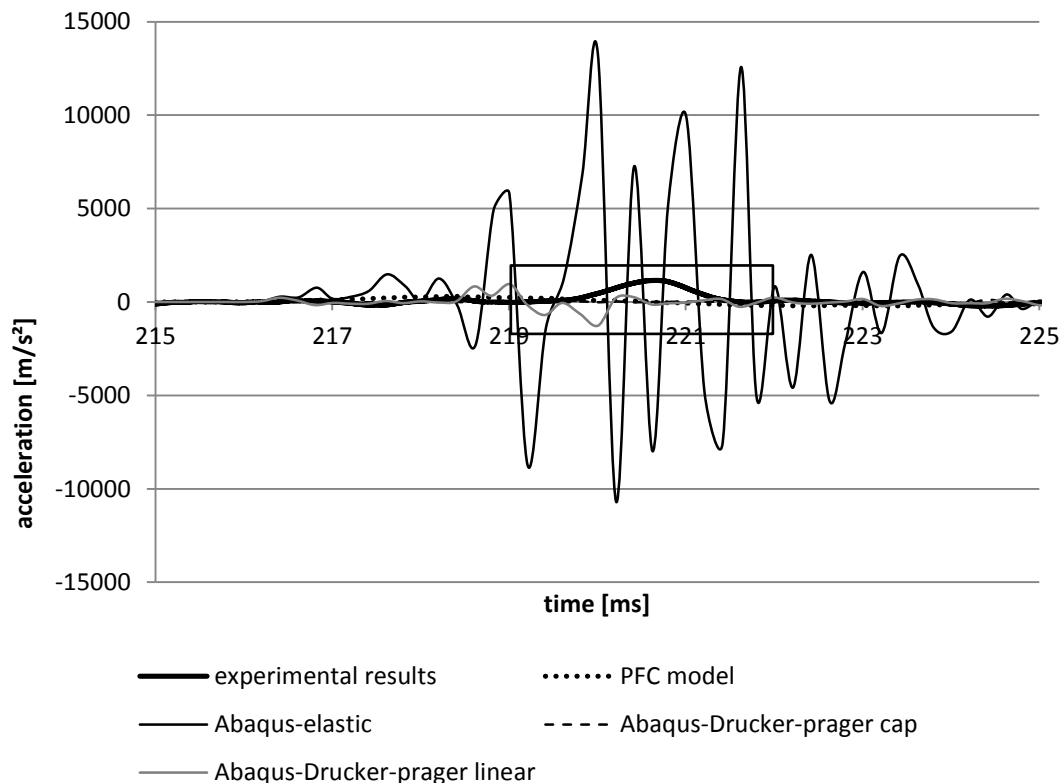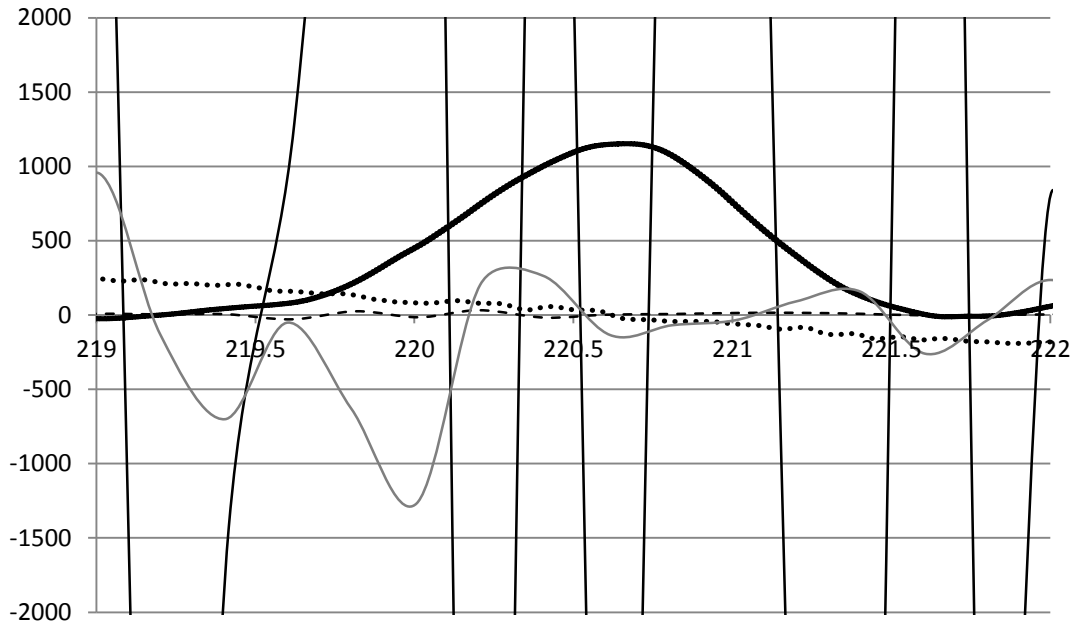
Figure 5.1.8 Experimental and numerical results of accelerometer A9

The trend seen from Figure 5.1.8 is similar with accelerometer A5. All the ranges of vibration amplifications are reduced and delayed as the depth goes larger. The peak value of experimental results is around 1200m/s^2, and appears around 220.7ms, which is about 3ms later as the depth goes 400mm deeper. The results of other model are also delayed relatively 2-3ms. It is because the energy of impulse is dissipated by friction and material plasticity, where the material plasticity plays the main and more important role.

5.1.2 Results of longitudinal force

In this part, the longitudinal forces on the center point of loading section (A1) and the bottom section (D), which is the right wall and the left wall in the PFC model, are shown. In order to compare the results between different numerical models, the friction coefficient between soil specimen and chamber used in Abaqus model is 0.4, which is the same with that used in PFC model.
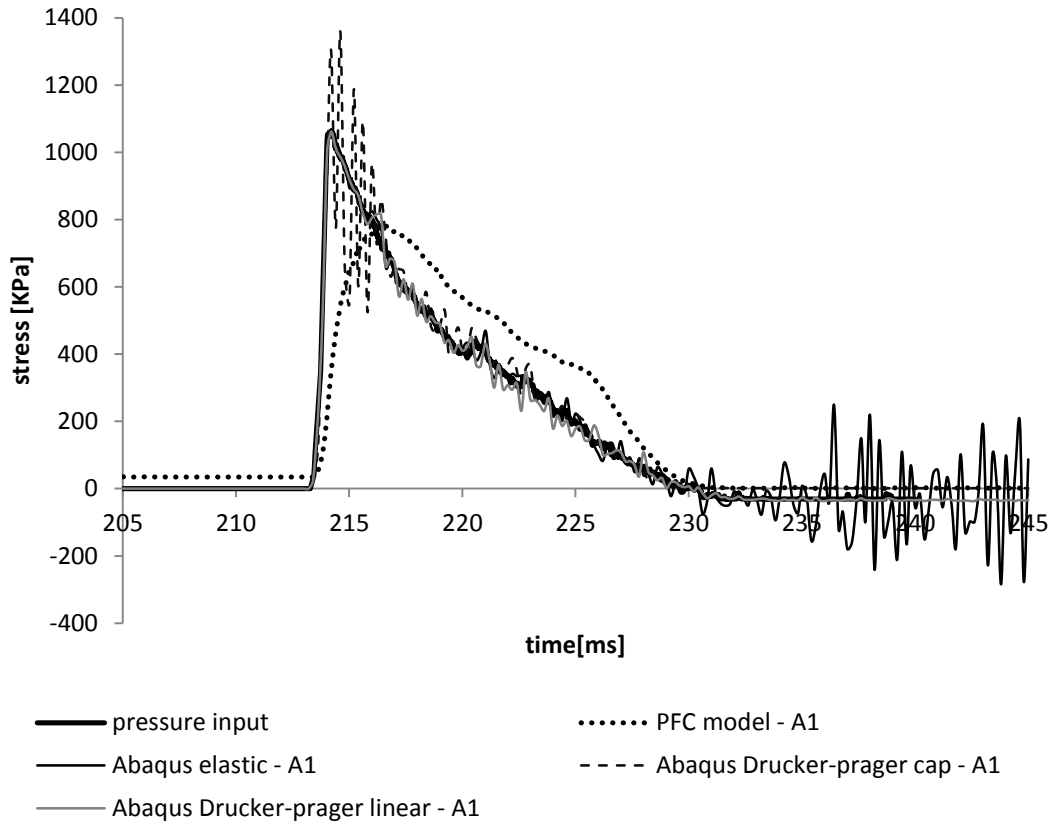
Figure 5.1.9 stress of center point on the loading section (top section Point A1) with friction 0.4

Figure 5.1.9 shows the stress of Point A1 from both numerical models. As the description seen previously, the Drucher-prager linear model gives the most reasonable result, which is not very clear to be seen in the figure, because it almost superposes the input pressure. It has only very small oscillations around the input pressure. The Drucher-prager cap model also gives the fitted results, except the 2ms just after the peak pressure, during which the oscillation around the value of input pressure gets large amplification. While the results of elastic model during loading are similar to input pressure, but after 230ms when the input pressure maintains stable at a small negative value, the elastic model goes into relatively sharp vibration. This is also the result caused by material elasticity as analyzed before. Here, the PFC model shows less sharp and fitted results compared to Abaqus model, because the impulse load is simulated to act on rigid plane of loading section, on which the displacements of each point are the same, this in turns influences the stresses of each point on the section. This is the reason why the stress of center point A1 of PFC model is not very fitted to input pressure. On the contrary, the impulse is directly acted on the each point of loading section, including point A1.
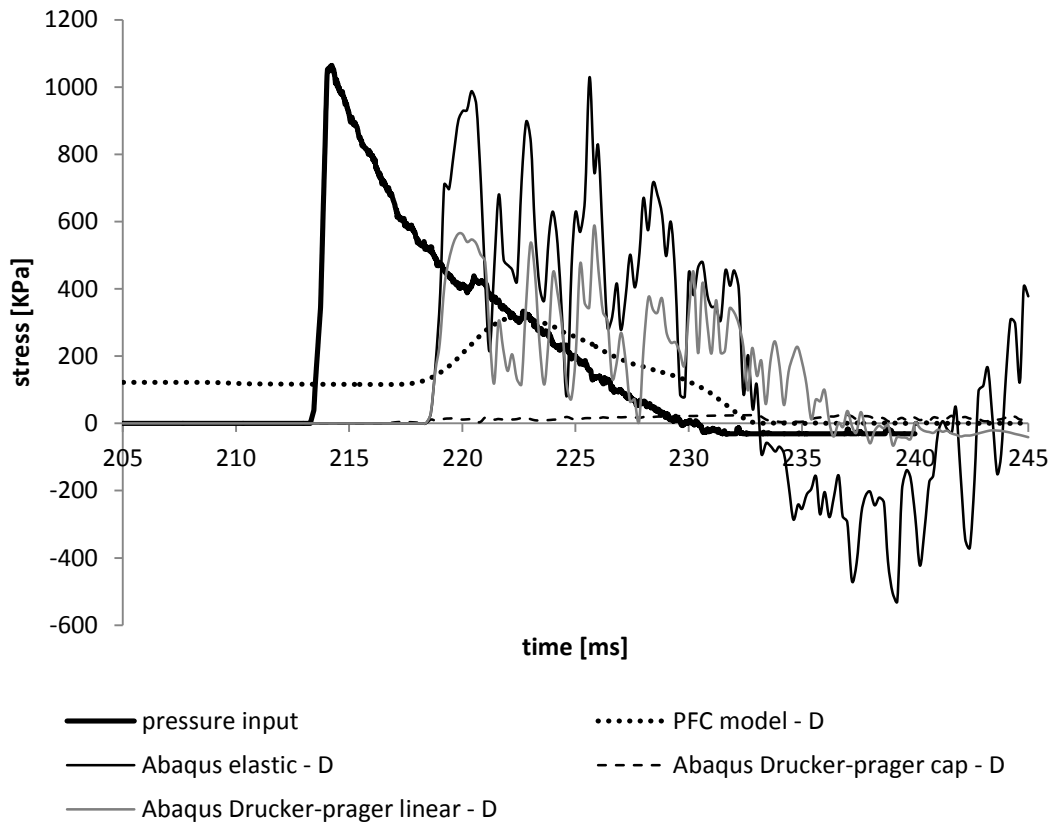
Figure 5.1.10 stress of center point on the base section (bottom section Point D)
with friction 0.4

Figure 5.1.10 illustrates the stress of the center point D of the bottom section, which is also the reflection section of dynamic wave. It is obvious that the reactions of impulse in numerical models are about 5ms delayed, which can be taken as reflection time of wave. And during the propagation of wave through the soil specimen, the material plasticity dissipates some energy, which leads to the amplifications of reflected vibration is lower than the peak of input pressure. And the lower it is, the more material plasticity behaves. So the elastic model gives the highest reflection, but still a little lower than input ones. This small decrease is caused by the friction between soil specimen and chamber, which as analyzed before does not make much contribution compared to material plasticity. What is noteworthy, the results from Drucher-prager cap model maintain at a very small value (20kpa) from starting to react. It means in this case, the load nearly cannot influence the bottom of soil. The impulse wave nearly cannot reaches to the bottom section, because of so larger dissipation through propagation.

5.1.3 Results of longitudinal displacement

In this part the longitudinal displacements from numerical models are analyzed and compared. The values of these results recorded from Abqus model is the displacement of Point A1, the center point on loading section. While the ones of PFC are taken as the differences of the displacements between right wall and left wall ($disp_{right}$-$disp_{left}$) instead. Here illustrate the comparisons of Abaqus results with different friction and PFC results.
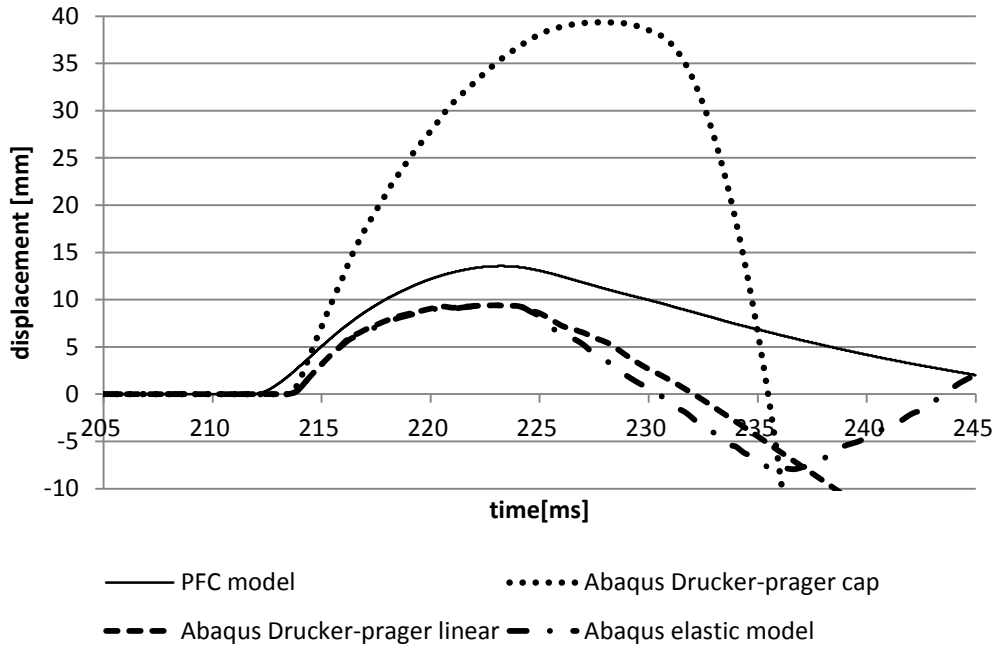
Figure 5.1.11 longitudinal displacement of PFC model (friction 0.4)
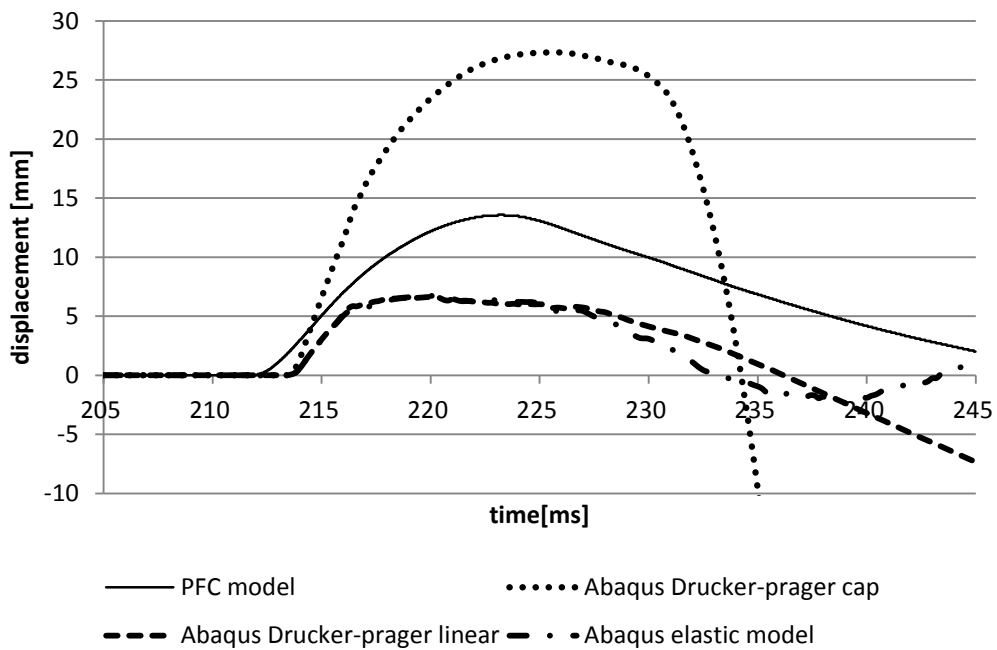and Abaqus model (friction 0.2)

Figure 5.1.12 longitudinal displacement of PFC model (friction 0.4)
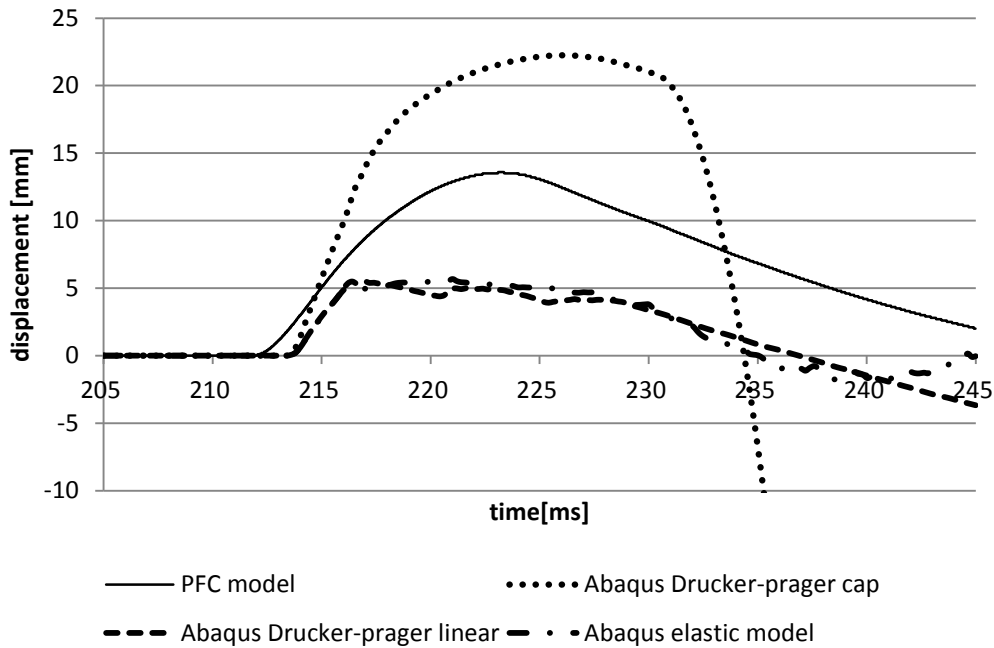and Abaqus model (friction 0.4)

Figure 5.1.13 longitudinal displacement of PFC model (friction 0.4)
and Abaqus model (friction 0.6)

It is obvious the friction only reduces the highest value of displacement in Abaqus models. The reaction time is similar among different Abaqus models, around 214ms, which is 1ms later than PFC model. This reaction time seems not influenced by friction because of its position; the center of section is far from the interface and not affected directly by the friction. At the same time the results of PFC models give 10ms delay of time when displacement reaches peak value (223ms) than the input pressure reaches peak value (at 213ms). From this point of view, elastic and Drucher-prager linear models give the similar delay of time with friction 0.2 (223ms), but with the friction gets larger they get in advance (at 216ms) with the half value (5mm) of that in 0.2 (10mm). It means that the friction resists the movements of the deeper part of soil specimen. While on the contrary, the cap model behaves larger plasticity, appears very larger displacement under loading, 40mm with friction 0.2, 27mm with friction 0.4 and 22mm with friction 0.6. The time of peak displacement also goes in advance with the friction goes larger. What needs to be noticed, the cap model gives unlimited displacements, which are not convergent at negative values. That is to say, after impulse loading, the soil specimen will rebound up to a high displacement like a bomb. This also can be seen clearly in the case of Drucher-prager linear model after 235ms, nevertheless it gives a relative small rebound value.

5.2 Test 2 L-122-T-1

The impulse pressure of test 2 is a lower load about 350KPa, it starts and reaches the peak at about 214ms. During a slow reduction for 26ms, it ends up with 40KPa at 240ms. This part shows the behaviors of models under low impulse pressure.
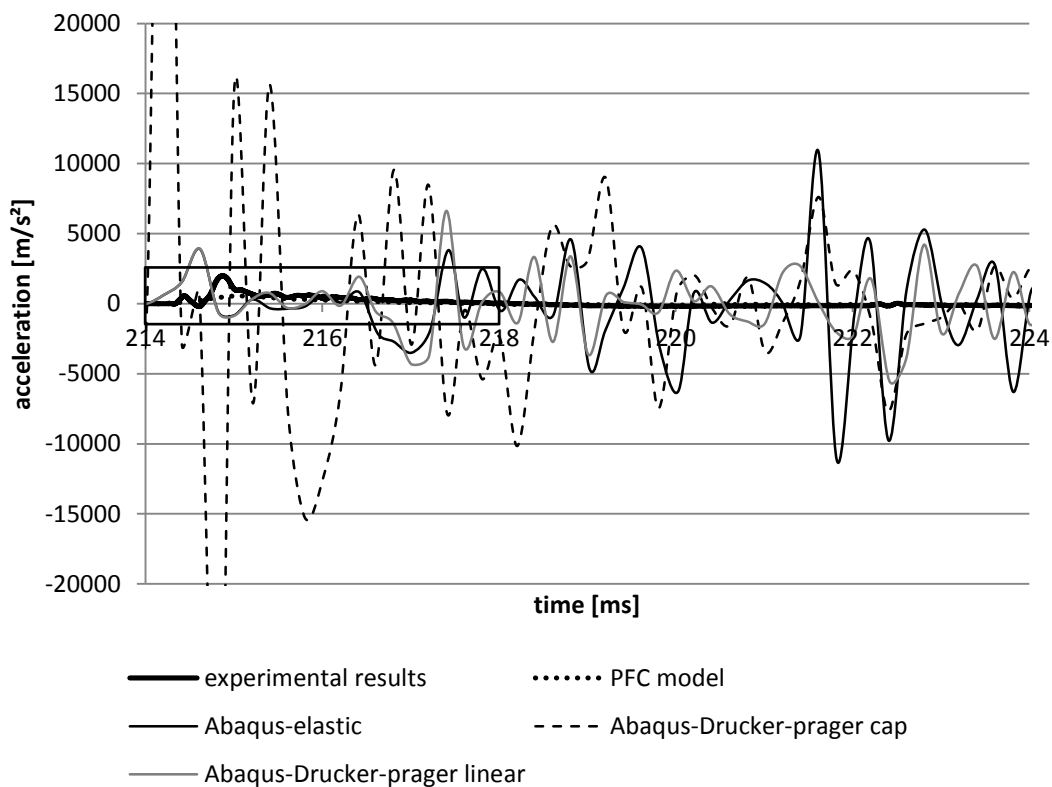
5.2.1 Results of acceleration

Figure 5.2.1 – Figure 5.2.4 describe the results of accelerometers A1, A2, A5 and A9 from different models. The friction coefficient between chamber and soil in PFC model is 0.4. However this parameter used in Abaqus models is 0.6 in this part.

(I) Loading section

Loading section is the first section that receives the impulse load. It is also the most direct section that is influenced by the impulse load. It should obtain the most energy and goes into the biggest reaction.

Figure 5.2.1 shows the accelerations of center point on the loading section.
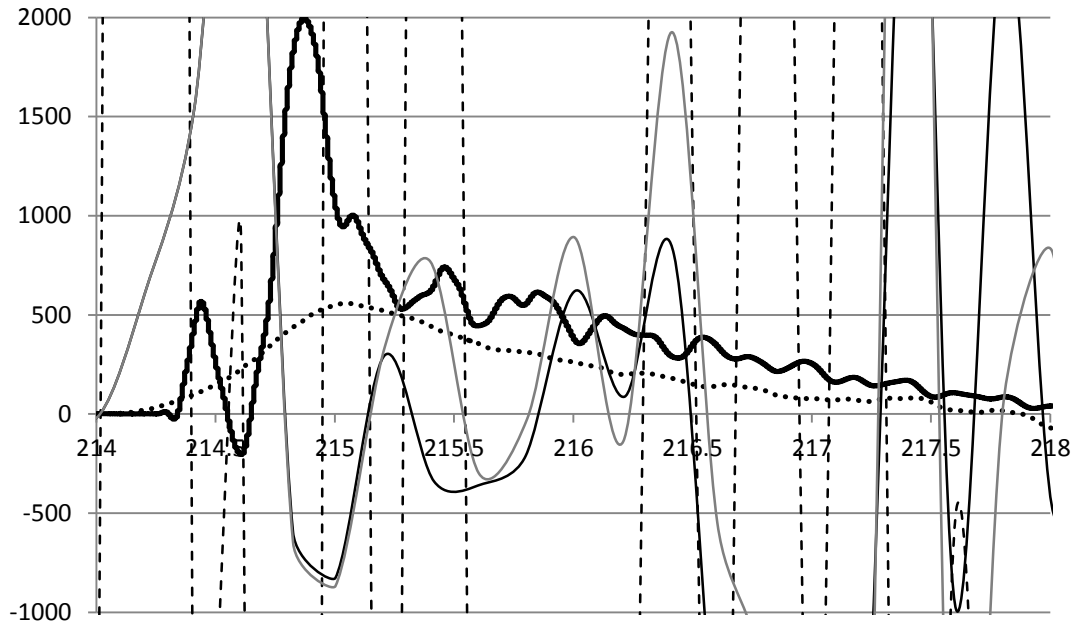
Figure 5.2.1 Experimental and numerical results of accelerometer A1

From the figure, it is can be seen that the reaction duration is from 214ms to 218ms in both experiment and PFC model, even though the experimental result gives a little delay at beginning. The input pressure during this period is more than 250KPa, which is a relative low level compared to test 1. After 218ms, the results of experiment and PFC model are zero. It means the soil in the both cases has been compacted at 218ms under the low pressure level. But the reaction period is not shown by Abaqus models. From the curves, it is hard to distinguish the reaction period. Because the models created here using Abaqus are very basic and simple continuum, it does not have enough damping to dissipate the impulse energy. And also, A1 is the center point, which is not affected directly by the friction. On the contrary, A2 is near the interface, which is affected directly by the friction. Figure 5.2.2 gives the results of accelerometer A2.
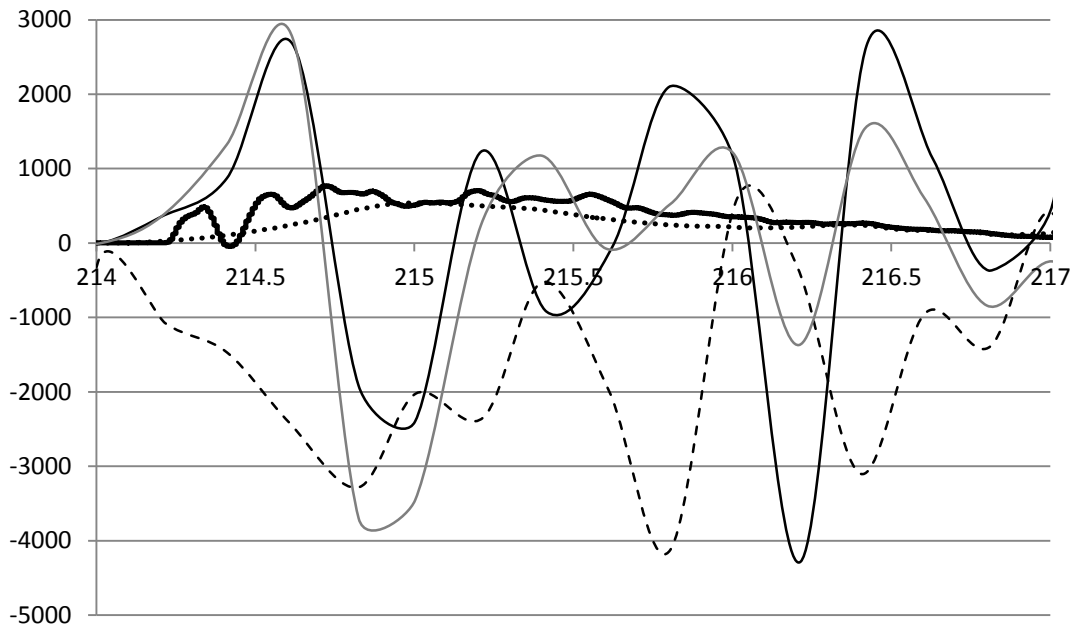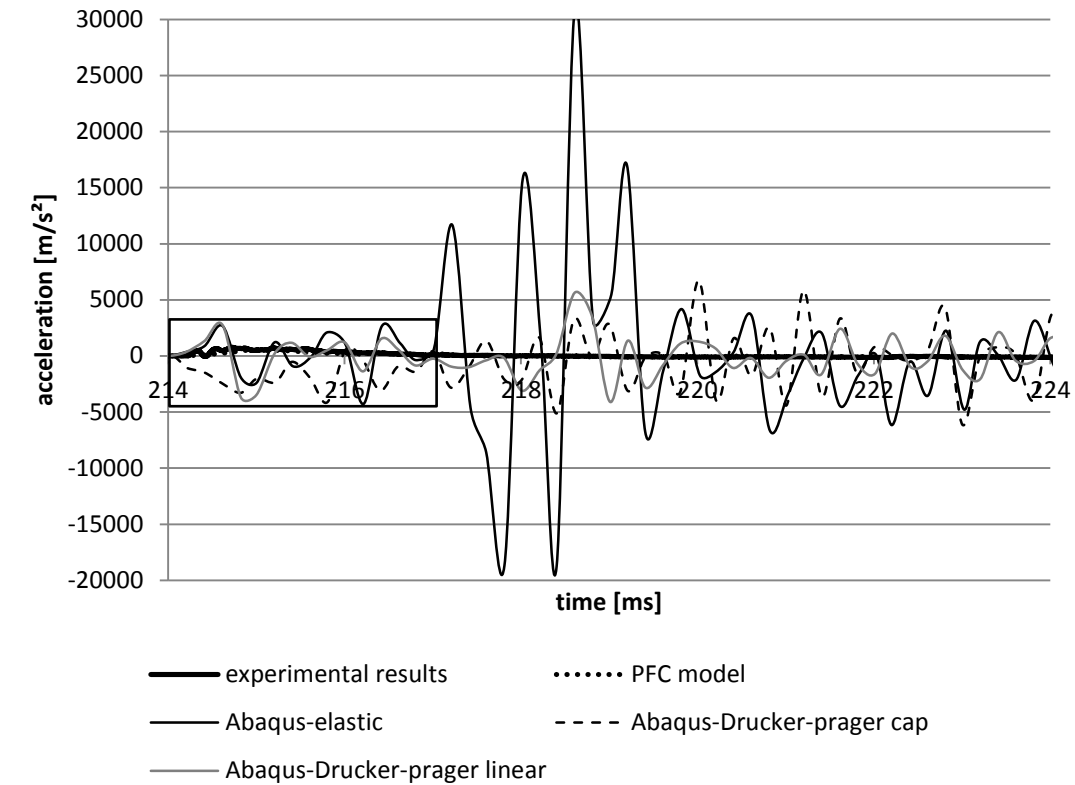
Figure 5.2.2 Experimental and numerical results of accelerometer A2

From Figure 5.2.2, it is obvious in all cases that the reaction period is from 214ms to 217ms. The peak values of experimental test and PFC model are less than 1000m/s^2, while the Abaqus models give the values of 3000-4000m/s^2. After this period, the results of experiment and PFC model approach stably to zero. But there are still oscillations in the results of Abaqus models. Especially in the elastic model, since the friction is the only one factor of dissipation, the oscillation of accelerations in the elastic model is very high.

(II) Section A-A

Section A-A is 400mm far from the loading section. Figure 5.2.3 illustrates the experimental and numerical results of accelerometer A5 (near interface).
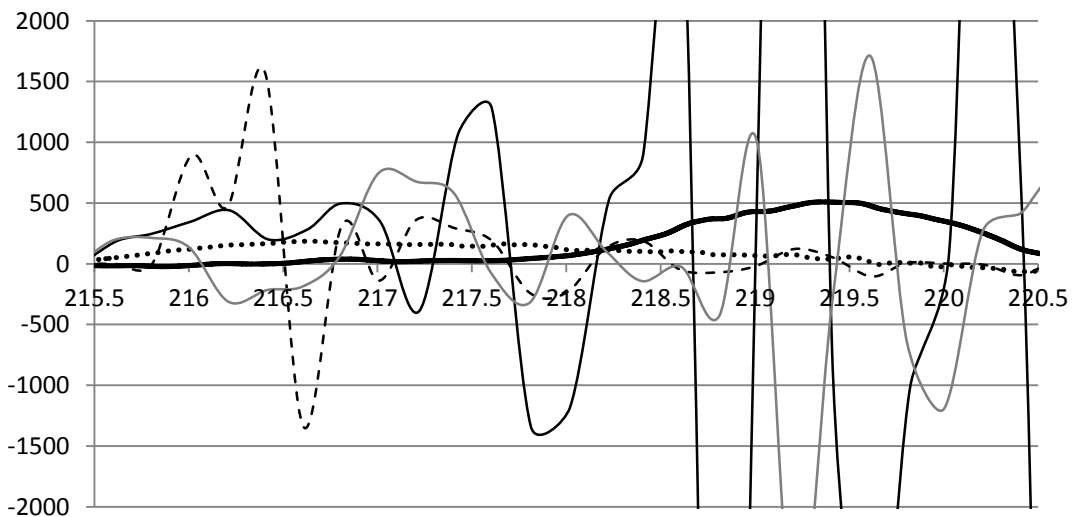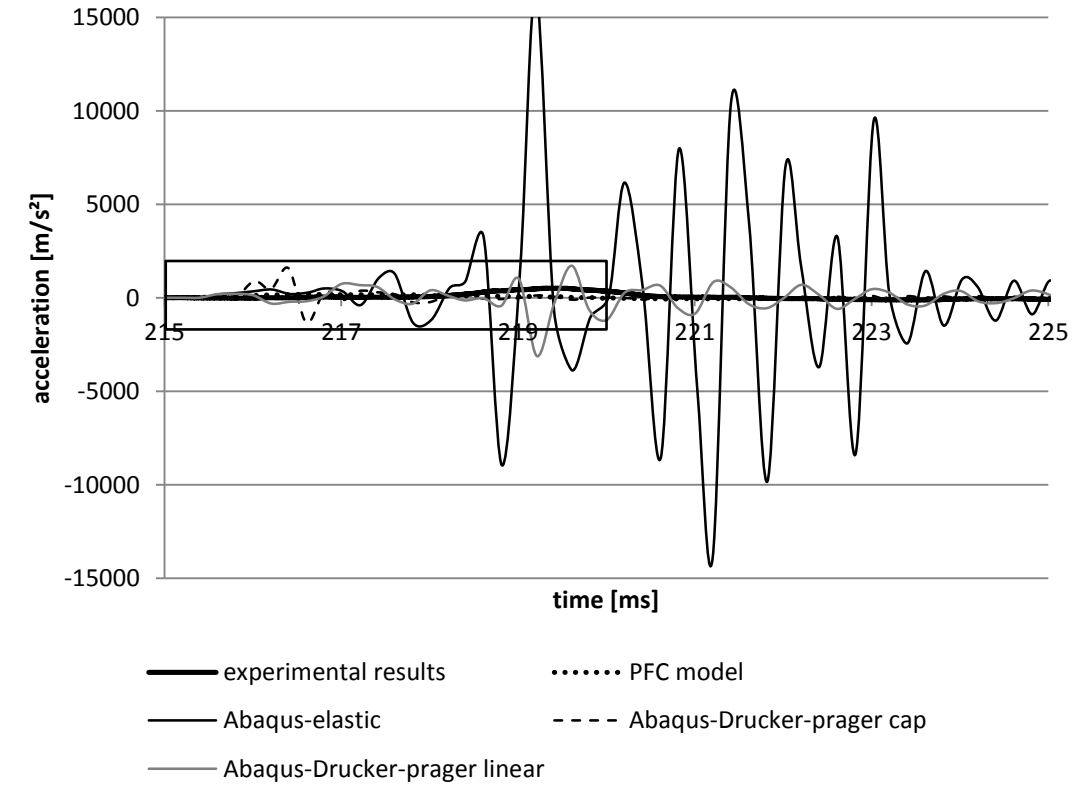

Figure 5.2.3 Experimental and numerical results of accelerometer A5

The experimental result shows a delay of 4ms from the starting of impulse (at 214ms), and reaches the peak of 500m/s^2, while PFC model gives 1.5ms-delay instead and lower peak (about 250m/^{2}) but longer reaction period. The result of cap model seems more reasonable among that

of Abaqus models. In the period from 215.5ms to 220.5ms which can be seen as reaction period of cap model, it has relatively high amplification (peak value 1500m/s^2) at beginning and then decays gradually. After reaction period it approaches to zero.

The delay of reaction period is caused by the distance between section A-A and loading section, while the one of peak value is caused by the dissipation of energy.

(III) Section B-B

Section B-B is 400mm deeper than section A-A. Figure 5.2.4 describes the experimental and numerical results of accelerometer A9. Accelerometer A9 is also near the interface.
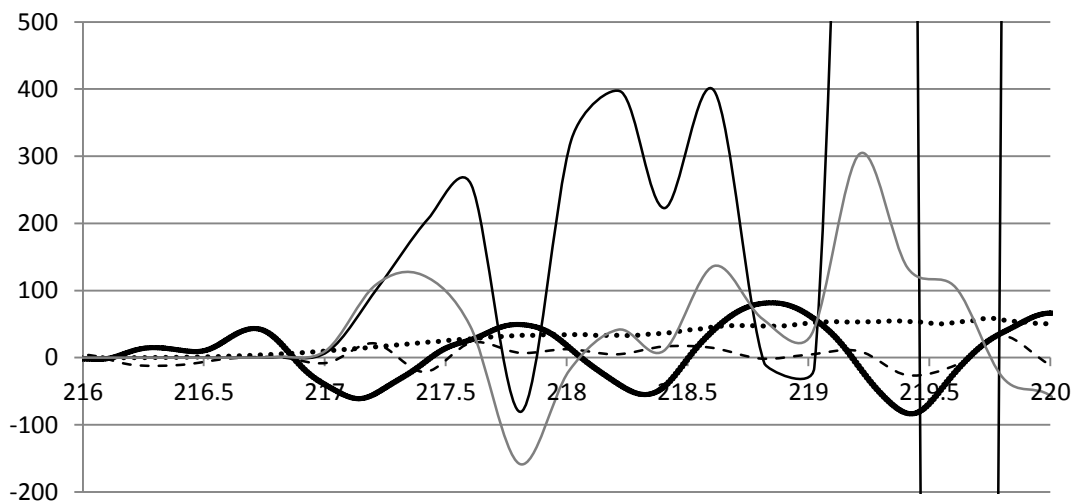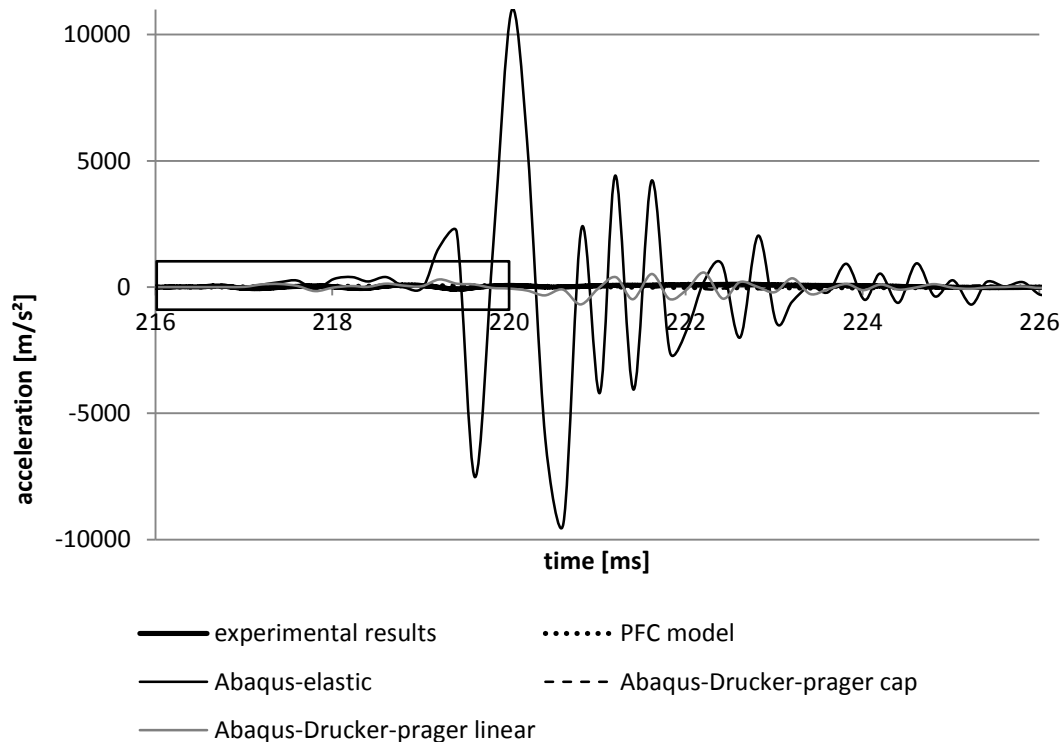

Figure 5.2.4 Experimental and numerical results of accelerometer A9

By reviewing Figure 5.1.8, it seems that the trends of numerical results are similar with that of test 1. Only the values are less for this lower input pressure. On the contrary the experimental results go into few vibrations.

5.2.2 Results of longitudinal force

Figure 5.2.5 shows the stress of Point A1 during test 2. Point A1 is at the center of loading section. As described in chapter 5.1.2, the results of Abaqus model are more reasonable, especially the result from Drucher-prager linear model, which is nearly overlapping the input pressure. Elastic one is also relatively fitted, only gives some oscillations at the ending moment. The result of cap model has higher oscillations around the input pressure.
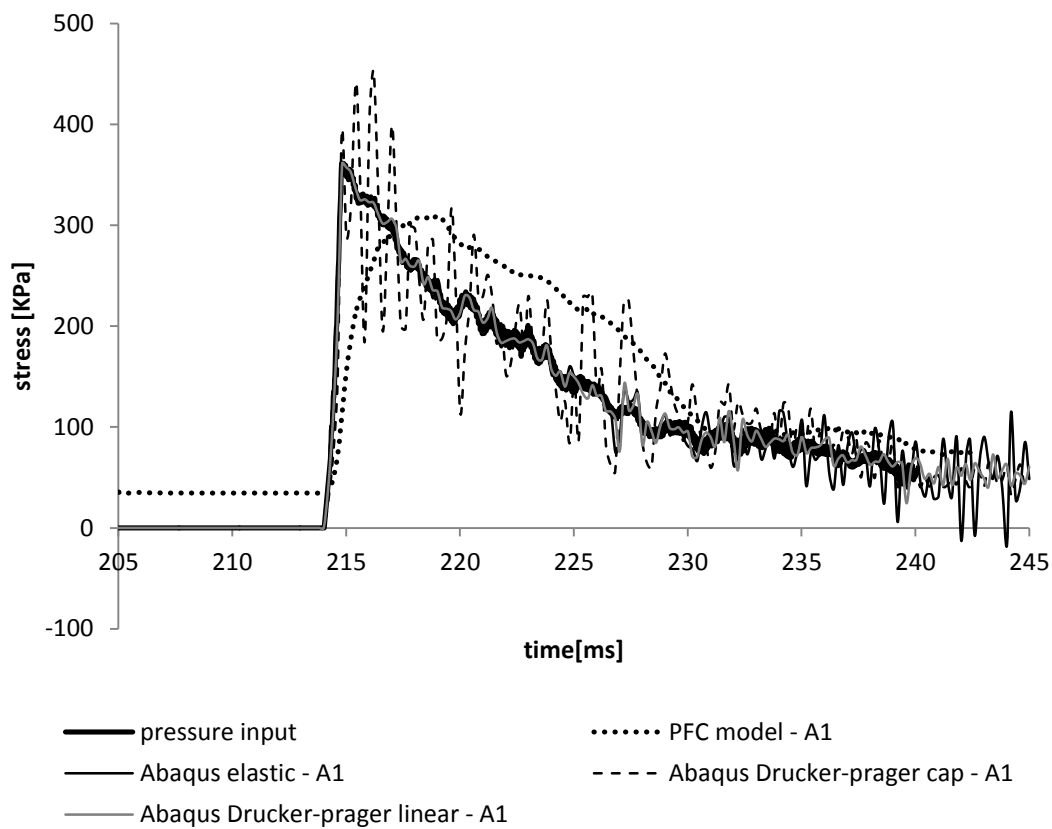

Figure 5.2.5 stress of center point on the loading section (top section) with friction 0.4

On the other side, the stress of Point D (Figure 5.2.6) shows a delay of 5ms, which is the same with test 1. From the point of view of quantity, the peak stresses in elastic and Drucker-prager linear model are higher than the peak of input pressure. This difference from test 1 seems strange.
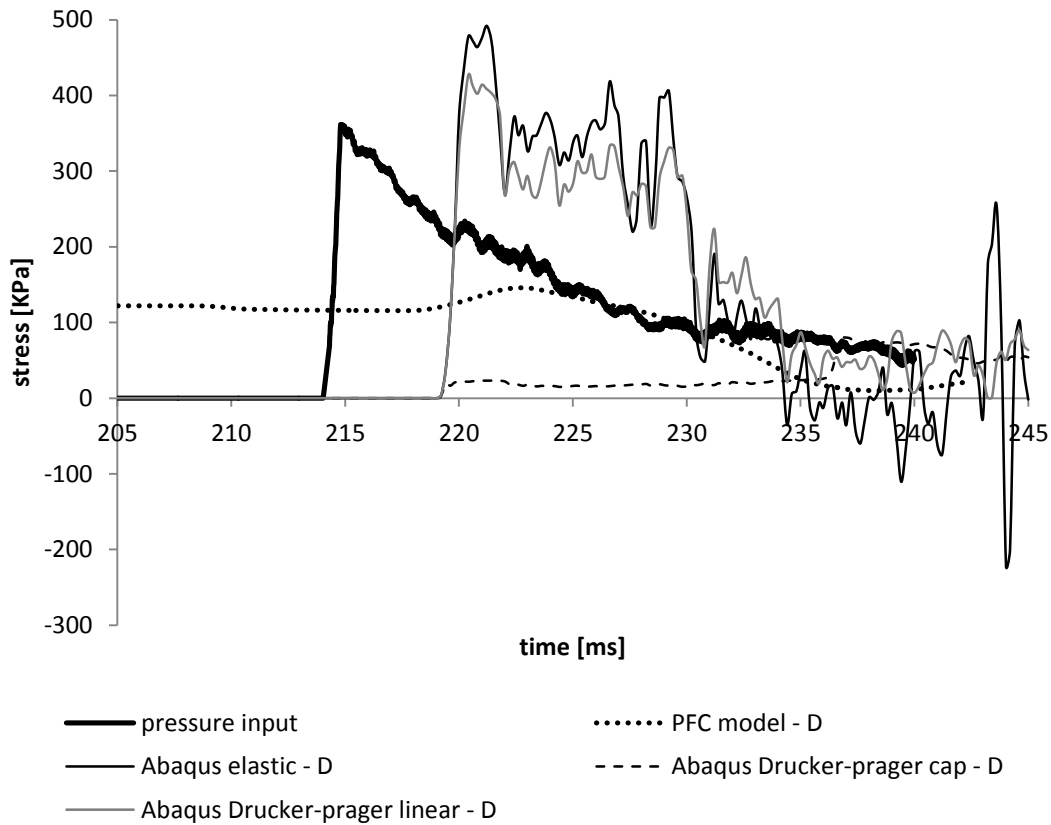
Figure 5.2.6 stress of center point on the base section (bottom section) with friction 0.4

5.2.3 Results of longitudinal displacement

The PFC model gives about 11mm of maximum displacement. Figure 5.2.7 – Figure 5.2.8 illustrate the comparisons of longitudinal displacements between Abaqus model with different friction and PFC model with friction 0.4. Overall, the trends of displacement of cap model are similar under different frictions. At around 215ms, which is 1ms delay to input pressure, displacements appear. The results of cap model increase under loading, and reach the peak, then become steady at maximum values (27mm under friction 0.2, 17mm under friction 0.4). However, elastic model and Drucher-prager linear model have similar but much less displacements. The maximum displacement under friction 0.2 is 4mm, while it is 3mm under friction 0.4. But not like the result of cap model, the displacements of elastic model and linear model decrease after peaks.
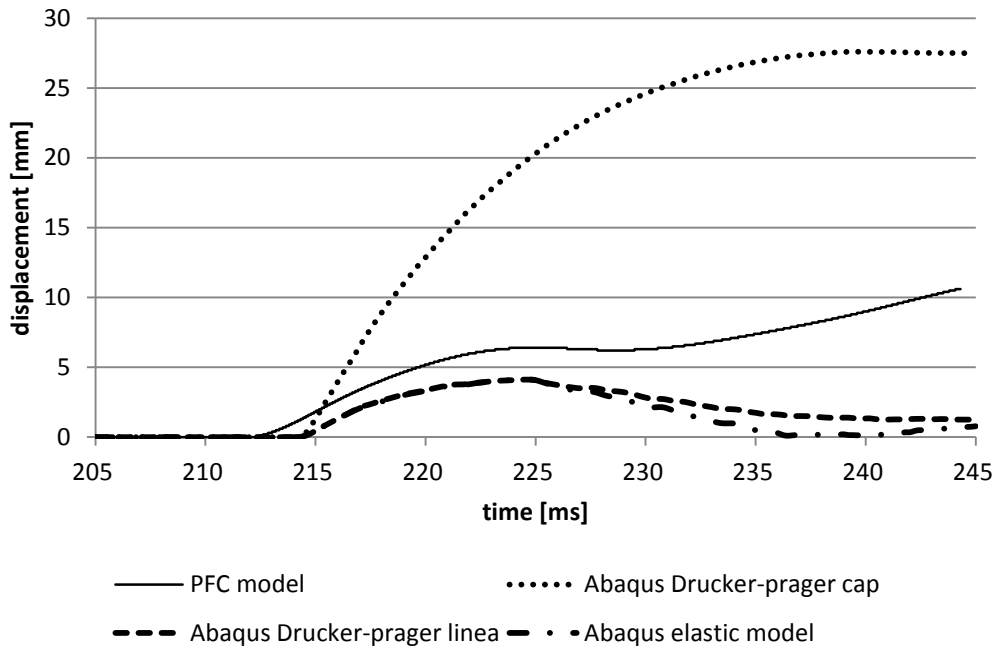
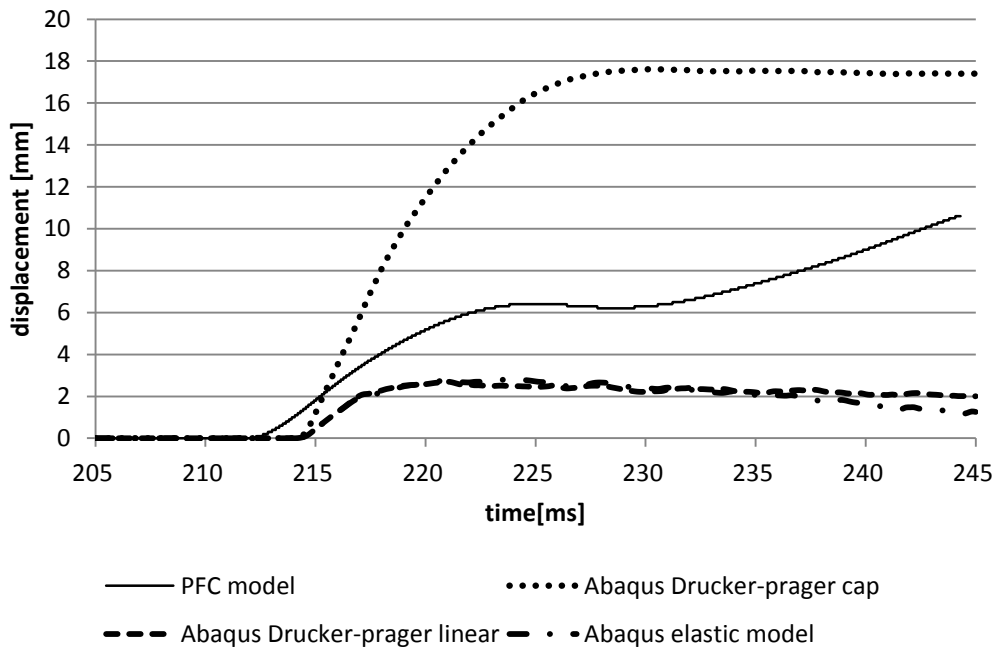Figure 5.2.7 longitudinal displacement of PFC model (friction 0.4) and Abaqus model (friction 0.2)

Figure 5.2.8 longitudinal displacement of PFC model (friction 0.4) and Abaqus model (friction 0.4)

5.3 Results of other tests

5.3.1 Test 3 L-40-T-1

The impulse load 3 is also forced on the models. This impulse is similar with the previous one , test 2, no matter the peak value or the duration of pressure, only except that the starting time is 1ms in advance. So the Abaqus results is similar, the trends are the same with test 2. What needs to be pointed out is in the experiment procedure and PFC simulation, the confinement of 40KPa is processed before the impulse loading, so it leads to different results. However, since the Abaqus model is more simplified, the bottom section of soil specimen is constrained as a fixed boundary condition. The confinement which should be acted on the bottom section cannot be simulated. It is same with the situation of rotation procedure that cannot be simulated in this Abaqus model either. That is the reason why there's no needs to analyze the results of test 3 and analyze the results in vertical direction. So, even though test 3 is also processed on the models, the results are not described here.

5.3.2 Test 4 H-122-T-1-1

The impulse of loading in test 4 has also a high peak pressure (1000KPa) which is similar to test 1, and starts 2ms in advance of test 1, but ends up with positive 40KPa pressure after during slow reduction, in which it is different with test 1. So here only the results of longitudinal displacements are shown in the following.

Figure 5.3.1 illustrates the longitudinal displacements of numerical models with friction 0.4. It can be seen that the results of Drucher-prager models do not rebound and maintain stable and convergent under test 4.
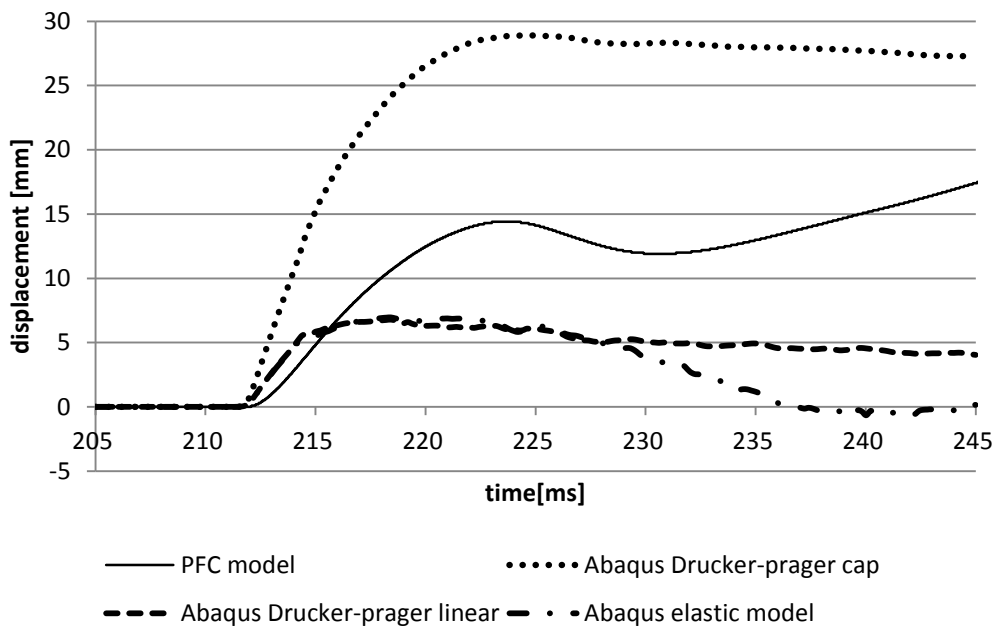

Figure 5.3.1 longitudinal displacement of PFC model and Abaqus model with friction 0.4

Chapter 6 Conclusions

In this work of thesis, a simple continuous numerical model of shock tube is created using Abaqus, which consists of axial-symmetric soil specimen (1.42m long, 29.15m wide) and analytical rigid chamber (without thickness). Four kinds of material are considered: Elastic model, Porous elastic model, Drucker-Prager linear model, Drucker-Prager cap model. The sand-steel chamber's friction influence is studied in detail both in static and dynamic conditions. The behaviors of the 4 materials are investigated in several cyclic static load conditions. The effects of friction and plasticity are analyzed within the results of Abaqus models.

On the other hand, a discrete numerical model of shock tube is created using PFC3D, which consists of rigid cylinder wall without thickness and large amounts of balls full filled inside walls. The model has 1.42m length and 29.15mm inter-radius. Four impulse waves of experimental tests are applied on the model.

In general, friction necessarily leads to a reduction of maximum displacement. However, the effect of friction is different on the points at different positions; since the friction is applied directly on the interface of soil and chamber, the effect on the points on the interface is large; on the contrary, the center point on the same section is less influence. At the same time the depth of point is also a factor that needs to be taken consideration. The points on deeper section are influenced less by the load, have less peak displacement compared to the top section.

The material plasticity is another reason of energy dissipation besides friction, and is the main one that takes a bigger role compared to friction. It is shown on the maximum displacement and dissipation energy. Drucker-Prager material model always gives larger displacement and larger dissipation energy compared to elastic model. Even under the case of Drucker-Prager cap material models, the bottom section is nearly not affected by the impulse load, which is not only caused by the depth of section, but also a result of material plasticity that leads to large energy dissipation.

The two numerical approaches, which mainly differ for model's micro structures and simulating principles, lead to different results. From the point of view of material characters, in the shock tube tests, the soil used is one kind of sand, which has very little even negligible cohesion between soil particles. Therefore, the displacement of soil is caused by the decrease of the void between particles both in volume and quantities. The procedure of compaction of soil under impulse load is exactly the reduction of porosity, while the stiffness of particle is very large, which leads to nearly no deformation of particle itself. So, the behavior of this sand is mainly presented as discrete characters. From the point of view of results, in general, the results from PFC model are more reasonable through comparisons between results of two numerical model and experimental results. Under static condition, the PFC model gives a larger peak displacement after loading and bigger residual displacement after unloading, than Abaqus models of all kinds of materials. Under dynamic impulse, the acceleration of PFC model has not any oscillation and only one peak which value is more or less the same with that of experimental results. However, the Abaqus models show much larger peak of accelerations and vibrate severely. So the discrete model of PFC is more reasonable to simulate these experimental tests than the continuous models of Abaqus.

Bibliograghy

Abaqus (2007). Abaqus Manuals and Theory. Dassault Syatemes Simulia Corp.

Bonacina F., Dell'era G., A. (2013). Modellazione agli elementi distinti della propagazione di onde d'urto nel terreno. Master thesis, Politecnico di Milano.

Calvetti F.(2008). Discrete modelling of granular materials and geotechnical problems. Discrete modelling of geomaterials.

Cazerzan, A. (2010). High Strain-Rate Uniaxial Tensile Constitutive Behaviour in Fibre Reinforced Cementitious Composites. PhD thesis, Politecnico di Milano.

Colombo, M., di Prisco, M., and Martinelli, P. (2011). A new shock tube facility for tunnel safety. Experimental mechanics.

Colombo, M., di Prisco, M., and Martinelli, P. (2013). Layered concrete plates interacting with soil under blast loads: an experimental investigation. European Journal of Environmental and Civil Engineering.

Colombo, M., Martinelli, P., and di Prisco, M., (2012). On the blast resistance of prefabricated high performance tunnel.

Corti L., Corti L. G., A. (2012). Soil Structure Interaction Under Blast Load: a Multilayer Fibre Cementitious Composite Structural Solution. Master thesis, Politecnico di Milano.

PFC3D (2012). PFC3D Manuals. Itasca Corp.